

## Modelling and kinetic study of a Fischer-Tropsch reactor for the synthesis of e-kerosene

**Auteur :** Rouxhet, Antoine

**Promoteur(s) :** Léonard, Grégoire

**Faculté :** Faculté des Sciences appliquées

**Diplôme :** Master en ingénieur civil en chimie et science des matériaux, à finalité spécialisée

**Année académique :** 2021-2022

**URI/URL :** <http://hdl.handle.net/2268.2/14391>

---

### *Avertissement à l'attention des usagers :*

*Tous les documents placés en accès ouvert sur le site le site MatheO sont protégés par le droit d'auteur. Conformément aux principes énoncés par la "Budapest Open Access Initiative"(BOAI, 2002), l'utilisateur du site peut lire, télécharger, copier, transmettre, imprimer, chercher ou faire un lien vers le texte intégral de ces documents, les disséquer pour les indexer, s'en servir de données pour un logiciel, ou s'en servir à toute autre fin légale (ou prévue par la réglementation relative au droit d'auteur). Toute utilisation du document à des fins commerciales est strictement interdite.*

*Par ailleurs, l'utilisateur s'engage à respecter les droits moraux de l'auteur, principalement le droit à l'intégrité de l'oeuvre et le droit de paternité et ce dans toute utilisation que l'utilisateur entreprend. Ainsi, à titre d'exemple, lorsqu'il reproduira un document par extrait ou dans son intégralité, l'utilisateur citera de manière complète les sources telles que mentionnées ci-dessus. Toute utilisation non explicitement autorisée ci-avant (telle que par exemple, la modification du document ou son résumé) nécessite l'autorisation préalable et expresse des auteurs ou de leurs ayants droit.*

---

# **Modelling and kinetic study of a Fischer-Tropsch reactor for the synthesis of e-kerosene**

**ROUXHET Antoine**

Thesis presented for obtaining the Master's degree in  
**Chemical and Materials engineering**

Supervisor:  
**LEONARD Grégoire**

Academic Year: **2021-2022**

# Acknowledgements

The accomplishment of this master's thesis would not have been possible without the help and support of many people. I am sincerely grateful to Professor Grégoire Léonard for allowing me to work on such a fascinating topic. I thank him for his help and critical point of view during this semester, which helped me improve my work. I also thank him for proofreading this report and for his valuable comments.

Then, I would like to thank Alejandro Morales, without whom this thesis would have been far more complicated to realise. I thank him for his help during my reflections and for all the valuable discussions we have shared. I thank him for his kindness and attention during the explanations of my observations and results. I finally thank him for proofreading this report. I would also like to thank the other PhD students, which are part of Prof. Grégoire Léonard's team, for their welcome in their office.

I thank Andreas Meurer, PhD student at the German Aerospace Center (DLR), for answering our questions about his article. I also thank him for the nice and useful discussion that we had.

I am also thankful to Professor Nathalie Job and Markus Dickamp for being part of my jury and reading this report. I also thank Prof. Nathalie Job for answering my questions.

Finally, as this master's thesis represents the completion of two intensive years of master's degree and five years of engineering studies, I would like to take the opportunity to thank all professors of the Applied Science Faculty, especially the professors from the Chemical Engineering Department, who contributed directly or indirectly to the proper continuity of my studies. I also thank Juliette and Loris for the mutual aid, support, and laughter we have had during the past two years.

# Abstract

If climate change is evident, society's current ecological transition is also apparent. Renewable energy sources utilisation is paramount to mitigate the anthropogenic environmental impact. However, they present significant drawbacks, including primarily their variability. It implies the necessity to store them in the medium and long term to address this problem, which is possible through the Power-to-X technology. This work specifically focuses on the production of e-kerosene through the low-temperature cobalt-based Fischer-Tropsch synthesis. There are various kinetics in the literature describing this reaction. The overall idea behind this master's thesis is to identify the best kinetic model to be implemented in a reactor model. Ultimately, it will help to understand the interactions between the reaction and the rest of the process.

In this work, the kinetics developed by [Ma et al. \(2014a,b\)](#) are specifically studied. Compared to more classical models, it includes a positive kinetic effect induced by water. A reactor model is developed in Aspen Custom Modeler® in which the kinetics are considered. The reaction stoichiometry is developed following the Anderson-Schulz-Flory theory by accounting for the methane deviation from this ideal model.

The implementation of these kinetics and stoichiometry is validated with experimental data ([Ma et al., 2014a,b](#)). It is shown that the squared correlation coefficients between the calculated and experimental values exceed 90%. Then, the results yielded by the reactor model are compared with another study ([Morales and Léonard, 2022](#)) in which more simple kinetics, following a Langmuir-Hinshelwood expression, are implemented. The model developed in this study concludes that a reactor 2.5 times greater is required to reach an equivalent conversion. A discussion is conducted to explore the origin of this divergence, yielding various assumptions. The general expression and catalyst used to regress both models differing, it probably plays a role in this dissimilarity. A specific interest is also given to the kinetics validity range, which varies depending on the assumptions taken to determine it. A fully numerical approach yields a limiting conversion value of 83.5% in base case conditions, while only considering [Ma et al. \(2014a\)](#)'s experimental data leads to a limiting value of 52%. The validity of these approaches is discussed. Eventually, some sensitivity analyses are conducted to observe the reactor model behaviour when some of its parameters and variables are varied. It shows that proper temperature control of the reaction is crucial for reactor performance and that an appropriate tuning of cooling system parameters should be conducted. These sensitivity studies also reveal that an optimal reactor temperature around 210°C and a syngas ratio slightly above 2 maximise the kerosene fraction selectivity.

The perspectives envisaged for this project are multiple. A particular focus should be given to refining the kinetics validity range and deepening the study of the water kinetic effect, possibly experimentally. Validation of the reactor model with other experimental data seems also relevant. Hopefully, the objective is to conduct those experiments on the future lab-scale installation at ULiège.

# Résumé

Si le changement climatique est une évidence, la transition écologique actuelle de notre société est également perceptible. L'utilisation de sources d'énergie renouvelable est d'une importance capitale afin de réduire l'impact environnemental d'origine anthropique. Cependant, leur utilisation présente des désavantages conséquents, notamment leur variabilité. Elles doivent donc pouvoir être stockées à moyen et long terme pour répondre à ce problème, ce qui est possible avec la technologie Power-to-X. Ce travail porte principalement sur la production de e-kérosène à travers la synthèse de Fischer-Tropsch à basse température avec un catalyseur à base de cobalt. Il existe différents modèles de cinétique décrivant cette réaction dans la littérature. L'idée générale derrière ce mémoire est d'identifier le meilleur d'entre eux afin de l'implémenter dans un modèle de réacteur. À terme, celui-ci aidera à comprendre les interactions entre la réaction et le reste du procédé.

Dans ce travail, le modèle cinétique développé par [Ma et al. \(2014a,b\)](#) est spécifiquement étudié. Par rapport à des cinétiques plus classiques, il inclut un effet cinétique positif induit par l'eau. Un modèle de réacteur est développé dans Aspen Custom Modeler® dans lequel la cinétique de [Ma et al. \(2014a,b\)](#) est incluse. La stœchiométrie de la réaction est développée selon la théorie d'Anderson-Schulz-Flory en tenant compte de la déviation du méthane par rapport à ce modèle idéal.

L'implémentation de cette cinétique et cette stœchiométrie est validée avec des données expérimentales ([Ma et al., 2014a,b](#)). Il est montré que les coefficients de corrélation avec ces données dépassent 90%. Ensuite, les résultats obtenus par le modèle du réacteur sont comparés à une autre étude ([Morales and Léonard, 2022](#)), où une cinétique plus simple est mise en œuvre. À conversion équivalente, le volume du réacteur est environ 2,5 fois plus grand avec le modèle développé dans cette étude. Diverses hypothèses sont posées pour étudier l'origine de cette divergence. L'expression générale et le catalyseur utilisés pour régresser les deux cinétiques étant différents, ils jouent probablement un rôle dans cet écart. Un intérêt particulier est également porté au domaine de validité de cette cinétique. Une approche numérique donne une valeur de conversion limite de 83,5%, tandis que la seule prise en compte des données expérimentales de [Ma et al. \(2014a\)](#) conduit à une valeur limite de 52%. La validité de ces approches est discutée. Enfin, des analyses de sensibilité sont menées pour observer le comportement du modèle lorsque certains de ses paramètres sont modifiés. Elles montrent qu'un contrôle adéquat de la température de réaction est crucial pour les performances et qu'un réglage approprié des paramètres du système de refroidissement doit être effectué. Ces études de sensibilité révèlent également qu'une température optimale autour de 210°C et un rapport de gaz de synthèse légèrement supérieur à 2 maximisent la sélectivité de la fraction kérosène.

Les perspectives envisagées pour ce projet sont multiples. Une attention particulière devrait être accordée à l'affinement du domaine de validité de la cinétique et à une étude approfondie de l'effet cinétique de l'eau, éventuellement de manière expérimentale. La validation du modèle de réacteur avec d'autres données expérimentales semble également pertinente. L'objectif est de mener ces expériences sur la future installation pilote à l'ULiège.

# Contents

<b>I</b>	<b>Introduction</b>	<b>1</b>
I.1	Objectives pursued during this master's thesis	3
<b>II</b>	<b>Literature review</b>	<b>4</b>
II.1	Conventional kerosene production	4
II.2	Power-to-X concept	5
II.2.1	Origin of the concept	5
II.2.2	Power-to-Gas	5
II.2.2.a	Power-to-Hydrogen	5
II.2.2.b	Power-to-Methane	6
II.2.2.c	Power-to-Syngas	6
II.2.3	Power-to-Liquids	7
II.2.3.a	Power-to-Methanol	7
II.2.3.b	Power-to-DME	8
II.2.3.c	Power-to-Fischer-Tropsch-fuels	8
II.2.4	Power-to-Chemicals	10
II.2.5	Power-to-Heat	10
II.3	Fischer-Tropsch synthesis	10
II.3.1	Type of catalysts used	11
II.3.1.a	Cobalt-based catalysts	11
II.3.1.b	Iron-based catalysts	12
II.3.2	Reaction mechanisms	12
II.3.2.a	Carbide mechanism	13
II.3.2.b	Enol mechanism	14
II.3.2.c	CO insertion mechanism	14
II.3.3	Reactor configurations	15
II.3.3.a	Fixed-bed reactor	15
II.3.3.b	Slurry phase reactor	16
II.3.3.c	Circulating fluidized bed reactor	17
II.3.3.d	Fixed fluidized bed reactor	18
II.4	State-of-the-art of sustainable aviation fuel production	19
II.4.1	Sustainable aviation fuel production pathways	19
II.4.2	Scale-up challenges of the Power-to-Liquids pathway	19
II.4.3	European projects	20
<b>III</b>	<b>Fischer-Tropsch reactor modelling</b>	<b>22</b>
III.1	Reactions and thermodynamics	22
III.2	Reaction rates and kinetics	25

III.3	Fischer-Tropsch product distribution . . . . .	27
III.3.1	The Anderson-Schulz-Flory distribution . . . . .	28
III.3.2	Differentiation between paraffins and olefins production . . . . .	30
III.3.3	Calculation of chain growth probability . . . . .	31
III.3.4	Non-ideal Anderson-Schulz-Flory distribution . . . . .	32
III.4	Stoichiometry . . . . .	33
III.4.1	Determination of Fischer-Tropsch product stoichiometric coefficients . . . . .	34
III.4.2	Determination of hydrogen usage ratio . . . . .	35
III.5	Implementation of balances . . . . .	36
III.5.1	Material balance . . . . .	36
III.5.2	Energy balance . . . . .	38
III.5.3	Momentum balance . . . . .	40
<b>IV</b>	<b>Results analysis and discussion</b>	<b>42</b>
IV.1	Kinetics model validation . . . . .	42
IV.2	Base case results . . . . .	45
IV.2.1	Analysis of inlet conditions . . . . .	45
IV.2.2	Analysis of base case results . . . . .	47
IV.2.2.a	Reactor performance . . . . .	47
IV.2.2.b	Temperature profiles . . . . .	49
IV.2.2.c	Pressure profile . . . . .	50
IV.2.2.d	Fischer-Tropsch product distribution . . . . .	51
IV.3	Reactor sizing and kinetics model limits . . . . .	55
IV.4	Sensitivity analyses . . . . .	60
IV.4.1	Operating variables influence on reactor performance . . . . .	60
IV.4.1.a	Operating temperature influence . . . . .	60
IV.4.1.b	Operating pressure influence . . . . .	62
IV.4.1.c	Inlet syngas ratio influence . . . . .	63
IV.4.1.d	Inlet total flow rate influence . . . . .	64
IV.4.1.e	Influence of the presence of water in the inlet stream . . . . .	65
IV.4.2	Cooling system variables influence on temperature control and reactor performance . . . . .	66
IV.4.2.a	Comparison of co- and counter-current cooling . . . . .	66
IV.4.2.b	Coolant inlet temperature and flow rate influence . . . . .	68
IV.4.2.c	Overall heat transfer coefficient influence . . . . .	69
IV.4.3	Catalytic bed characteristics influence on pressure drop and reactor performance . . . . .	70
IV.4.3.a	Catalytic bed porosity influence . . . . .	70
IV.4.3.b	Catalyst particle diameter influence . . . . .	73
<b>V</b>	<b>Conclusions and perspectives</b>	<b>75</b>
<b>A</b>	<b>Energy balance full derivation</b>	<b>87</b>
<b>B</b>	<b>Test conditions for kinetics validation</b>	<b>89</b>
<b>C</b>	<b>Kinetics validation data</b>	<b>90</b>

# List of Figures

I.1	Evolution of the amount of CO <sub>2</sub> emitted in the atmosphere and its concentration in the atmosphere between 1750 and 2020 (Climate.gov, 2021b)	2
II.1	Schematic representation of the Power-to-Fischer-Tropsch technology (Léonard, 2021b)	9
II.2	Schematic representation of the carbide mechanism (inspired by Shafer et al. (2019) and Teimouri et al. (2021))	13
II.3	Schematic representation of the enol mechanism (inspired by Shafer et al. (2019) and Teimouri et al. (2021))	14
II.4	Schematic representation of the CO insertion mechanism (inspired by Shafer et al. (2019) and Teimouri et al. (2021))	15
II.5	Illustration of a multi-tubular packed-bed reactor (Guettel et al., 2008)	16
II.6	Illustration of a slurry phase reactor (Guettel et al., 2008)	17
II.7	Illustration of a circulating fluidized bed reactor (Steynberg et al., 2004)	17
II.8	Illustration of a fixed fluidized bed reactor (Steynberg et al., 2004)	18
III.1	Molar flow rate distribution at the reactor outlet for reagent and product fractions for the following inlet conditions: $T = 210^{\circ}\text{C}$ , $P = 20$ bar, $\dot{F} = 0.01$ kmol/h and $\text{H}_2/\text{CO} = 2$ .	24
III.2	Molar flow rate distribution at the reactor outlet for the Fischer-Tropsch product fractions for the following inlet conditions: $T = 210^{\circ}\text{C}$ , $P = 20$ bar, $\dot{F} = 0.01$ kmol/h and $\text{H}_2/\text{CO} = 2$ .	24
III.3	Schematic representation of chain growth probability (inspired by Panahi et al. (2012))	28
III.4	Molar fraction ASF distribution for a chain growth probability $\alpha = 0.9$	30
III.5	Schematic representation of an experimental Fischer-Tropsch product distribution compared with an ideal ASF distribution (Todic et al., 2017)	32
III.6	Schematic representation of a plug-flow reactor of length $L$ , cross-sectional area $A$ , inlet and outlet molar flow rates for component $i$ $\dot{F}_{i,0}$ and $\dot{F}_{i,L}$ , respectively. An infinitesimal volume $\Delta V$ is also represented	37
III.7	Schematic representation of a plug-flow reactor with its cooling system and their respective inlet and outlet temperatures. An infinitesimal volume $\Delta V$ in which the heat exchange rate $\Delta \dot{Q}$ is also represented	39
IV.1	Parity plot for comparison of experimental (Ma et al., 2014a) and calculated Fischer-Tropsch reaction rate $r'_{FT}$ . Their squared correlation coefficient $r^2$ is also shown	44
IV.2	Parity plot for comparison of experimental (Ma et al., 2014b) and calculated methane reaction rate $r'_{\text{CH}_4}$ . Their squared correlation coefficient $r^2$ is also shown	44
IV.3	Variation of the mass fraction of Fischer-Tropsch product fractions with chain growth probability $\alpha$	46
IV.4	Variation of chain growth probability $\alpha$ with syngas ratio, $\text{H}_2/\text{CO}$ , at $210^{\circ}\text{C}$	46
IV.5	Variation of chain growth probability $\alpha$ with temperature for a syngas ratio of 2.1	46



IV.6	Evolution of ratio between CO net reaction rate calculated with <a href="#">Iglesia et al. (1993)</a> 's model and the one calculated with <a href="#">Ma et al. (2014a)</a> 's model down the reactor for 1.25 kg of catalyst in the base case conditions . . . . .	48
IV.7	Temperature profiles of the reactor and cooling medium for 1.25 kg of catalyst in the base case conditions . . . . .	50
IV.8	Pressure profile in the reactor for 1.25 kg of catalyst in the base case conditions . . . .	51
IV.9	Distribution of Fischer-Tropsch product molar fractions in the product spectrum at the reactor outlet for 1.25 kg of catalyst in the base case conditions . . . . .	52
IV.10	Evolution of syngas ratio in an isothermal reactor as a function of its initial value for 1.25 kg of catalyst in the base case conditions . . . . .	54
IV.11	Qualitative representation of the conversion evolution with reactor volume for an isothermal plug-flow reactor . . . . .	56
IV.12	Evolution of water-to-hydrogen partial pressures ratio as a function of the catalyst mass used in the reactor in the base case conditions . . . . .	57
IV.13	Evolution of Fischer-Tropsch reaction rate $r'_{FT}$ along the reactor in the base case conditions . . . . .	58
IV.14	Influence of reactor operating temperature on CO conversion and methane and C12-C20 mass fractions at the reactor outlet for 0.5 kg of catalyst in the base case conditions	61
IV.15	Influence of reactor operating temperature on the C12-C20 molar flow rate at the reactor outlet for 0.5 kg of catalyst in the base case conditions . . . . .	61
IV.16	Influence of reactor operating pressure on CO conversion and methane and C12-C20 mass fractions at the reactor outlet for 1.25 kg of catalyst in the base case conditions	62
IV.17	Influence of inlet syngas ratio on the CO conversion and methane and C12-C20 mass fractions at the reactor outlet for 0.5 kg of catalyst in the base case conditions . . . .	64
IV.18	Influence of inlet total molar flow rate on CO conversion and methane and C12-C20 mass fractions at the reactor outlet for 1.25 kg of catalyst in the base case conditions	65
IV.19	Influence of inlet water molar fraction on CO conversion and methane and C12-C20 mass fractions at the reactor outlet for 1.25 kg of catalyst in the base case conditions	65
IV.20	Comparison of the temperature profiles in the reactor and the cooling medium for co- and counter-current cooling modes for 1.25 kg of catalyst in the base case conditions	67
IV.21	Inlet coolant temperature influence on the reactor temperature profile for 1.25 kg of catalyst in the base case conditions . . . . .	68
IV.22	Inlet coolant temperature influence on CO conversion and methane and C12-C20 mass fractions at the reactor outlet for 1.25 kg of catalyst in the base case conditions . . . .	69
IV.23	Overall heat transfer coefficient, $U$ , influence on the reactor temperature profile for 1.25 kg of catalyst in the base case conditions . . . . .	70
IV.24	Catalytic bed porosity influence on the pressure profile in the reactor for 1.25 kg of catalyst in the base case conditions and a perfectly isothermal reactor . . . . .	71
IV.25	Catalytic bed porosity influence on the CO conversion and methane and C12-C20 mass fractions at the reactor outlet for 1.25 kg of catalyst in the base case conditions and a perfectly isothermal reactor . . . . .	72
IV.26	Catalyst particle diameter influence on the pressure profile in the reactor for 1.25 kg of catalyst in the base case conditions and a catalytic bed porosity of 30% . . . . .	73

# List of Tables

III.1	Meaning, value and units of the variables and parameters used in the Fischer-Tropsch reaction rate definition (see Equations III.7 and III.8)	26
III.2	Value and units of the parameters used in the methane reaction rate definition (see Equations III.9 and III.10)	26
III.3	Meaning, value and units of the variables and parameters used for chain growth probability calculation (see Equation III.27)	31
III.4	Meaning, value and units of the catalytic bed characteristics	38
III.5	Meaning, value and units of the variables and parameters used in the Ergun equation (see Equation III.77)	41
IV.1	Base case inlet conditions similar to Morales and Léonard (2022)	45
IV.2	Evolution of chain growth probability $\alpha$ , temperature and syngas ratio down the reactor with their corresponding mean value and standard deviation for 1.25 kg of catalyst in the base case conditions	52
IV.3	Inlet CO consumption rate for various inlet water contents for 1.25 kg of catalyst in the base case conditions	66
IV.4	Influence of the cooling mode on CO conversion, C12-C20 molar production and methane and C12-C20 mass fractions at the reactor outlet for 1.25 kg of catalyst in the base case conditions. The values for a perfectly isothermal reactor are shown for comparison	68
B.1	Test conditions, including inlet CO and H <sub>2</sub> partial pressures, total pressure, syngas ratio and space velocity at normal conditions, for which the reaction rates ( $r'_{FT}$ and $r'_{CH_4}$ ) were experimentally measured (Ma et al., 2014a,b) and calculated. The temperature is 220°C and the inlet stream only contains CO and H <sub>2</sub> for all tests	89
C.1	Fischer-Tropsch reaction rate ( $r'_{FT}$ ) experimental and calculated values from Ma et al. (2014a) and calculated values from current model for all test conditions	90
C.2	Methane reaction rate ( $r'_{CH_4}$ ) experimental and calculated values from Ma et al. (2014b) and calculated values from current model for all test conditions	91

# Chapter I

## Introduction

During the summer of 2021, unprecedented flooding hit Belgium and mudslides ravaged the west of Germany ([Le Monde, 2021](#)). Australia suffered from historical wildfires in 2019 and 2020, just like the Amazon rainforest every past few years ([Eos, 2022](#)). Ethiopia is currently going through the worst drought in its history, as it has barely not rained since the end of 2020 ([Le Temps, 2022](#)). In 2020, south-east Asia was hit by various typhoons and cyclones, putting the lives of millions of people in danger ([Unicef, 2020](#)). Brazil observed a cold spell last year and suffered from snowfalls ([RTBF, 2021](#)). These climatic events that made the news during the past few years are isolated, different in nature, and on various continents, but they all lead to the same conclusion: climate is changing. These climatic events are tangible evidence of worldwide climate change. If someone still doubts that Earth has entered a critical climate emergency, various numerical data translate less directly visible events that also demonstrate a global change. The most known indicator is maybe the global average surface temperature, which has risen by 0.18°C per decade since 1981 with a 2020 surface temperature almost 1°C higher than the 20<sup>th</sup> century average ([Climate.gov, 2022](#)). Another indicative variable is the global mean sea level, which has increased by 21 cm between 1900 and 2020 and for which the rising rate has increased to 3.7 mm/year over the period 2006-2018, which is twice as fast as during the 20<sup>th</sup> century ([European Environment Agency \(EEA\), 2021](#)). Another sign of climate change is the progressive decline and disappearance of glaciers. It has been measured that 2019/2020 was the 33<sup>rd</sup> year in a row that mountain glaciers lost rather than gained ice ([Climate.gov, 2021a](#)).

All these events are linked to a common origin: the greenhouse effect intensification induced by the increase in the concentration of greenhouse gases in the atmosphere. There are different greenhouse gases, including methane, ozone, nitrous oxide, and hydrofluorocarbons (HFCs), but the most publicised gas is certainly CO<sub>2</sub>, which is responsible for around 65% of the anthropogenic greenhouse effect ([Jancovici, 2007](#)). Its concentration increase is inevitably linked to the growing emissions since the beginning of the Industrial Revolution in 1750, as can be seen in Figure [I.1](#). It is interesting to observe the small decay in the CO<sub>2</sub> emissions for the year 2020, the first in several years, which is due to the COVID-19 pandemic which induced a reduction in human activities. These emissions should imperatively be decreased to mitigate the atmospheric CO<sub>2</sub> concentration rise and thus manage to limit the global warming to 1.5°C, as suggested by the latest IPCC report ([IPCC, 2022](#)).

To reach this objective, the emissions must be reduced by 45% by 2030, compared to the 2010 level, by taking several measures, including the reduction of fossil fuel usage, the utilisation of renewable energies, the implementation of new CO<sub>2</sub> capture and storage units, etc ([Pallardy, 2022](#)). Intending to maximise the impact of these different measures, it is essential to focus on the sectors emitting the largest amounts of CO<sub>2</sub>. It turns out that in 2016, the energy used in the industry accounted for

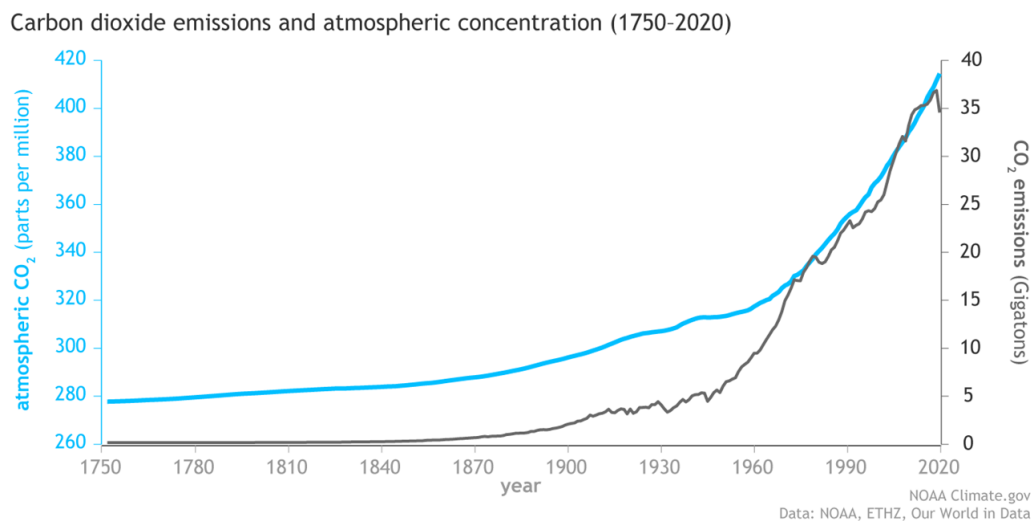


Figure I.1: Evolution of the amount of CO<sub>2</sub> emitted in the atmosphere and its concentration in the atmosphere between 1750 and 2020 (Climate.gov, 2021b)

24.2% of the global greenhouse gas emissions, while the energy used in buildings and transport was responsible for 17.5 and 16.2% of global emissions, respectively (Ritchie et al., 2020). Some solutions proposed to reduce CO<sub>2</sub> emissions in the industry are the improvement of the energy efficiency, using heat integration, for instance, the utilisation of renewable energies, the recycling of materials,... If these alternatives could not be possible, the industries could resort to carbon capture and storage. The decrease in the energy used in buildings goes through better insulation of old buildings and real estate sector replacement with low energy-intensive buildings. The majority of transport emissions come from road transport (Ritchie et al., 2020) which could be reduced through the electrification of the sector using renewable sources of electricity. However, the emissions caused by shipping and aviation are considered hard-to-abate because these sectors present more challenges and less potential for electrification compared to road transportation. It is explained by the difference in energy density between electricity and fuel. To cover the same distance, the mass of the battery is much larger than the mass of fuel. This problem is still manageable on the car level but not for shipping and aviation (Gross, 2020).

If the measures proposed above are applied to all sectors with the best possible efficiency, then the goal of a net-zero society for the year 2050 could be achieved. On top of mitigating anthropogenic CO<sub>2</sub> emissions, another solution is to capture already emitted CO<sub>2</sub> directly in the atmosphere, which results in net-negative emissions. The storage or the utilisation of the captured CO<sub>2</sub> is an important point to address for this technology, as well as for carbon capture in industry. The storage in soils is an effective solution, as it is a pretty well-known technology, which is already used for seasonal storage of natural gas (Léonard, 2021a). On the other side, the utilisation of CO<sub>2</sub> is an appealing approach, as CO<sub>2</sub> is a source of carbon, meaning that it could theoretically replace crude oil in the fossil-based industry. By combining CO<sub>2</sub> with H<sub>2</sub> it is possible to yield various chemicals that are historically produced from fossil fuels.

One category of chemicals that can be produced from CO<sub>2</sub> and H<sub>2</sub> are e-fuels. As previously stated, they can be synthesised from captured CO<sub>2</sub>. But they are also considered as long-term energy storage carriers addressing one major problem of renewable energy sources, i.e. their variability. For

instance, one way to store renewable electricity is to use it to power an electrolyser that converts water into green  $H_2$ . However,  $H_2$  has a low energy density per unit volume and is difficult to store. Then, converting this  $H_2$  into liquid fuel, with, therefore, a higher energy density per unit volume, is an attractive alternative. This solution is often referred to as Power-to-Liquids (PtL), or more generally, Power-to-X (PtX). It is based on the idea that combining air captured  $CO_2$  with  $H_2$  to synthesise transportation fuels might be a solution to reach sustainability with carbonated fuels. The full decarbonisation is achievable if  $H_2$  is produced by water electrolysis powered by renewable energies. It is a considerable advantage as, in most cases, it does not require a complete redesign of all vehicles, unlike the electrification solution that necessitates the replacement of thermal engines with electric batteries (Léonard, 2021b).

## I.1 Objectives pursued during this master's thesis

This master's thesis focuses on the production of e-kerosene that can be further upgraded to jet fuel. It is a relevant topic of study, as the aviation sector emissions are considered hard-to-abate, as mentioned above. To be more precise, this work is in line with the project developed by Professor Grégoire Léonard's team to set up a pilot installation for e-kerosene production, which is mainly conducted by Alejandro Morales, a PhD student. The aim is to produce e-kerosene through Fischer-Tropsch (FT) synthesis in which CO reacts with  $H_2$  to yield a large spectrum of hydrocarbon products and water. CO is obtained by converting  $CO_2$  in the reverse water-gas shift (rWGS) reaction, and  $H_2$  is produced by water electrolysis. At this time, three electrolysis cells are already available at ULiège, and a first reactor model describing the Fischer-Tropsch synthesis has been implemented with simple kinetics and stoichiometry.

The objectives pursued in this work are to develop a Fischer-Tropsch reactor model that accounts for the production of paraffins and olefins (and no longer only the paraffins, as performed by Morales and Léonard (2022)) with a more complex stoichiometry taking into account the variation of temperature and syngas ratio in the reactor. The goal is also to use another kinetic model and compare the results it yields with the ones obtained by the initially implemented model. The reactor model developed in the present work uses Aspen Custom Modeler® (ACM) to conduct detailed modelling of the reactor and its kinetics. One of the main advantages of using ACM over other simulation tools (Matlab, Python) is the availability of properties databases, which are already implemented in ACM. It also enables the future transfer of the model in Aspen Plus® to build a whole process around this reactor, including a reverse water-gas shift reactor, the  $H_2$  production and the separation and purification steps. Another objective is the sensitivity analyses of different variables and parameters on the behaviour and performance of the reactor. It aims at giving an insight into the effects induced by the variation of certain critical variables that will be helpful for the operation of the future lab-scale installation.

The present work starts with a brief literature review concerning the Power-to-X concept and more specifically the Fischer-Tropsch synthesis. It continues with a chapter describing more theoretical aspects concerning reactor modelling. It includes a description of the kinetic model, the stoichiometry and the product distribution obtained at the end of the reactor. The following chapter consists of an analysis of the results obtained with a validation of the kinetic model, a discussion about the results yielded by the reactor operated with base case conditions, and finally a discussion concerning different sensitivity analyses performed on various variables. The report is eventually concluded with a summary of the most significant results, and a projection of the future work concerning this project.

# Chapter II

## Literature review

### II.1 Conventional kerosene production

The conventional way of producing jet fuel is through the distillation of crude oil in classical refineries in which the kerosene fraction corresponds to boiling temperatures ranging between 205 and 260°C. In Europe, in 2020, this production accounted for 3.7% (16.4 million tonnes of oil equivalent (Mtoe)) of petroleum products leaving the refinery. For the same year, Europe's net importations of kerosene-type jet fuel were evaluated at 6.35 Mtoe ([Eurostat, 2022](#)). There also exists an unconventional way of synthesis in which the origin of the raw material is different. For instance, a small percentage of jet fuel is produced from sand oil or shale oil. However, these unconventional oils are less optimal for jet fuel production, as they require dealing with solids and are less environmentally friendly compared to the traditional synthesis from crude oil ([Liu et al., 2013](#)). Another alternative production pathway consists in producing kerosene from CO and H<sub>2</sub> through the Fischer-Tropsch synthesis in a Gas-to-Liquids (GTL) plant, as it is operated by Shell in Qatar, for instance ([Shell, 2022](#)). More details concerning this pathway are given in Section [II.3](#).

The largest producer of jet fuel and kerosene in the United States is Exxon Mobil, with 12% of the market share in 2012 ([Davidson et al., 2014](#)). The jet fuel production is not the only application for kerosene, as there is still a widespread usage of household kerosene for cooking and lighting in developing countries, estimated to be around 6.4 Mtoe/year ([Lam et al., 2012](#)). One of the first applications for kerosene was lighting, as it replaced whale oil, which was more expensive during the 19<sup>th</sup> century. Kerosene has been progressively replaced during the 20<sup>th</sup> century with electrification and availability of gas fuels ([Lam et al., 2012](#)).

The hydrocarbon chain lengths range that constitutes kerosene varies depending on the consulted source. [Doliente et al. \(2020\)](#) consider that hydrocarbons having between 10 and 18 carbon atoms are found in jet fuel, [Kallio et al. \(2014\)](#) take a broader range with the distribution varying between 6 and 16 carbon atoms, [Liu et al. \(2013\)](#) claim that a typical carbon range is C9-C15 and [Shepherd et al. \(2000\)](#) say that species between 5 and 20 carbon atoms can be found in jet fuel. The presence of hydrocarbon chains as long as 20 carbon atoms has also been measured elsewhere ([Smith and Bruno, 2007](#)). For this work, it is considered that the fraction of interest contains between 12 and 20 carbon atoms to match with the hypothesis previously taken by [Morales and Léonard \(2022\)](#). According to [Doliente et al. \(2020\)](#), the desired composition of jet fuel should be between 75 and 85 vol% of paraffins, including straight-chained, branched, and cyclic paraffins and the remaining being 15 to 25 vol% of olefins and aromatics.



## II.2 Power-to-X concept

### II.2.1 Origin of the concept

As mentioned in the introduction, one measure that must be taken to reach the objective of net zero emissions by 2050 is the progressive transition towards renewable energy sources. In 2020, it was estimated that the global primary energy demand was based at 80% on fossil fuels, which shows the extent of the effort that should be made to reach the set objectives (Panzone et al., 2020). One of the principal challenges currently imposed by the replacement of fossil-based sources with renewable energy sources is the variability of the resources compared to crude oil. The consequence of this challenge is an imbalance between the energy supply and demand, thus requiring essential storage of electricity produced from renewable sources to increase the flexibility of the energetic system. Likewise, electricity storage requires dynamic responses, high roundtrip efficiency, i.e. low energy losses, high storage density, high reliability, and maintaining power quality, frequency and voltage at low cost.

The electrical energy storage systems can be classified into different categories depending on the form under which the electricity is stored. The first category concerns electricity stored mechanically. It includes hydroelectric plants, where an altitude difference between a water reservoir and a power turbine is exploited, but also electricity stored by air compression or flywheels. Then, it is possible to convert electricity into electrochemical energy in batteries or electrical energy systems, including supercapacitors and superconducting magnetic energy storage. The last category consists in storing electrical energy in the form of chemical potential in energy carriers. The most widespread energy carrier is  $H_2$  produced by water electrolysis. It can be used to redeliver power in fuel cells, for instance, or in non-electrical sectors, including transportation, heating or industry. This last category refers to the Power-to-X concept (Buffo et al., 2019).

The power-to-X pathway encompasses a power production unit that corresponds to the renewable electricity generation, then converted inside a  $H_2$  production unit. This unit is an electrolyser in which water splits into  $O_2$  and  $H_2$ . The membrane and the species that are exchanged across this membrane differentiate the various electrolysis cells. The conventional cells are the alkaline and the proton exchange membrane electrolysers, which are mature technologies. It is also possible to find the solid oxide electrolyte and the anion exchange membrane electrolysis. The produced  $H_2$  can then directly be used or further converted, generally by reacting with  $CO_2$  previously captured in flue gases or directly in the atmosphere. The nature of the product yielded or its utilisation determine the 'X' that appears in Power-to-X, including Power-to-Gas, Power-to-Liquids, Power-to-Chemicals and Power-to-Heat, which are reviewed below (Koj et al., 2019; Léonard, 2021b). Instead of reacting with captured  $CO_2$ , the produced  $H_2$  can also react with other molecules, namely  $N_2$  to produce  $NH_3$ , as discussed in Section II.2.4

### II.2.2 Power-to-Gas

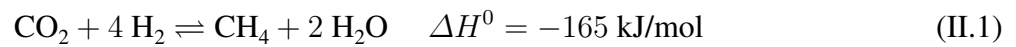
#### II.2.2.a Power-to-Hydrogen

The Power-to-Gas category includes three dominant  $H_2$  validation pathways. The first one is called Power-to-Hydrogen and consists in directly utilising the produced  $H_2$ . It concerns the transportation sector with the development of fuel cells, for instance, but also the industrial sector. Supplying industries for which  $H_2$  is already a raw material with this renewable source of  $H_2$  is of high interest, as

it is currently produced by hydrocarbon reforming or gasification. The concerned industries include mainly ammonia synthesis and refineries in which H<sub>2</sub> is used for hydrocracking and gas purification. From a practical point of view, the objective is to use the already existing natural gas pipelines to transport H<sub>2</sub> when the natural gas reserves are depleted. It is already possible to use these pipelines by enriching natural gas with up to 10% of H<sub>2</sub> from which it is further separated using membranes, adsorption or other technologies (Hu et al., 2020). H<sub>2</sub> can also directly be used in cogeneration plants, where the idea is to progressively replace the traditional natural gas with H<sub>2</sub> to generate heat and electricity. A pilot project is currently conducted by INEOS and ENGIE in Doel (Clarion Energy Content Directors, 2021). It can also replace natural gas in combined cycle gas turbine (CCGT) plants (Oberg et al., 2022).

### II.2.2.b Power-to-Methane

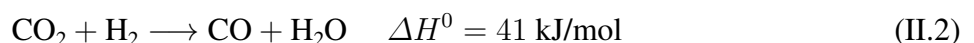
The second validation pathway for H<sub>2</sub> in the Power-to-Gas category is the Power-to-Methane. H<sub>2</sub> reacts with CO<sub>2</sub> to form methane and water in the so-called Sabatier reaction:



This reaction represents the chemical synthesis of methane, but it is also possible to biologically produce methane, which is then known as biogas production. This biological route enables an operation at low temperature (30-60°C) and atmospheric pressure. On the other side, it suffers from slow kinetics and poor mass transfer performance. CO is a by-product of the Sabatier reaction, but its formation can be minimised at low temperature and high pressure. There are various reactor types in which the Sabatier reaction can be carried out, including fixed-bed reactors, which are mostly used in the industry. There are few Power-to-Methane plants currently in operation, but the biggest one, the Audi e-gas plant, is located in Germany, where the produced methane is fed into the natural gas grid (Ghaib and Ben-Fares, 2018). In Belgium, the Columbus Project regrouping ENGIE, Carmeuse and John Cockerrill aims at capturing CO<sub>2</sub> generated during lime production to produce methane (ENGIE Laborelec, 2022).

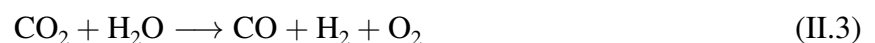
### II.2.2.c Power-to-Syngas

Syngas is conventionally synthesised by coal gasification or steam reforming of fossil-based liquids and natural gas, which are considered polluting pathways regarding greenhouse gas emissions. The Power-to-Syngas concept is thus an interesting alternative, achievable in different ways. A first solution is to react CO<sub>2</sub> with H<sub>2</sub> through the rWGS reaction:



This pathway thus requires the utilisation of H<sub>2</sub> that must be produced by water electrolysis to remain in the Power-to-X scope (Foit et al., 2017). As can be seen from its reaction enthalpy value, the rWGS reaction is endothermic and must be operated at a temperature above 700°C. Below this temperature, the reaction yields methane as a by-product. There is not yet an industrial-scale process for this pathway that requires improvements in terms of energy efficiency (Schwab et al., 2015).

Another way to produce syngas through the Power-to-Syngas concept is the direct one-step co-electrolysis of water and CO<sub>2</sub>:





The advantage of this pathway is that  $\text{H}_2$  and  $\text{CO}$  are both synthesised within the same unit. In contrast, in the rWGS route,  $\text{H}_2$  needs first to be produced in an electrolysis cell, and then a fraction of this  $\text{H}_2$  is used to react with  $\text{CO}_2$  in the rWGS reaction. However, the combined synthesis of  $\text{CO}$  and  $\text{H}_2$  within the same unit through the co-electrolysis technology is still at a low maturity level (Peters et al., 2022).

The last synthesis route is the direct electrochemical reduction of  $\text{CO}_2$ :



This reaction can be operated within solid oxide electrolysis, molten carbonate electrolysis or low-temperature electrolysis, ranging by decreasing order of maturity level. The solid oxide electrolysis has been demonstrated in an operational environment, and a fully industrial plant is estimated by 2029 (Küngas, 2020). This syngas production pathway requires a secondary  $\text{H}_2$  source but offers the possibility of regulating the  $\text{H}_2/\text{CO}$  ratio by adapting the productivity of both production processes. It is an important feature, as this ratio determines the field of application for the syngas. A 1:1 ratio is relevant for the oxo synthesis, producing aldehydes and oxo-alcohols. Between 1:1 and around 2:1 ratios, the syngas is mainly used as a reagent in the Fischer-Tropsch or alcohol syntheses. A 3:1 ratio is suitable for the methanation reaction in synthetic natural gas production (Foit et al., 2017).

## II.2.3 Power-to-Liquids

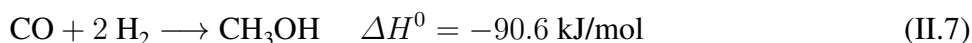
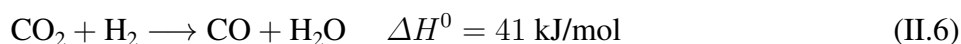
The storage of renewable electricity in liquid fuels presents several advantages compared to gaseous fuels and is generally the preferred solution for medium- and long-term storage. Liquid fuels are easier to store and transport compared to gaseous fuels that need to be compressed or liquefied, they have a higher energy density per unit volume, have lower mass loss induced by long-term storage and are easily extracted from the reactor (Panzone et al., 2020). The production of methanol, DME and Fischer-Tropsch fuels is discussed. On top of these carbon-based fuels, other fuels can be produced from  $\text{H}_2$ , including ammonia, which is synthesised from  $\text{H}_2$  and  $\text{N}_2$ . Sustainable ammonia production is further discussed in Section II.2.4. Note that the scope of this master's thesis focuses on the production of Fischer-Tropsch fuels.

### II.2.3.a Power-to-Methanol

While methanol is currently produced in a catalytic process using natural gas, the idea of the Power-to-Methanol concept is to convert  $\text{CO}_2$  and  $\text{H}_2$  in methanol and water using a highly selective catalyst, such as Cu promoted with another metal (Panzone et al., 2020):



but  $\text{CO}_2$  can also react with  $\text{H}_2$  with a different stoichiometric ratio through the rWGS reaction yielding  $\text{CO}$  and water. The  $\text{CO}$  formed can further react with  $\text{H}_2$  to produce additional methanol:



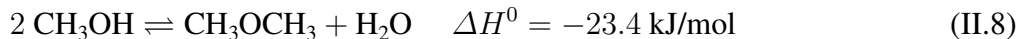
This synthesis pathway is carried out at around  $250^\circ\text{C}$  and a pressure ranging between 50 and 100 bar. Regarding the above equations, it turns out that methanol can be synthesised directly from syngas. It means that the Power-to-Methanol route can be a validation option for syngas produced in

the Power-to-Syngas pathway. There is currently only one commercial plant located in Iceland and commissioned by Carbon Recycling in 2012 with an annual capacity of 4000 tonnes of methanol (Dieterich et al., 2020; Léonard, 2021b).

There are several advantages to storing renewable electricity in the form of methanol, including its ease of storage, as it is liquid under normal conditions. It produces almost zero emissions of NO<sub>x</sub> and SO<sub>x</sub>, and it can be easily converted into a large panel of relevant compounds, including gasoline or light olefins, for instance (Panzone et al., 2020). The methanol-to-olefins reaction specifically receives interest as it enables to yield light olefins, which are at the very basis of the petrochemical industry. Producing light olefins from methanol, which is produced within the Power-to-Methanol scope, would mean that the whole petrochemical industry could theoretically be shifted from a crude oil-based synthesis towards a renewable energy-based production. Therefore, the topic is the subject of numerous studies that focus on catalyst improvements, as catalysis is one of the critical constraints for this process. The selectivity towards light olefins constitutes a significant challenge, requiring the utilisation of specific catalysts, including zeolites and molecular sieves (Yang et al., 2019; Alshafei et al., 2021; Zhong et al., 2021).

### II.2.3.b Power-to-DME

Dimethyl ether (DME) is traditionally produced by methanol bimolecular dehydration on a solid acid catalyst. Concerning its synthesis through the Power-to-DME pathway, two routes are distinguished. The first possibility is a two-step process in which methanol is produced from CO<sub>2</sub> and H<sub>2</sub>, as described above, and where methanol is secondly dehydrated on an acid catalyst:



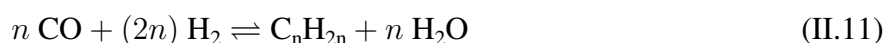
The second possibility consists in a one-step process where methanol is only an intermediate and where a bi-functional catalyst is used. One part of the catalyst is metallic to promote the methanol formation and the other part is acid to promote the dehydration:

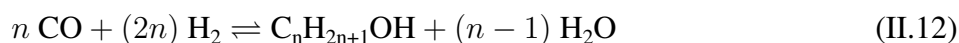


Albeit this alternative is hardly applied industrially, given the catalyst deactivation caused by water, it constitutes the preferred option because of its lower thermodynamic limitations and lower cost (Panzone et al., 2020). The interest in producing green DME is high, as it can be used as a substitute for liquefied petroleum gas (LPG), a green solvent, a refrigerant or a propellant. It also finds its application as a green fuel to replace diesel, given its high cetane number. It requires some tank and injection system modifications, as DME is gaseous at ambient conditions. Other usages of DME are found in fuel cells and as a raw material for other processes (Semmel et al., 2021).

### II.2.3.c Power-to-Fischer-Tropsch-fuels

The Fischer-Tropsch synthesis is a well-known reaction for almost a century, as the results concerning this reaction were published in 1923 by Fischer and Tropsch (1923). The synthesis consists in the formation of a wide range of hydrocarbons, including paraffins and olefins, as well as oxygenated species from syngas on a Co or Fe catalyst:





The optimal  $\text{H}_2/\text{CO}$  ratio for Co-based catalysts is found around 2, while Fe-based catalysts tolerate lower values. The chain length distribution of Fischer-Tropsch products follows the Anderson-Schulz-Flory (ASF) distribution, which is fully detailed in Section III.3 (Dieterich et al., 2020). More details concerning the catalysts, the kinetics and the reactor for this reaction are given below, as this reaction is at the heart of this work.

Figure II.1 depicts a schematic representation of the Power-to-Fischer-Tropsch technology. It shows the feedstock origin, including  $\text{H}_2$  produced by water electrolysis powered by renewable energies and  $\text{CO}_2$  captured in the industry or directly in ambient air (see Steps 1 and 2 in Figure II.1). Equations II.10 to II.12 illustrate the presence of various products. This project focuses on kerosene synthesis intended for aviation fuel utilisation, but other products are valuable to a lower extent. Figure II.1 shows one of them, i.e. synthetic gasoline, but the naphtha fraction can also be validated as a substitute in the petrochemical industry (Carnall et al., 2022). The Power-to-Fischer-Tropsch fuels technology often exhibits residual heat, given the significant exothermicity of the reactions. For instance, this waste heat can be recovered within the global process or distributed through a district heating network in nearby neighbourhoods for residential heating purposes. Figure II.1 also depicts the cyclical nature of the technology. Once captured,  $\text{CO}_2$  emissions inevitably resulting from the utilisation of the products become the feedstock for the process.

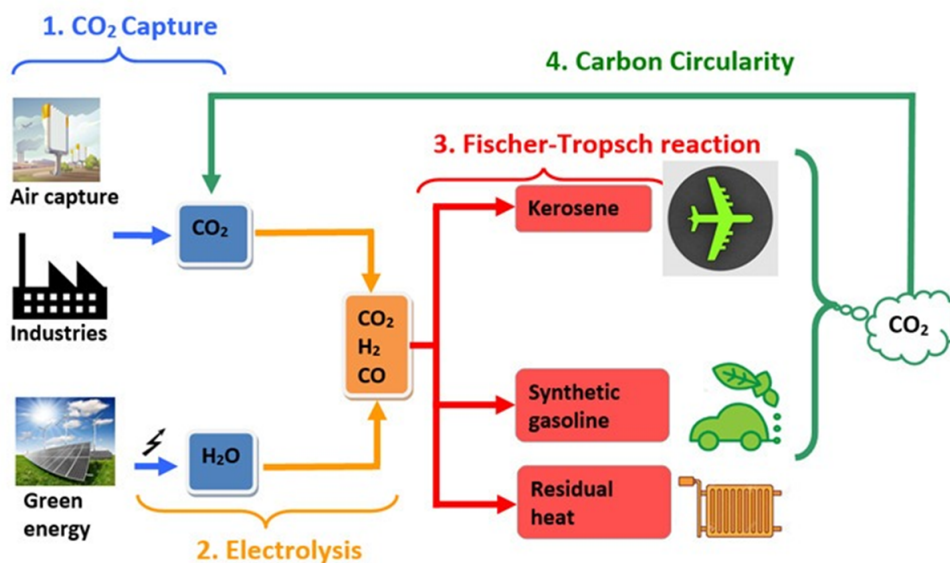


Figure II.1: Schematic representation of the Power-to-Fischer-Tropsch technology (Léonard, 2021b)

It is interesting to mention that liquid hydrocarbons can be produced through the FT or the methanol pathway. In the methanol pathway, methanol is produced as described in Section II.2.3.a and then further transformed to liquid hydrocarbons, including DME and gasoline, for instance. Both pathways exhibit a direct alternative in which  $\text{H}_2$  reacts with  $\text{CO}_2$  to form liquid hydrocarbons in a one-step process where CO or methanol is an intermediate. The other possibility is an indirect alternative where CO is formed through the rWGS reaction and is then sent to a FT reactor, or where methanol is formed by the reaction of  $\text{CO}_2$  with  $\text{H}_2$  followed by a Methanol-to-Liquids unit. The direct pathways are often more challenging, as they require the utilisation of bi-functional catalysts which can carry out both reactions of the indirect pathways in a single unit (Panzone et al., 2020).

## II.2.4 Power-to-Chemicals

The concept of Power-to-Chemicals consists in storing renewable electricity in various chemicals. This pathway generally goes through a CO generation step from CO<sub>2</sub>. It is achieved using the rWGS reaction or the co-electrolysis of water and CO<sub>2</sub>. Another solution is to synthesise methanol. Regarding the review presented above concerning Power-to-Gas and Power-to-Liquids, the chemicals produced through the Power-to-Chemicals route could easily be associated with one of the two previously presented categories. However, it is possible to yield chemicals within the Power-to-Chemicals scope without going through a preliminary CO or methanol production. A relevant chemical to be produced within such a route is ammonia (Power-to-Ammonia). It is currently produced through the Haber-Bosch process in which N<sub>2</sub> reacts with H<sub>2</sub>, mainly stemming from steam reforming of natural gas. The environmental impact of conventional NH<sub>3</sub> production is thus crucial in motivating the research of an alternative ([Ince et al., 2021](#)).

Nowadays, 80% of ammonia production is used by the fertiliser industry. It also finds some applications as feedstock for nitric acid synthesis, as a refrigerant or as a fuel. The point of producing nitrogen-based chemicals is that they contain nitrogen, which is abundant in the atmosphere and easier to obtain from an energetic and economic point of view compared to CO<sub>2</sub>. Ammonia can be used to power fuel cells, its combustion does not yield any CO<sub>2</sub> and the emission of nitrous oxides can be avoided by catalytic decomposition of NH<sub>3</sub> to burn H<sub>2</sub> in fuel cells or gas turbines. Ammonia can even be further transformed in hydrazine (N<sub>2</sub>H<sub>4</sub>), ammonia carbonate ((NH<sub>4</sub>)<sub>2</sub>CO<sub>3</sub>) or urea (CO(NH<sub>2</sub>)<sub>2</sub>), which can serve as ammonia storage solutions, indirect H<sub>2</sub> storage or even directly be used in appropriate fuel cells ([Ikäheimo et al., 2018](#)). Among all the applications, the utilisation of NH<sub>3</sub> as an alternative fuel is recently the focus of various studies ([Al-Aboosi et al., 2021](#); [Xu et al., 2022](#)).

## II.2.5 Power-to-Heat

The Power-to-Heat technology consists in converting renewable electricity into thermal energy. There are two mature technologies for this purpose, which are the heat pump or electric boilers being used for residential heating, as well as for industrial applications ([Koj et al., 2019](#)).

## II.3 Fischer-Tropsch synthesis

As mentioned previously, the Fischer-Tropsch synthesis is a well-known reaction. The world's largest facility implementing Fischer-Tropsch technology is the Secunda plant in South Africa, operated by Sasol. They produce 150,000 barrels of fuels and petrochemicals each day. The process is qualified as a Coal-to-Liquids process, as they yield liquid products through coal gasification, which is followed by the Fischer-Tropsch synthesis ([van Dyk et al., 2006](#)). In the previous section, it is explained that the Power-to-Fischer-Tropsch technology is an appealing option for CO<sub>2</sub> emissions abatement. However, the historical utilisation of Fischer-Tropsch synthesis, such as in the Secunda plant, is far from being considered environmental-friendly, given their feedstock origin. In 2018, Greenpeace Africa labelled the Secunda plant as "the world's biggest single-point source of emissions" ([Lee, 2020](#)). Shell operates two other important Fischer-Tropsch facilities. The Shell Middle Distillate Synthesis (MDS) process is operated in Bintulu, Malaysia, and their Pearl Gas-to-Liquids plant is located in Qatar ([Shell, 2022](#)).

### II.3.1 Type of catalysts used

The Fischer-Tropsch synthesis is a reaction which can theoretically be catalysed by numerous transition metals, including Ru, Fe, Co, Rh, Ni, Ir, Pt or Pd. Pd, Pt and Ir have a too high selectivity for the methanation reaction ([Mousavi et al., 2015](#)), while Ni is not considered as a Fischer-Tropsch synthesis active metal, given its poor selectivity profile. However, some studies aim to use a bimetallic catalyst, including nickel ([Li et al., 2014](#); [van Helden et al., 2020](#)). Ru is technically the most active transition metal towards Fischer-Tropsch synthesis, but its high cost and limited reserves prevent its industrial application ([Zhang et al., 2010](#)). These transition metals which are not suitable for industrial application of Fischer-Tropsch synthesis are used as promoters on Co-based catalysts ([Khalighi et al., 2020](#); [Sonal et al., 2020](#)).

#### II.3.1.a Cobalt-based catalysts

Cobalt-based catalysts are generally preferred to iron-based catalysts in the case where the goal is to produce long-chain hydrocarbons. These catalysts also present the advantage of being almost inactive towards the water-gas shift reaction:



unlike iron, which is active in this reaction. Cobalt catalysts yield less oxygenated species and are more stable in the presence of water ([Adeleke et al., 2020](#)). Several parameters influence the performance of cobalt-based catalysts, namely the particle size, the support type, the preparation method, the promoter used,...

Generally, catalyst supports are used, as they facilitate active metal particles crystallisation and stabilisation. The metal-support interactions are crucial, as they have an impact on the structure and electron density of metal particles that could yield to the formation of cobalt-support mixed compounds. The support also plays a determining role concerning heat dissipation in fixed-bed reactors. One of the most commercially widespread cobalt-based catalysts is the Co/Al<sub>2</sub>O<sub>3</sub>. It presents, among others, excellent mechanical properties and high attrition resistance. It also seems that the support pore size influences the size of Co particles: wide pores leads to large particles and narrow pores to smaller particles ([Borg et al., 2007](#); [Gholami et al., 2021](#)). Silica-supported catalysts are also widely used, offering the advantage of weaker metal-support interactions compared to alumina supports. It enhances the reduction of cobalt particles and thus increases the number of active sites. Another support material which can be found is TiO<sub>2</sub>, which presents considerable thermal and chemical stability and high corrosion resistance. Zeolites are interesting for gasoline production due to their capacity to enhance the octane number through their shape-selectivity feature. Finally, carbon-based materials exhibit weak metal-support interactions and are cheap ([Gholami et al., 2021](#)).

As explained before, one of the main disadvantages of catalyst supports is their interaction with metal particles, hindering their reduction and thus decreasing the number of active sites. A solution to solve this issue is to use promoters, presenting a lower reduction temperature than cobalt particles. It enables them to catalyse cobalt reduction by lowering its reduction temperature ([Jacobs et al., 2002](#)). The nature of the promoters can vary, and noble metals can be used, namely Pt, Ru or Ir. Small amounts are generally used, between 0.1 and 0.5 wt%, on one side because of their relatively high cost and on the other side because a too large amount may cause a blocking of cobalt-active sites. Transition metals, often in the form of oxides, are also used as promoters to adjust the metal-support interactions. Finally, it is also possible to use alkali earth metals (Li, Na, K, etc). They affect the



electronic density of the transition metal because of their strong basicity, inducing a positive effect on CO chemisorption and dissociation (Gholami et al., 2021).

### II.3.1.b Iron-based catalysts

Iron-based catalysts present the advantage of being cheaper compared to cobalt-based ones. They also can be used in a wider temperature range, while cobalt is preferentially not used at high temperatures where its methane selectivity becomes significant. On the other side, iron-based catalysts are less resistant to deactivation and catalyse the water-gas shift reaction. In this reaction, CO reacts with water, the by-product of FT synthesis, to form  $\text{CO}_2$  and  $\text{H}_2$ . It may be an advantageous feature when the syngas ratio is not optimal. Therefore, it enables the FT synthesis to be operated in a wider range of inlet syngas ratios, whereas cobalt-based catalysts must be used with syngas ratio values close to 2 (Abelló and Montané, 2011). The reasons for Fe-based catalysts deactivation may be the conversion of active phases into less active or inactive phases by oxygenation, deposition of inactive carbonaceous species on the iron phase, sintering or poisoning by sulphur compounds (Smit and Weckhuysen, 2008).

Bulk iron catalysts can be used for Fischer-Tropsch synthesis. However, they can become unstable under the conditions of catalyst activation or at high temperatures. Utilising supports for iron-based catalysts enables their mechanical stability enhancement, the more efficient use of the active phase and the increase in the catalytic activity. The suitable supports for iron-based catalysts are mainly limited to classical oxidised supports, including  $\text{SiO}_2$ ,  $\text{Al}_2\text{O}_3$  or  $\text{TiO}_2$ , but also mixed oxides, such as zeolites. It is also possible to find carbon-based supports, such as activated carbon, carbon nanotubes or carbon spheres (Sun et al., 2012; Cheng et al., 2015). The interactions between the support and the metal particles are consequential, as it stabilises the iron dispersion. Too strong interactions can lead to mixed support-metal species formation, these species being difficult to reduce and thus inactive. The porosity of the support also impacts the catalytic performance, but very few studies are available for supported-iron catalysts (Cheng et al., 2015).

The utilisation of promoters in iron-based catalysts is of interest to improve their selectivity. They affect the iron dispersion, the iron carbidisation (as iron carbide is assumed to be the active phase (Sun et al., 2012)) and the electronic properties of the active species. The promoters are mainly alkali metals and copper (Barrios et al., 2020).

## II.3.2 Reaction mechanisms

The scope of this work is not to study in detail the kinetics of the Fischer-Tropsch synthesis with a deep understanding of the mechanisms governing the reaction. However, it is still of interest to give an overview of the possible mechanistic routes, as the topic is the focus of several discussions (Mousavi et al., 2015; Mahmoudi et al., 2018; Teimouri et al., 2021).

The Fischer-Tropsch synthesis is a polymeric surface reaction including the following steps (Laan and Beenackers, 1999):

1. Reactants adsorption at the catalyst surface
2. Chain initiation
3. Chain growth
4. Chain termination

## 5. Products desorption

## 6. Possible products readsorption and further reaction (hydrogenation of $\alpha$ -olefins, isomerisation,...)

The differences in the proposed mechanisms come from the variety of surface monomeric species proposed to describe chain initiation and growth. The three monomers most often considered are methylene ( $\text{CH}_2$ ), enol species ( $\text{HCOH}$ ) and CO, giving rise to the three corresponding mechanisms: carbide, enol and CO insertion mechanism, respectively (Mousavi et al., 2015). These three mechanisms are briefly discussed below.

### II.3.2.a Carbide mechanism

Initially proposed by Franz Fischer and Hans Tropsch, the carbide mechanism starts with dissociative adsorption of CO at the catalyst surface. The two atoms resulting from this dissociative adsorption, i.e. C and O, are hydrogenated by  $\text{H}_2$  to form methylene species and water. The polymerisation proceeds by insertion of the monomer in a growing alkyl chain. For the termination step, two alternative routes are considered: the desorption of an unsaturated intermediate giving olefins or the addition of a  $\text{CH}_3$  species or  $\text{H}_2$  resulting in paraffins. A schematic representation of the different steps is proposed in Figure II.2.

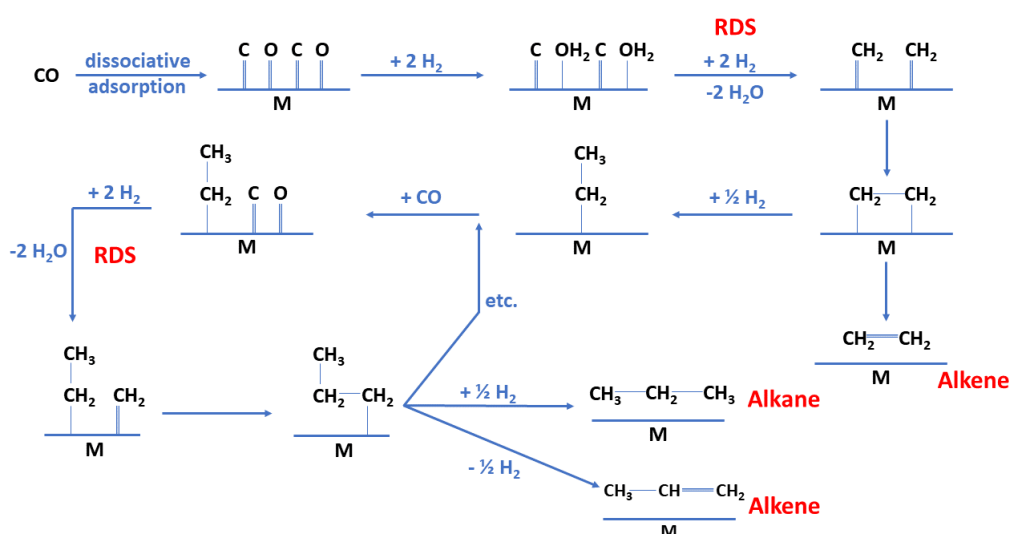


Figure II.2: Schematic representation of the carbide mechanism (inspired by Shafer et al. (2019) and Teimouri et al. (2021))

The rate-determining step (RDS) of this mechanism is the hydrogenation of carbon and oxygen atoms coming from CO molecules and resulting in methylene species and water (Shafer et al., 2019; Teimouri et al., 2021). Although this mechanism has been widely proposed in the literature, it seems that methylene intermediates cannot undergo self-polymerisation, which suggests the intervention of other monomers and initiators. For this reason, some mechanisms were proposed based on a modification of the carbide mechanism, including, for instance, a  $\text{H}_2$ -assisted CO dissociation (Teimouri et al., 2021).

### II.3.2.b Enol mechanism

This alternative mechanism proposes non-dissociative adsorption of CO molecules. The adsorbed CO is then hydrogenated to form enol species which act as monomers. The product chain growth is induced by a condensation reaction between two adjacent enol species, leading to the elimination of a water molecule. The termination occurs by the enol group hydrogenation in the growing chain, which is eliminated as water. The enol mechanism is represented in Figure II.3. The rate-determining step for this mechanism is the hydrogenation of adsorbed CO molecules. This mechanism successfully explains the presence of oxygenated compounds in the product spectrum (Shafer et al., 2019; Teimouri et al., 2021).

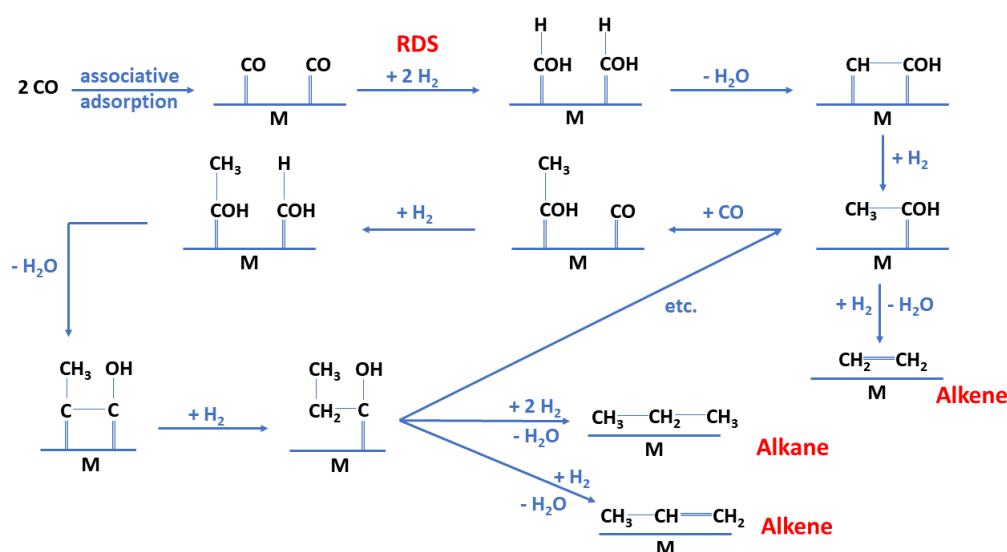


Figure II.3: Schematic representation of the enol mechanism (inspired by Shafer et al. (2019) and Teimouri et al. (2021))

### II.3.2.c CO insertion mechanism

In the CO insertion mechanism, as depicted in Figure II.4, the CO molecule acts as the monomer for the chain propagation. In this model, CO is inserted at a metal-hydride bond, which is the case for the initiation, or at a metal-alkyl bond during chain growth. The inserted CO is then hydrogenated with a  $H_2$  molecule to form a new methylene group in the growing chain and a water molecule. The termination either implies a  $H_2$  molecule resulting in a paraffin formation or not, then giving an olefin. Similarly to the two other proposed mechanisms, the rate-determining step is the hydrogenation of CO to a methylene group  $CH_2$  (Shafer et al., 2019; Teimouri et al., 2021).



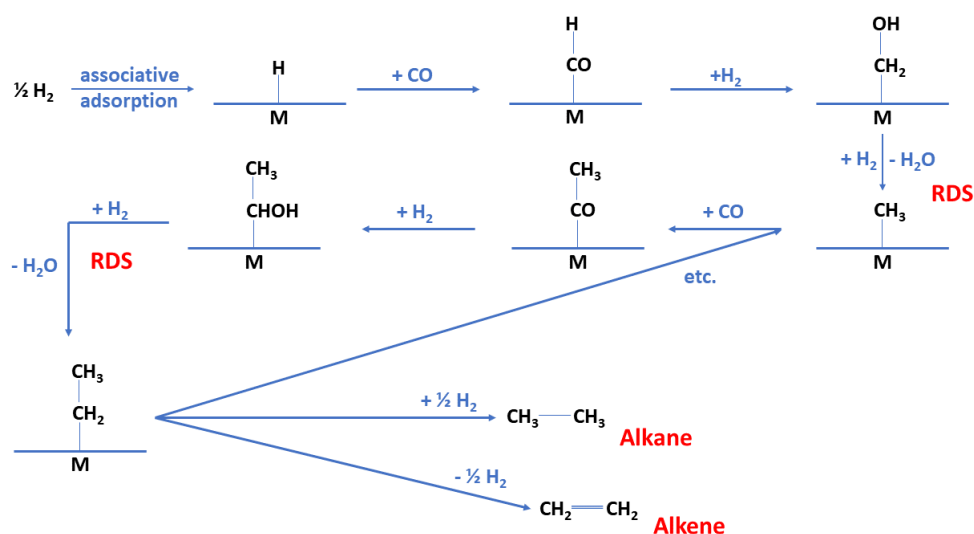


Figure II.4: Schematic representation of the CO insertion mechanism (inspired by [Shafer et al. \(2019\)](#) and [Teimouri et al. \(2021\)](#))

### II.3.3 Reactor configurations

There are four main reactor configurations for Fischer-Tropsch synthesis which are referenced in the literature: the circulating fluidized bed reactor, the fluidized bed reactor, the tubular fixed-bed reactor and the slurry phase reactor ([Dieterich et al., 2020](#)). These four options are used in two different alternative processes: the low-temperature and the high-temperature Fischer-Tropsch process (LTFT and HTFT, respectively). The fixed-bed and slurry phase reactors are used at low temperatures, ranging from 220 to 240°C and pressures between 20 and 25 bar ([Dieterich et al., 2020](#)). It happens that low-temperature reactors are operated at a slightly higher temperature than 240°C ([Steynberg et al., 2004](#)). These low-temperature reactors are characterised by the potential presence of three phases: the gaseous reagents and part of the products, another part of the products that are liquids (waxes) and the solid catalyst. The low-temperature reactor can be operated with both Co and Fe-based catalysts and yields generally long-chained products ([Dry, 2002](#); [Dieterich et al., 2020](#)). On the other side, the circulating and non-circulating fluidised bed reactors fall in the high-temperature Fischer-Tropsch category. They are mainly operated at a temperature varying between 320 and 350°C, as a higher temperature would induce a significant carbon deposition on the catalyst ([Steynberg et al., 2004](#); [Dieterich et al., 2020](#)). They are operated in the same pressure range as the LTFT process with exclusively Fe-based catalysts, as the utilisation of Co-based catalysts at this temperature would induce a too large methane selectivity. The products yielded at high temperature are typically shorter than at low temperature, which is induced by the ASF distribution they follow (see Section [IV.2.1](#)).

#### II.3.3.a Fixed-bed reactor

As shown previously, the Fischer-Tropsch synthesis is a highly exothermic reaction. Then, the evacuation of the heat released by the reaction towards the cooling medium is paramount to avoid hot spots and adverse effects induced by temperature rises. Thus, classical vertical spaced packed-bed or adiabatic reactors with inter-stage cooling are unsuitable for packed-bed reactors. The favoured configuration is a multi-tubular packed-bed reactor with the catalyst inside the tubes ([Steynberg et al., 2004](#)). Figure [II.5](#) shows a representation of this type of reactor.

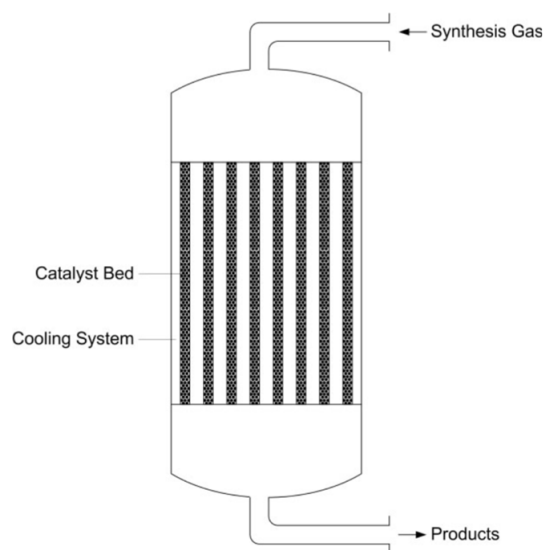


Figure II.5: Illustration of a multi-tubular packed-bed reactor (Guettel et al., 2008)

The utilisation of such reactors presents the advantage of being easy to manufacture and facilitating the design transition from one tube to several tubes. They do not require a separation of the liquid products and the catalyst performance is predictable from the results of tests performed on lab-scale reactors. However, the catalytic bed is composed of large catalyst particles to avoid too nefast pressure drop, which has a negative impact on intra-particles transport properties. On an industrial scale, where the tube diameters are large, the apparition of hot spots is possible, which is detrimental to the catalyst. Their manufacturing cost is also generally consequential. The way of cooling brings an inherent problem of the apparition of axial and radial temperature gradients affecting the conversion. This issue is mitigatable by recirculating unreacted syngas, which enhances the overall conversion and increases the gas velocity, which is beneficial for heat transfer (Steynberg et al., 2004; Guettel et al., 2008; Knutsen, 2013). Shell applies this technology in their MDS process in Bintulu, Malaysia, which was the first-ever GTL commercial plant (Shell, 2022).

### II.3.3.b Slurry phase reactor

As previously mentioned, catalyst particles of fixed-bed reactors should not be too small to avoid large pressure drops across the reactor, but this may have a deleterious effect on mass transfer resistances inside the particles. A possible alternative is a slurry phase reactor, as represented in Figure II.6.

In slurry phase reactors, the catalyst particles are in a suspension with dimensions ranging from 10 to 200  $\mu\text{m}$ , leading to negligible mass transfer resistances. The suspension medium consists of the liquid products, which act as the heat carrier as well (Dieterich et al., 2020). This feature enhances the catalyst utilisation, inducing better productivity and selectivity. This type of reactor enables a nearly isothermal operation because of the presence of internals for better heat dissipation, which means that it can operate at a higher temperature. There is a lower pressure drop compared to fixed-bed reactors and a better cost efficiency (Steynberg et al., 2004; Guettel et al., 2008). Another important aspect of this reactor configuration is the possibility for online catalyst replacement (Steynberg et al., 2004).

However, significant aspects have hindered the development of this reactor on an industrial scale, including the separation of fine and friable catalyst particles from liquid products and its complicated scale-up (Steynberg et al., 2004; Guettel et al., 2008). This technology is notably operated by Sasol

through its Sasol Slurry Phase Distillate™ process, which is the core of their GTL technology (Sasol, 2022).

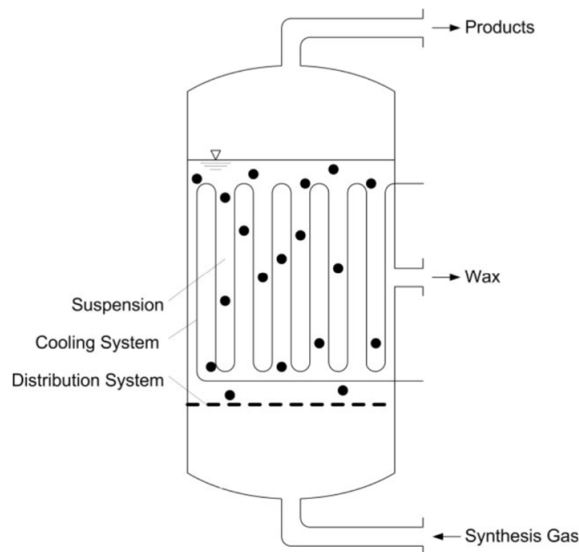


Figure II.6: Illustration of a slurry phase reactor (Guettel et al., 2008)

### II.3.3.c Circulating fluidized bed reactor

One example of this reactor configuration is the Synthol reactor, developed by Sasol (Steynberg et al., 2004). Figure II.7 proposes an illustration of a circulating fluidized bed reactor.

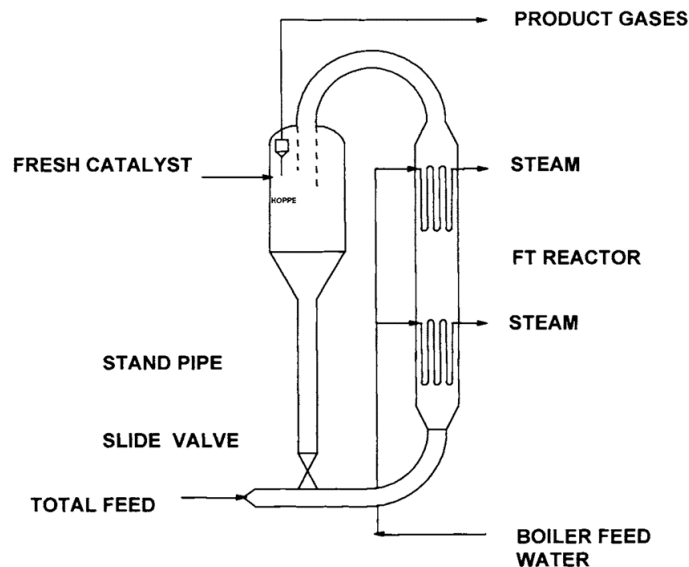


Figure II.7: Illustration of a circulating fluidized bed reactor (Steynberg et al., 2004)

As can be seen in this figure, the reactor is composed of two sections. It includes the reaction section where the syngas is converted to Fischer-Tropsch products and a stand pipe where the catalyst is recirculated at the entrance in the fresh feed gas. At the top of the reactor section, the catalyst, which is entrained by the gas, is separated from this stream by a cyclone. An important design aspect

concerning this reactor configuration is that the pressure difference in the stand pipe should always exceed the one in the reaction section. Otherwise, this would induce a bypass of the feed gas through the stand pipe and thus a massive catalyst loss. As no cooling system is present in the stand pipe, this bypass would create an important temperature rise damaging the catalyst (Steynberg et al., 2004).

#### II.3.3.d Fixed fluidized bed reactor

This reactor configuration, as illustrated in Figure II.8, is generally referred to as the Sasol Advanced Synthol (SAS) reactor, which was inspired by the Synthol reactor. This reactor configuration is the one found in the Sasol Secunda plant (Steynberg et al., 2004). It takes advantage of the high turbulence level induced by the fluidized bed to achieve efficient heat dissipation and thus deal with large amounts of heat released by the reaction. It also means that the reactor can operate at a higher temperature, given that it is considered fully isothermal. This reactor type requires operation conditions limiting the selectivity for long hydrocarbons which could condense in catalyst particle pores. It would result in an agglomeration of these particles and thus a de-fluidization of the reactor (Steynberg et al., 2004).

This reactor presents several advantages compared to the circulating fluidized bed: it can operate at higher pressure because of a larger reaction section, it induces less pressure drop regarding the lower gas velocity, it is cheaper and requires less maintenance (Dieterich et al., 2020). It also exhibits a higher catalyst/gas ratio, i.e. ratio of the amount of catalyst in contact with feedgas, as all the catalyst remains in the reaction section, while in the case of a circulating fluidized bed reactor, a fraction of the catalyst is in the circulation loop where it does not catalyse any reaction. The scale-up of non-circulating fluidized bed reactors is also easier (Steynberg et al., 1999). Both types of fluidized bed reactors are generally cooled down by a steam generator system, yielding 40 bar steam. The amount of heat generated in fixed fluidized bed reactors is often greater, as they present a larger diameter and thus theoretically a larger cooling coil area for heat transfer (Steynberg et al., 1999).

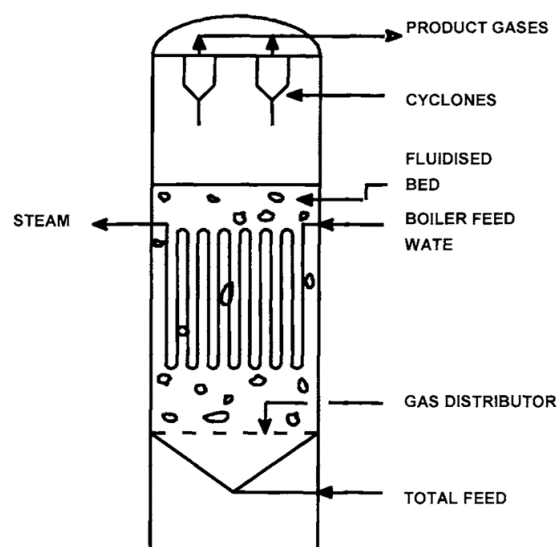


Figure II.8: Illustration of a fixed fluidized bed reactor (Steynberg et al., 2004)

## II.4 State-of-the-art of sustainable aviation fuel production

### II.4.1 Sustainable aviation fuel production pathways

As already described above, the production of sustainable aviation fuels (SAF) is achievable through the Power-to-Liquids technology. This pathway is highly trendy given its theoretically unlimited feedstock. Furthermore, the abatement of greenhouse gas emissions can be as high as 100% if the supply chain is fully decarbonised (Carnall et al., 2022). However, this technology is still in development. Other SAF production pathways exist, which are at a higher maturity level. The high feedstock cost of the Power-to-Liquids route might explain the less advanced maturity level, while the other alternatives target solid feedstock, namely biomass, which is less expensive (Wang et al., 2022).

Nowadays, the most mature technology for SAF production is the hydroprocessed esters and fatty acids (HEFA) pathway (Carnall et al., 2022). The concept underlined in this pathway is to extract free fatty acids contained in oil through a series of reactions, followed by isomerisation and hydrocracking reactions, yielding jet fuel. The feedstock for this technology consists of vegetable oils, animal fats, waste cooking oil, pyrolysis oil and algal oil (Ng et al., 2021). This technology is safe, proven and scalable, but its potential for reducing emissions only reaches up to 85% (Carnall et al., 2022).

The alcohol-to-jet (ATJ) and gasification routes are not as mature as the HEFA pathway, but they enable a 94% reduction in greenhouse gas emissions. Their development is more advanced than the Power-to-Liquids route as commercial pilots are already set up (Carnall et al., 2022). The ATJ pathway consists in the conversion of polymeric sugars contained in biomass feedstock into alcohol molecules, which are generally ethanol or isobutanol. Alcohol molecules are further treated, including dehydration, oligomerisation and hydrogenation steps, to yield the final fuel product. The sugar extraction from biomass is processed through mechanical, chemical or biological means. This pathway involves the utilisation of an engineered microorganism for the conversion of sugar into alcohol (Yao et al., 2017). The gasification pathway is similar to the Power-to-Liquids pathway, as the fuel is produced through the Fischer-Tropsch synthesis. The notable difference lies in the feedstock origin. In the Power-to-Liquids alternative, the syngas used within the Fischer-Tropsch reactor is yielded by different means, as described above, but H<sub>2</sub> most often comes water electrolysis. In contrast, syngas is produced by biomass gasification in the gasification route. This route offers a flexible biomass conversion method (Korberg et al., 2021). Instead of biomass gasification, an alternative technology consisting in biomass pyrolysis is also found in the literature (Wang et al., 2022).

### II.4.2 Scale-up challenges of the Power-to-Liquids pathway

The latest World Economic Forum's insight report (Carnall et al., 2022) gives an overview of the main challenges limiting the scaling-up of Power-to-Liquids installations. The major limiting factor is to obtain all the necessary feedstock in a single site in large quantities for an affordable price. They explain in the report that a typical commercial plant should provide around 50,000 tonnes of products per year, requiring 1.1 TWh of electricity and 169,000 tonnes of CO<sub>2</sub>. By 2025, the expected cost for one tonne of jet fuel produced through the Power-to-Liquids technology is assumed to lie between \$2400 and \$3000. Comparatively, the production cost for one tonne of fossil-based aviation fuel is around \$670 (Soone, 2020). The consequential gap between both production costs is a major obstacle to the development of large-scale Power-to-Liquids facilities.

The Power-to-Liquids aviation fuel production cost is estimated to decrease by around 50% by 2050. Significant enhancements in carbon source, hydrogen and renewable electricity production should be made to reach this objective, as they represent almost 90% of the global production cost. Thus, the production of low-cost renewable electricity should be greatly expanded. It goes through an improvement in battery technology, decreasing its cost and ensuring sufficient storage. One solution proposed to reduce the cost is to take advantage of regions offering weather conditions which enable the complementarity of wind and solar resources. A decreased cost for H<sub>2</sub> production should also positively impact the technology cost. It will be possible through the rising interest of companies in electrolysis technology, especially its scaling-up.

The privileged carbon source should be atmospheric CO<sub>2</sub> stemming from direct air capture to yield a 100% decarbonised fuel. But the technology is not yet mature, preventing large-scale operations and inducing high capture costs (between \$250 and \$600 per tonne of CO<sub>2</sub>). The falling cost and increased size of facilities will be made possible by new regulatory incentives, strategic funding and investment partnerships, and intensification of research in the domain. To a lower extent, a reduction of Power-to-Liquids cost would come along with a better maturity of fuel-synthesis technology and a consideration of the by-product markets.

On top of these technical improvements, some measures must be taken by the political authorities to incentivize the scaling-up. The cost of conventional fossil fuels should be increased to trigger the shift towards sustainable aviation fuels. The attribution of subsidies could also be a solution motivating for SAF production (Carnall et al., 2022). There are also discussions concerning the imposition of a minimum percentage of sustainable fuels in the transport sector, especially for renewable fuels of non-biological origin (RFNBO). The idea is to introduce a 2.6% target for 2030 (Wilson, 2021).

### II.4.3 European projects

In Europe, several research projects aiming at producing e-kerosene for the aviation sector have emerged in the past few years. The European Commission finances the KEROGREEN project through the Horizon 2020 research and innovation programme (H2020). The project is carried out by six partners coming from four European countries (Netherlands, Germany, Belgium, and Norway). The process approach differs from the one considered at ULiège. Air-captured CO<sub>2</sub> dissociates in a plasma reactor, which is followed by O<sub>2</sub> separation and CO purification units. Part of the CO resulting from the purification step is sent to a water-gas shift reactor to produce the required amount of H<sub>2</sub>. Then, the Fischer-Tropsch reactor and purification steps arrive. The Dutch Institute for Fundamental Energy Research (DIFFER) coordinates the whole project and is responsible for the plasma reactor study. The Karlsruhe Institute of Technology (KIT) studies the water-gas shift and Fischer-Tropsch reactions, the product upgrading section, the overall process simulation and the process sustainability. The site installation for the fully integrated KEROGREEN system is situated in KIT. The Flemish Institute for Technological Research (VITO) and Ceramic Powder Technology AS (Cerpotech), a Norwegian company, are involved in the technology used in the O<sub>2</sub> separation unit. HyGear B.V., a Dutch company, is responsible for the up-scaling of the O<sub>2</sub> separation membrane and the development of small scale CO purification modules. INERATEC, a German company, develops the FT synthesis unit and carries out the integration of the system in a container-sized module. They are also involved in process simulation and analysis and qualification of the products (KEROGREEN, 2022).

In 2021, the project start-up Synkero was launched. It aims at developing a commercial plant for the production of SAF through FT synthesis. The plant will be located in the Port of Amsterdam to



supply the Schiphol Airport through the already existing kerosene pipeline. The plant is scheduled for 2027 with a production goal of 50,000 tonnes of fuel per year. The feedstock for the synthesis is captured CO<sub>2</sub> and H<sub>2</sub> produced using renewable electricity, but the details concerning the process pathway are not yet revealed. The different partners for this project are the Royal Dutch Airlines (KLM), the Port of Amsterdam, the Royal Schiphol Group and SkyNRG, a Dutch company involved in SAF synthesis ([Synkero, 2022](#)).

Recently, an international partnership has been set up to produce SAF in Germany. The project is to combine captured CO<sub>2</sub> from a cement production factory with green H<sub>2</sub> generated with renewable energies. The consortium is composed of CEMEX, a construction materials company from Mexico, which will supply CO<sub>2</sub> from its cement factory in Rüdersdorf, Germany. ENERTRAG, a German company involved in renewable energies, will provide green H<sub>2</sub> and the Sasol Group is responsible for the Fischer-Tropsch technology ([Harrington, 2022](#)).

In Dunkerque, France, ENGIE and Infinium announced a partnership for the Reuze project. It aims at capturing CO<sub>2</sub> emitted by a ArcelorMittal's steel production plant and associating with H<sub>2</sub> produced within a 400 MW electrolyser provided by ENGIE. The targeted products are aviation and shipping fuel produced with Infinium's technology. The commercial launch of the project is planned for 2026 ([ENGIE, 2022](#)).

ULiège is involved in the neutral-kero-lime (NKL) project aiming to produce e-kerosene. The objective is to have an industrial-scale plant of 250 ML/year of e-kerosene by 2035, representing 40% of the current Liège Airport annual consumption. The consortium is composed of various partners, including Liège Airport, ULiège, UMons, Lhoist, RESA, Fluxys, ENGIE Laborelec and Hamon ([Orban et al., 2021](#)).

# Chapter III

## Fischer-Tropsch reactor modelling

This chapter aims to present the structure of the Fischer-Tropsch reactor model. The model focuses on a low-temperature Fischer-Tropsch synthesis taking place in a packed-bed reactor with cobalt-based heterogeneous catalysis. This model was developed using the simulation software Aspen Custom Modeler<sup>®</sup> along with Aspen Properties<sup>®</sup> and its associated databases to calculate the physical properties of the compounds ([Aspen Technology Inc, 2022](#)). One of the reactor built-in models available in Aspen Plus<sup>®</sup> could have been used, unfortunately, none of the proposed kinetic models correctly fit the one used in this study, and the complex stoichiometry of the reaction would have been too complicated to implement. Furthermore, Aspen Custom Modeler<sup>®</sup> offers more flexibility in terms of modelling possibilities. The transfer of the reactor model from ACM to Aspen Plus<sup>®</sup> thus constitutes the next goal to include the reactor in a complete sustainable kerosene production process.

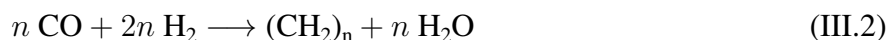
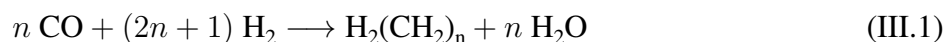
The starting point for the modelling of this reactor is a recent article written by [Meurer and Kern \(2021\)](#) in which they describe a sustainable kerosene production process. The kinetic model that they implemented, which is used in this study as well, was derived by [Ma et al. \(2014a,b\)](#). [Meurer and Kern \(2021\)](#)'s article seems to be a relevant starting point for this work as their goal are similar to the ones pursued during this master's thesis. They developed a reactor model aimed at being incorporated into a complete Power-to-Liquids process, as it is the case for this work. They give a particular interest to studying the influence of critical parameters on reactor behaviour, which is done for this work as well in Section IV.4. However, it should be noted that this work takes a certain distance to [Meurer and Kern \(2021\)](#)'s model, in particular, because the stoichiometry is differently implemented, given uncertainties concerning this point in their work. Furthermore, their work is not used to validate the kinetic model, which is instead directly validated using [Ma et al. \(2014a,b\)](#)'s experimental data, as described in Section IV.1.

### III.1 Reactions and thermodynamics

The Fischer-Tropsch synthesis leads to a wide range of products which are mainly straight-chained paraffins for which the length can theoretically vary from one to an infinite number of carbon atoms. On top of these paraffins, linear olefins, isomerised and cyclic hydrocarbons are also produced. Oxygenated species, such as ketones, alcohols, aldehydes or acids complete the product spectrum. These oxygenated species only represent a small fraction of the product spectrum, which is mainly dominated by the presence of straight-chained paraffins and linear olefins ([Shafer et al., 2019](#)). For this reason, the modelling of the Fischer-Tropsch synthesis performed in this work only accounts for the formation of straight-chained paraffins and linear  $\alpha$ -olefins, as it is done in similar simulation studies



(Panahi et al., 2012; Meurer and Kern, 2021). In addition, it is shown that the formation of aromatics only takes place in high-temperature Fischer-Tropsch synthesis and that the production of oxygenated species is negligible (less than 2 wt-%) for cobalt-based low-temperature synthesis (de Klerk, 2012). The formation of the two product categories which are studied in this work are thus represented with reactions III.1 and III.2:



It should be specified that the water-gas shift reaction:



could take place in the reactor. However, it is not catalysed on cobalt catalysts and is thus negligible (Yates and Satterfield, 1991; Panahi et al., 2010) and not included in the reactor model.

Looking at Equations III.1 and III.2, the compounds included in the model are CO, H<sub>2</sub>, H<sub>2</sub>O, straight-chained paraffins and linear  $\alpha$ -olefins with chain lengths varying from one (two in the case of olefins) to  $n$  carbon atoms. The maximal carbon chain length is set to 45 to take a sufficiently wide range of products. However, it appears that all 1-alkenes from 1 to 45 carbon atoms are not available in the databases proposed in Aspen Properties®. Consequently, C<sub>25</sub>H<sub>50</sub>, C<sub>31</sub>H<sub>62</sub> to C<sub>35</sub>H<sub>70</sub>, C<sub>37</sub>H<sub>74</sub> to C<sub>39</sub>H<sub>78</sub> and C<sub>41</sub>H<sub>82</sub> to C<sub>45</sub>H<sub>90</sub> are not included in the model. This approximation can be justified due to a smaller olefins production than paraffins and the insignificant fraction these long carbon chains represent in the product spectrum. Thus, not considering these compounds has presumably a negligible impact on the real product formation. The thermodynamic properties of the medium are estimated using the Peng-Robinson equation of state, as it is generally the case for such modelling studies (Knutsen, 2013; Meurer and Kern, 2021).

The Fischer-Tropsch synthesis is a reaction taking place in the gaseous phase. However, given the relatively high molar mass of certain products and the conditions of a low-temperature Fischer-Tropsch synthesis, a liquid phase may appear in the reactor. The appearance of a liquid phase impacts the subsequent steps of the Fischer-Tropsch process, i.e. the separation steps, but this point is beyond the scope of this work. The liquid phase also influences the calculation of some properties, such as density and viscosity. In that case, it is necessary to solve a liquid-vapour equilibrium to know the liquid and vapour fractions, as well as the composition of each phase. Solving this equilibrium inevitably increases the complexity of the model and its implementation. Thus, it motivates to consider only the vapour phase in the reactor. The validity of this hypothesis is verified by demonstrating that the liquid fraction is negligible compared to the vapour fraction at the reactor outlet. To do that, Aspen Plus® can be used to calculate the liquid-vapour equilibrium of a stream having the same composition as the Fischer-Tropsch reactor outlet stream.

The results can be seen in Figure III.1 for which the outlet stream composition is shown for an inlet temperature of 210°C, an inlet pressure of 20 bar, an inlet syngas flow rate of 0.1 kmol/h (composed only of CO and H<sub>2</sub>) and with a syngas ratio (H<sub>2</sub> to CO molar flow rates ratio) equal to 2. The overall flow rate at the reactor outlet equals 0.067 kmol/h, and the results correspond to a CO conversion of 50%. This figure shows that the liquid phase is negligible compared to the vapour phase. It is confirmed by calculating their respective molar fractions, equal to 99.6 mol-% for the vapour and 0.4

mol-% for the liquid phase. This predominance of the vapour phase is mainly explained by a significant share of unreacted syngas, as well as a low production of hydrocarbon chains longer than 20 carbon atoms, which are more likely to condense as they are heavier products.

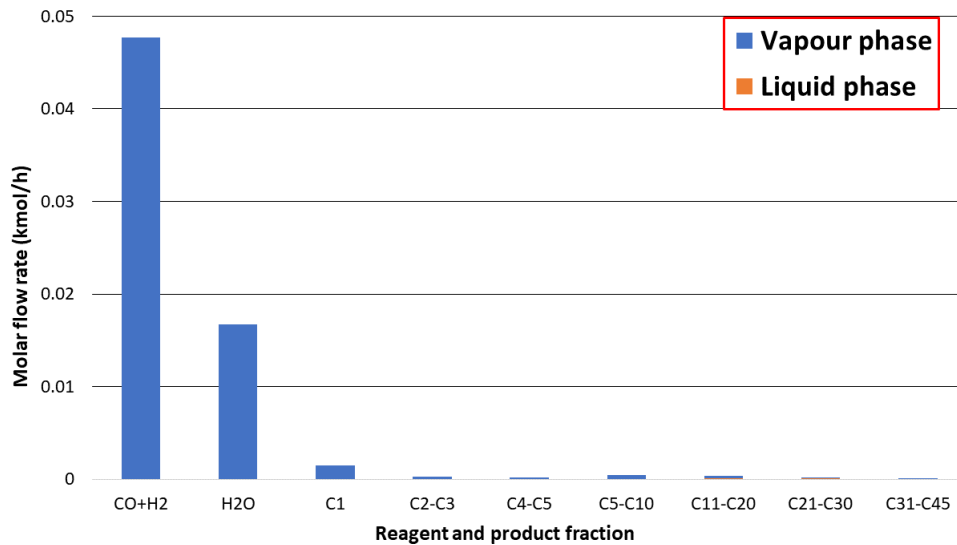


Figure III.1: Molar flow rate distribution at the reactor outlet for reagent and product fractions for the following inlet conditions:  $T = 210^{\circ}\text{C}$ ,  $P = 20$  bar,  $\dot{F} = 0.01$  kmol/h and  $\text{H}_2/\text{CO} = 2$ .

This distribution at the reactor outlet is also used to confirm that neglecting the presence of the compounds that are not available in Aspen Properties® should not massively impact the distribution. Figure III.2 presents the distribution of the Fischer-Tropsch products without the unreacted syngas and the water for the same inlet conditions as in Figure III.1.

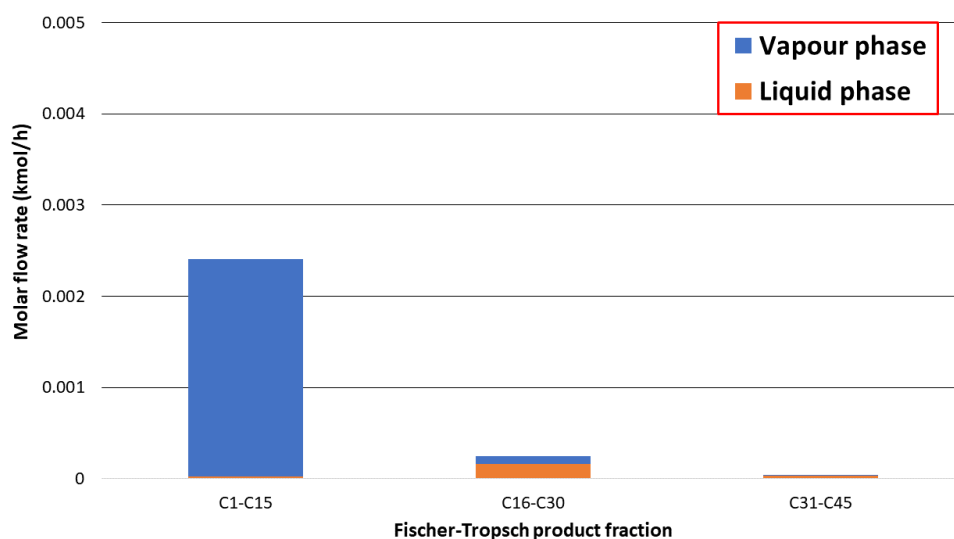


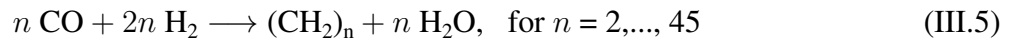
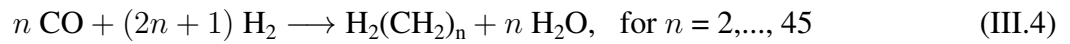
Figure III.2: Molar flow rate distribution at the reactor outlet for the Fischer-Tropsch product fractions for the following inlet conditions:  $T = 210^{\circ}\text{C}$ ,  $P = 20$  bar,  $\dot{F} = 0.01$  kmol/h and  $\text{H}_2/\text{CO} = 2$ .

All the compounds that are not included in the model (except  $\text{C}_{25}\text{H}_{50}$ ) fall in the C31-C45 range and, as Figure III.2 testifies, this fraction only accounts for a negligible part of the Fischer-Tropsch products (less than 2 mol-%). Furthermore, these unavailable compounds are all olefins, and it is shown below

that for a given length chain, paraffins production is larger than for olefins. It means that this absence of olefins is even more negligible, as they are supposed to be produced in smaller quantities than paraffins, which already consist of small amounts, as they fall in the fraction C31-C45.

## III.2 Reaction rates and kinetics

To optimally describe how the stoichiometry of the reactions is derived, it is first necessary to present the reaction rates used in the Fischer-Tropsch reactor model. As it is explained in the next section, the overall methane formation follows a different path than the production of the other Fischer-Tropsch products. Then, the stoichiometric reactions presented at the beginning of the previous section (see Equations III.1 and III.2) can be written as:



Regarding reactions III.4 to III.6, it is not possible to correctly describe the entire Fischer-Tropsch product spectrum with a single reaction rate. Both reaction rates presented below were derived by Ma et al. (2014a,b). The first reaction rate used in the model is called the Fischer-Tropsch reaction rate and is defined as:

$$r'_{FT} = \frac{k_{FT} \cdot p_{\text{CO}}^{a_{FT}} \cdot p_{\text{H}_2}^{b_{FT}}}{\left(1 + q_{FT} \cdot \frac{p_{\text{H}_2\text{O}}}{p_{\text{H}_2}}\right)} \quad (\text{III.7})$$

Here, and for the whole work, the following convention is adopted: a reaction rate  $r'_i$  denotes a reaction rate per unit of catalyst mass, while  $r_i$  denotes a rate per unit of reactor volume. The Fischer-Tropsch reaction rate constant,  $k_{FT}$ , is calculated with:

$$k_{FT} = k_{0,FT} \cdot \exp\left(\frac{E_{a,FT}}{R} \left(\frac{1}{493.15} - \frac{1}{T}\right)\right) \quad (\text{III.8})$$

The meaning, value and units of each variable and parameter appearing in Equations III.7 and III.8 can be found in Table III.1. The reaction rate defined by Equation III.7 corresponds to the CO molar consumption. To be fully precise  $r'_{FT}$  should be referred to as a production rate equals to the CO consumption rate as there is no minus sign in Equation III.7 and as a rate  $r'_i$  corresponds to a production rate by convention. The actual CO consumption thus corresponds to  $-r'_{FT}$ . The reaction rate describing CH<sub>4</sub> formation follows the same general form as the Fischer-Tropsch reaction rate and is thus defined as:

$$r'_{\text{CH}_4} = \frac{k_{\text{CH}_4} \cdot p_{\text{CO}}^{a_{\text{CH}_4}} \cdot p_{\text{H}_2}^{b_{\text{CH}_4}}}{\left(1 + q_{\text{CH}_4} \cdot \frac{p_{\text{H}_2\text{O}}}{p_{\text{H}_2}}\right)} \quad (\text{III.9})$$

where the methane reaction rate constant,  $k_{\text{CH}_4}$ , is calculated with:

$$k_{\text{CH}_4} = k_{0,\text{CH}_4} \cdot \exp\left(\frac{E_{a,\text{CH}_4}}{R} \left(\frac{1}{493.15} - \frac{1}{T}\right)\right) \quad (\text{III.10})$$

The variables and parameters appearing in the definition of the methane reaction rate and its associated rate constant have the same meaning and units as their counterpart for the Fischer-Tropsch reaction rate. Although, the values of the parameters are different, as depicted in Table III.2.

Variable	Meaning	Value	Units
$r'_{FT}$	reaction rate	-	mol/s/g <sub>cat</sub>
$k_{FT}$	reaction rate constant	-	mol/s/g <sub>cat</sub> /MPa <sup><math>a_{FT}+b_{FT}</math></sup>
$p_{CO}$	CO partial pressure	-	MPa
$p_{H_2}$	H <sub>2</sub> partial pressure	-	MPa
$p_{H_2O}$	H <sub>2</sub> O partial pressure	-	MPa
$T$	temperature	-	K
Parameter			
$a_{FT}$	CO reaction order	-0.31	-
$b_{FT}$	H <sub>2</sub> reaction order	0.88	-
$q_{FT}$	water effect constant	-0.24	-
$k_{0,FT}$	reaction rate constant at 493.15 K	$3.694 \times 10^{-6}$	mol/s/g <sub>cat</sub> /MPa <sup><math>a_{FT}+b_{FT}</math></sup>
$E_{a,FT}$	activation energy	104	kJ/mol
$R$	ideal gas constant	8.314	J/mol/K

Table III.1: Meaning, value and units of the variables and parameters used in the Fischer-Tropsch reaction rate definition (see Equations III.7 and III.8)

Parameter	Value	Units
$a_{CH_4}$	-0.86	-
$b_{CH_4}$	1.32	-
$q_{CH_4}$	0.46	-
$k_{0,CH_4}$	$2.925 \times 10^{-7}$	mol/s/g <sub>cat</sub> /MPa <sup><math>a_{CH_4}+b_{CH_4}</math></sup>
$E_{a,CH_4}$	136	kJ/mol

Table III.2: Value and units of the parameters used in the methane reaction rate definition (see Equations III.9 and III.10)

The starting point of these two reaction rates is the following empirical kinetic model:

$$r' = \frac{k \cdot p_{CO}^a \cdot p_{H_2}^b}{\left(1 + q \cdot \frac{p_{H_2O}}{p_{H_2}}\right)} \quad (\text{III.11})$$

for which Ma et al. (2014a,b) experimentally fitted the parameters. They carried out their kinetic experiments in a continuous stirred-tank reactor (CSTR) of 1 L using a 25%Co/Al<sub>2</sub>O<sub>3</sub> catalyst. This empirical expression is interesting as it accounts for the kinetic effect of water on the Fischer-Tropsch and methane reaction through the parameter  $q$ . If it is positive, then the denominator in the reaction rate expression becomes greater than 1, and thus water has a negative kinetic effect on the reaction rate. If this parameter is negative, the denominator becomes smaller than 1, and the kinetic effect is positive. This water effect is discussed below for both reaction rates.

In their study, Ma et al. (2014a) found a negative value for the water effect constant for the Fischer-Tropsch reaction, suggesting that water plays a positive role during Fischer-Tropsch synthesis. It

should be specified that their first conclusion was that water negatively impacts Fischer-Tropsch synthesis (Ma et al., 2011). This inconsistency is explained by the fact that water can adsorb on cobalt sites and lead to reversible oxidation of these sites. The consequence is thus the catalyst deactivation due to a decrease in the number of catalytic sites available for CO adsorption and consequently a decrease in CO conversion. This decrease has repercussions for the value of  $q_{FT}$ , which is determined from CO conversion and which can then deviate from its actual value, leading to a negative water effect. To assess the kinetic water effect on stable cobalt particles, Ma et al. (2014a) carried out their measurements during a period where the deactivation rate was relatively mild and thus the catalyst stable. In that way, the actual kinetic effect of water was assessed without interference from its deactivation effect on the catalyst.

The principal hypothesis explaining the origin of this positive kinetic effect of water on Fischer-Tropsch synthesis was proposed by Bertole et al. (2002). It seems that water increases the concentration of surface-active carbon species in the form of chain growth monomers  $\text{CH}_x$  and induces an acceleration of CO dissociation. Another hypothesis claims that water inhibits the secondary hydrogenation of primary olefins, making them available for insertion and chain growth (Storsæter et al., 2005). This latter hypothesis is less preferred as it only explains an increase in the production rate of Fischer-Tropsch products but not the increase in CO consumption rate, unlike the former hypothesis. Furthermore, the assumption according to which water increases the concentration of chain growth monomers ( $\text{CH}_x$ ) may explain why water has a negative kinetic effect on methane formation, as testified by the positive value of  $q_{\text{CH}_4}$  (see Table III.2). If the amount of surface-active carbon species increases, the chain growth probability increases and the formation of long Fischer-Tropsch products is favoured compared to methane formation. Thus, methane production is lowered in the presence of water (Ma et al., 2014b).

It is also interesting to observe the methane reaction rate orders concerning CO and  $\text{H}_2$  and to compare them with Fischer-Tropsch reaction rate orders. The negative value for the CO rate order (-0.86) suggests that CO inhibits methane formation because of its strong adsorption on cobalt catalysts. But this inhibition is weaker in the case of Fischer-Tropsch synthesis (-0.31), which can be understood by the fact that this strong adsorption enables the formation of longer carbon chains before their desorption. On the other hand, the high positive value for the  $\text{H}_2$  order in the methane reaction rate (1.32) indicates its strong positive impact on  $\text{CH}_4$  formation, as the hydrogenation probability is larger. The smaller value in the Fischer-Tropsch reaction rate (0.88) means that this reaction is less sensitive to  $\text{H}_2$  concentration than methane formation (Ma et al., 2014b).

Another interesting point investigated by Ma et al. (2014a) concerns the mechanism of the Fischer-Tropsch synthesis. They gathered empirical and mechanistic Fischer-Tropsch reaction rate models and the value of their respective parameters. It turns out that the better fit for the experimental kinetic data they obtained occurs with a mechanistic model based on the carbide mechanism, which is described in Section II.3.2.a (Botes et al., 2009). It suggests that the carbide mechanism governs the cobalt-based Fischer-Tropsch synthesis (Ma et al., 2014a).

### III.3 Fischer-Tropsch product distribution

As explained in Section III.1, the Fischer-Tropsch synthesis yields a wide range of hydrocarbon products. In the scope of this model, the products considered are methane, straight-chained paraffins and  $\alpha$ -olefins ranging from 2 to 45 carbon atoms. It is of the highest importance to know how the Fischer-

Tropsch products are distributed among these different chain lengths, as it will impact the process steps downstream of the reactor. Furthermore, the general goal is to design the reactor to maximise the production of the fraction of interest (between C12 and C20 for jet fuel). Then, it is required to determine the specific production of each hydrocarbon of size  $n$ , in other terms, fully describe the product spectrum.

### III.3.1 The Anderson-Schulz-Flory distribution

The Fischer-Tropsch products are assumed to follow the Anderson-Schulz-Flory (ASF) distribution, characterised by a chain growth probability,  $\alpha$ . This chain growth probability is defined as the probability for a growing chain to increase its length by one carbon atom. It can be mathematically translated as the ratio of the chain propagation rate and the sum of this rate with the chain termination rate (Stenger and Askonas, 1986):

$$\alpha = \frac{r_p}{r_p + r_t} \quad (\text{III.12})$$

From this definition, it turns out that the probability that the growing chain desorbs from the catalyst surface equals:

$$1 - \alpha = \frac{r_t}{r_p + r_t} \quad (\text{III.13})$$

The mathematical form of the product distribution can be derived from this theory. The reasoning starts with a growing chain containing a single carbon atom. The probability that another carbon atom is added to the chain equals  $\alpha$  and the probability that this chain desorbs is  $1 - \alpha$ . It turns out that methane formation probability equals  $1 - \alpha$ , i.e. the chain does not grow and immediately desorbs. Following this reasoning, ethane formation probability equals  $\alpha \cdot (1 - \alpha)$ , as it equals the probability for the chain to grow by one element ( $\alpha$ ) before desorption ( $1 - \alpha$ ). Extending the reasoning to  $n$  carbon atoms, the probability for compound  $C_n$  (products containing  $n$  carbon atoms) formation is calculated as:

$$m_n = \alpha^{n-1} \cdot (1 - \alpha) \quad (\text{III.14})$$

A schematic representation of the development of this equation is proposed in Figure III.3.

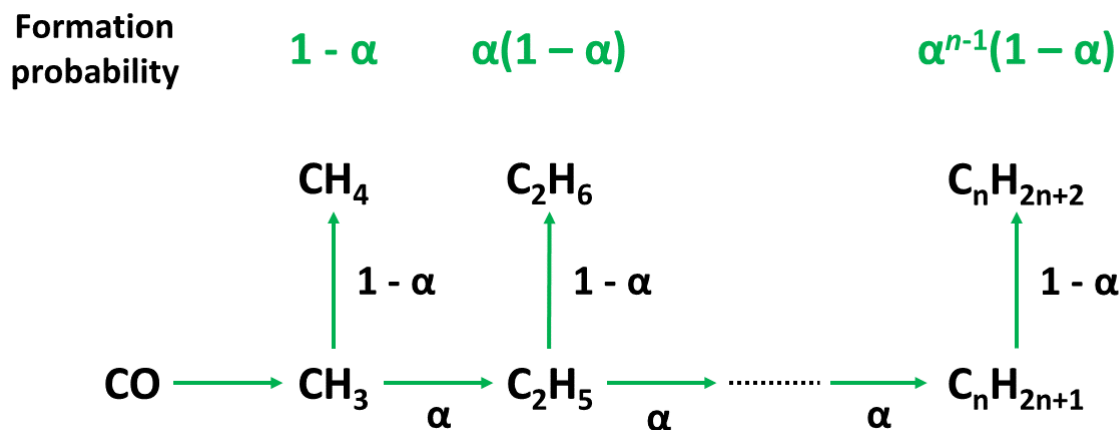


Figure III.3: Schematic representation of chain growth probability (inspired by Panahi et al. (2012))

This probability  $m_n$  corresponds to the molar fraction of product  $C_n$  in the product spectrum. The Fischer-Tropsch synthesis yields a product spectrum in which the chain length varies from one to

an infinite number of carbon atoms, meaning that the molar fraction of a product of length  $n$  in this spectrum effectively equals its formation probability. According to this affirmation, the sum of all molar fractions should be equal to 1, which is verified:

$$\sum_{i=1}^{\infty} m_i = \sum_{i=1}^{\infty} \alpha^{i-1} \cdot (1 - \alpha) = (1 - \alpha) \cdot \sum_{i=1}^{\infty} \alpha^{i-1} = (1 - \alpha) \cdot \frac{1}{1 - \alpha} = 1 \quad (\text{III.15})$$

where the second to last equation is respected if the absolute value of  $\alpha$  is lower than 1, which is fulfilled as it represents a probability (Delhez, 2017).

It is possible to derive an equation describing the mass fraction distribution of Fischer-Tropsch products, which is similar to Equation III.14. It can be shown that:

$$w_n = \frac{m_n \cdot MM_n}{\sum_{i=1}^{\infty} m_i \cdot MM_i} \quad (\text{III.16})$$

where  $w_n$  is the mass fraction of product  $C_n$  in the product spectrum and where  $MM_n$  is its molar mass. The validity of this equation is demonstrated below:

$$\frac{m_n \cdot MM_n}{\sum_{i=1}^{\infty} m_i \cdot MM_i} = \frac{\frac{\dot{F}_n}{\dot{F}} \cdot MM_n}{\sum_{i=1}^{\infty} \frac{\dot{F}_i}{\dot{F}} \cdot MM_i} = \frac{\frac{\dot{m}_n}{\dot{F}}}{\frac{1}{\dot{F}} \sum_{i=1}^{\infty} \dot{m}_i} = \frac{\dot{m}_n}{\sum_{i=1}^{\infty} \dot{m}_i} = \frac{\dot{m}_n}{\dot{m}} = w_n \quad (\text{III.17})$$

in which  $\dot{F}_n$  and  $\dot{F}$  represent the molar flow rate of compound  $C_n$  and the molar flow rate of the overall product spectrum, respectively, and equivalently  $\dot{m}_n$  and  $\dot{m}$  have the same meaning but for the mass flow rate. The molar mass of a Fischer-Tropsch product can be assumed to be directly proportional to the number of carbon atoms constituting its chain (in reality the relation is not directly proportional but the error can be neglected (Flory, 1936)), which is translated as:

$$MM_n = cst \cdot n \quad (\text{III.18})$$

where  $cst$  is an undefined constant. Inserting this equation in Equation III.16 and factoring  $cst$  out of the sum, it turns out that this constant cancels out, leading to:

$$w_n = \frac{m_n \cdot n}{\sum_{i=1}^{\infty} m_i \cdot i} \quad (\text{III.19})$$

Using Equation III.14, it leads to:

$$w_n = \frac{\alpha^{n-1} \cdot (1 - \alpha) \cdot n}{\sum_{i=1}^{\infty} \alpha^{i-1} \cdot (1 - \alpha) \cdot i} = \frac{\alpha^{n-1} \cdot n}{\sum_{i=1}^{\infty} \alpha^{i-1} \cdot i} = \frac{\alpha^{n-1} \cdot n}{\frac{1}{(1-\alpha)^2}} \quad (\text{III.20})$$

where the last equality is respected if the absolute value of  $\alpha$  is smaller than 1 (Delhez, 2017), which is still fulfilled. The mass fraction distribution can thus be calculated using:

$$w_n = n \cdot \alpha^{n-1} \cdot (1 - \alpha)^2 \quad (\text{III.21})$$

An interesting feature of the two derived distributions (Equations III.14 and III.21) is that there exists a linear relationship between the molar fraction of a product and its number of carbon atoms in a logarithmic plot:

$$\ln m_n = \ln (\alpha^{n-1} \cdot (1 - \alpha)) = (n - 1) \cdot \ln \alpha + \ln (1 - \alpha) = n \cdot \ln \alpha + \ln \left( \frac{1 - \alpha}{\alpha} \right) \quad (\text{III.22})$$

This linear relationship is easily verified by calculating the molar fraction of products ranging from 1 to 50 carbon atoms and constructing the associated graph, as shown in Figure III.4 for a chain growth probability of 0.9. Looking at the straight-line equation depicted in this figure, it is verified that the distribution follows Equation III.22. The same kind of relation can be obtained for the mass fractions starting from Equation III.21 and plotting  $\ln (w_n/n)$  instead.



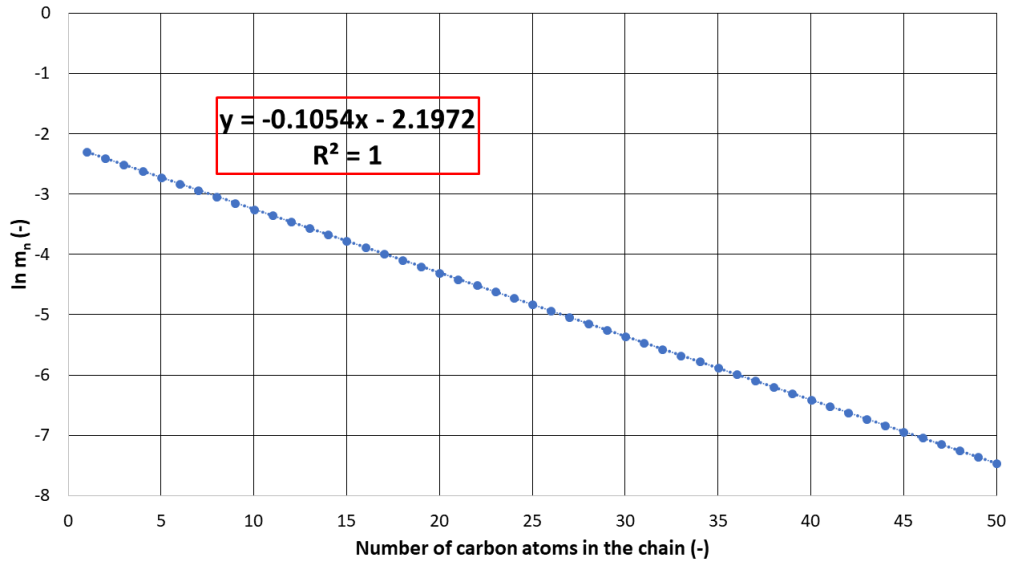


Figure III.4: Molar fraction ASF distribution for a chain growth probability  $\alpha = 0.9$

### III.3.2 Differentiation between paraffins and olefins production

In the description of the ASF distribution, no differentiation is made between the production of olefins and paraffins. As described in the preceding section, the distribution only enables knowing the fractions (molar or mass) of the products having a given number of carbon atoms in their chain. It means that the calculated fraction  $m_n$ , for instance, includes the molar fraction of paraffins of size  $n$  and the molar fraction of olefins of size  $n$  which are produced. The following equation is thus written:

$$m_n = m_{n,p} + m_{n,o} \quad (\text{III.23})$$

where  $m_{n,p}$  (resp.  $m_{n,o}$ ) corresponds to the molar fraction of paraffins (resp. olefins) of size  $n$  produced. A solution proposed to calculate these two molar fractions is to use the ASF distribution as described in the previous point (see Equation III.14) for both the paraffins and the olefins, but with a different chain growth probability  $\alpha$  for the two compound classes. This solution is explained by the fact that the catalyst would include two different types of active sites leading to two different propagation probabilities (Hillestad, 2015). However, in this work, only one chain growth probability is considered. Paraffin and olefin molar fractions should thus be determined alternatively. To determine how the molar fraction of products of size  $n$  is distributed among paraffins and olefins, the following equation is used (Iglesia et al., 1993):

$$\frac{m_{n,o}}{m_{n,p}} = e^{-0.3} \quad (\text{III.24})$$

This relation confirms that paraffins are more abundant than olefins for a given chain length, as mentioned in Section III.1. Normally, the argument of the exponent function should vary with the chain length, inducing a chain length-dependent olefins-to-paraffins ratio. However, an average value equal to -0.3 can be used, as is the case in different other works (Panahi et al., 2012; Meurer and Kern, 2021). Then, if  $m_n$  can be calculated using the ASF distribution (see Equation III.14), then the molar fractions  $m_{n,p}$  and  $m_{n,o}$  can be determined using Equations III.23 and III.24, and leading to:

$$m_{n,p} = m_n - m_{n,o} = m_n - e^{-0.3} \cdot m_{n,p} \Leftrightarrow m_{n,p} = \frac{m_n}{1 + e^{-0.3}} \quad (\text{III.25})$$

$$m_{n,o} = m_n - m_{n,p} = m_n - \frac{m_n}{1 + e^{-0.3}} \Leftrightarrow m_{n,o} = \frac{e^{-0.3} \cdot m_n}{1 + e^{-0.3}} \quad (\text{III.26})$$



In reality, this olefins-to-paraffins ratio estimation is much more complicated than it seems and is the centre of various discussions in the literature. Most papers agree with the fact that the ratio exponentially decreases with the chain length, except for ethene, which is highly reactive towards  $H_2$  and thus leads to a lower olefins-to-paraffins ratio for products containing two carbon atoms (Laan and Beenackers, 1999; Pour and Housaindokht, 2013; Todić et al., 2017). The reason for this exponential decrease is that the residence time of olefins increases with chain length making them available for secondary reactions and thus decreasing olefins yield (Rytter et al., 2020). Iglesia et al. (1993) explain this phenomenon by an exponential decrease in the olefins diffusivity coefficient with their size, but they did not manage to verify their empirical model with experimental data. On the other hand, Pour and Housaindokht (2013) explain the phenomenon by a solubility variation, i.e. a variation in the liquid-vapour equilibrium, impacting the olefins diffusion and thus modifying the extent of secondary reactions.

### III.3.3 Calculation of chain growth probability

The model used in this study to determine the value of the chain growth probability ( $\alpha$ ) mainly depends on the syngas ratio ( $H_2$  to CO molar flow rates) and the temperature, meaning that this probability is likely to change along the reactor. There are other models in the literature considering, for instance, two different chain growth probabilities for specific chain lengths (Huff and Satterfield, 1984) or even more complex models including olefins readsorption through more detailed kinetics (Visconti et al., 2011). The model used in this work was derived by Vervloet et al. (2012) from the chain growth probability definition (see Equation III.12) and by assuming that the propagation and termination rate constants follow a standard Arrhenius dependency with temperature. It is presented as follows:

$$\alpha = \frac{1}{1 + k_a \cdot \left(\frac{C_{H_2}}{C_{CO}}\right)^\beta \cdot \exp\left(\frac{\Delta E_\alpha}{R} \left(\frac{1}{493.15} - \frac{1}{T}\right)\right)} \quad (\text{III.27})$$

The meaning, value and units of the variables and parameters appearing in this equation can be found in Table III.3.

Variable	Definition	Value	Units
$\alpha$	chain growth probability	-	-
$C_{H_2}$	$H_2$ molar concentration	-	mol/L
$C_{CO}$	CO molar concentration	-	mol/L
$T$	temperature	-	K
<b>Parameter</b>			
$k_a$	termination and propagation rate constants ratio	0.0567	-
$\beta$	syngas ratio power constant	1.76	-
$\Delta E_\alpha$	difference in activation energies between termination and propagation reactions	120.4	kJ/mol
$R$	ideal gas constant	8.314	J/mol/K

Table III.3: Meaning, value and units of the variables and parameters used for chain growth probability calculation (see Equation III.27)

### III.3.4 Non-ideal Anderson-Schulz-Flory distribution

The ASF distribution described in Section III.3.1 is generally referred to as the ideal ASF distribution, as all points in Figure III.4 fall on a perfectly straight line. However, if an experimental product distribution is plotted, some deviations may appear, leading to not perfectly aligned points. These deviations are sufficiently large to be differentiated from experimental errors. A schematic view of an experimental distribution is depicted in Figure III.5, as an example (Todic et al., 2017). It turns out from this figure that an experimental Fischer-Tropsch distribution differs from an ideal ASF distribution in three principal deviations.

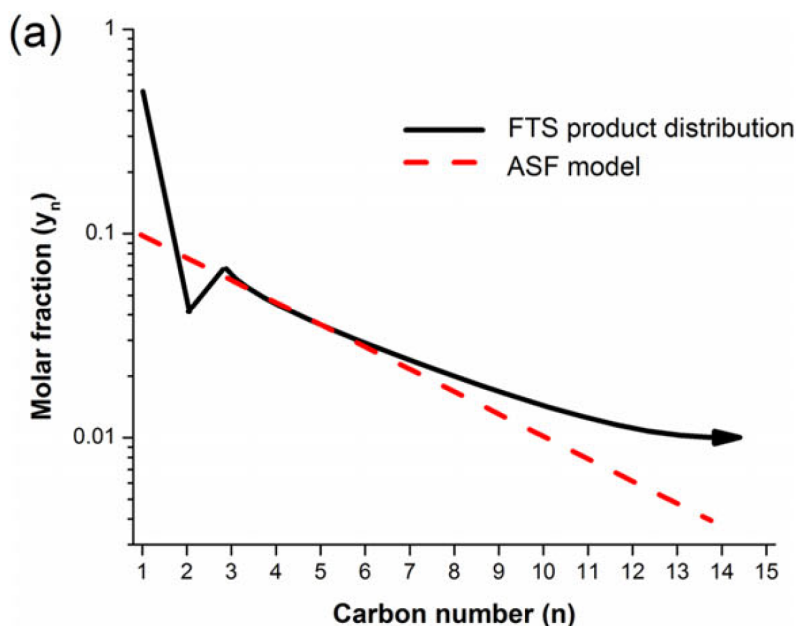


Figure III.5: Schematic representation of an experimental Fischer-Tropsch product distribution compared with an ideal ASF distribution (Todic et al., 2017)

The first one consists in a higher observed selectivity for methane than its predicted counterpart. Ma et al. (2014b) showed that this high CH<sub>4</sub> selectivity is induced by a higher rate constant for methane compared to the rate constant of heavier products. Visconti et al. (2011) went further by showing that this higher rate constant comes from a higher pre-exponential factor for methane desorption than for other products, while their respective activation energies seem to be comparable. However, several authors claim that the reason is more complex and is linked to different reaction pathways for methane formation, including its production through the classical Fischer-Tropsch polymerisation and an additional methanation reaction, implying the existence of two different catalytic active sites (Yang et al., 2013; Ma et al., 2014b; Todici et al., 2017).

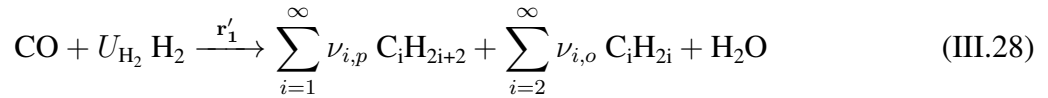
The second deviation consists in a lower than expected production of C<sub>2</sub> species which is generally attributed to the higher reactivity of ethene that readsorbs on the catalyst to form longer chains. The last observed deviation is a higher selectivity of heavier hydrocarbons compared to the ideal ASF distribution. There are different explanations proposed for this deviation, including the presence of different types of catalytic sites leading to different chain growth probabilities. The readsorption of  $\alpha$ -olefins leading to secondary reactions because of chain-length-dependent solubility and diffusion coefficients is also a proposed explanation (Förtsch et al., 2015).

In the scope of this work, only the methane deviation is accounted for, as it generally represents the higher observed deviation. Furthermore, methane is the less desirable product of the Fischer-Tropsch product spectrum. Thus, it is relevant to accurately determine the actual methane production (Todic et al., 2017). It is described in the next section how this methane deviation is included in the reactor model. A more detailed kinetics model should be used to account for the other deviations, namely a micro-kinetics description with readsorption reaction rates (Förtsch et al., 2015).

### III.4 Stoichiometry

In the previous section, the theoretical background concerning the Fischer-Tropsch products is presented. Here, it is described how these theoretical aspects are included in the reactor model by determining the stoichiometry of the reactions. The stoichiometric coefficients associated with each product dictate their final distribution. As it is shown below, they also enable the determination of the stoichiometric coefficient of  $H_2$ .

The starting point for the derivation of this stoichiometry is to take back the stoichiometric reactions given in Section III.2 and write them down in such a way that the stoichiometric coefficients are apparent:



where  $\nu_{i,p}$  (resp.  $\nu_{i,o}$ ) describes the stoichiometric coefficient associated to the paraffin (resp. olefin)  $C_i$  and  $U_{H_2}$  the one associated to  $H_2$  consumption, which is called hydrogen usage ratio. Reaction III.28 denotes the synthesis of paraffins and olefins as a single reaction with the reaction rate  $r'_1$ , while the second reaction shows an additional methane formation (as it is already produced by the first reaction) with the reaction rate  $r'_2$ . The reactions are portrayed such that the first reaction represents the Fischer-Tropsch synthesis in which all products, including methane, follow an ideal ASF distribution. However, as mentioned previously, it is desired to consider the methane deviation in the model, therefore, the second reaction is taken into consideration. Thus, the methane produced by the second reaction is the difference between the observed methane production and the one that would be observed if it followed an ideal ASF distribution.

Ma et al. (2014b) mention in their article that  $-r'_{FT}$  (see Equation III.7) describes CO consumption. It means that  $-r'_{FT}$  corresponds to the CO consumption rate whether it comes from Reaction III.28 or III.29, inducing the following equality:

$$r'_{FT} = r'_1 + r'_2 \quad (III.30)$$

On the other hand, they state that  $r'_{CH_4}$  corresponds to the methane rate, representing the overall production of methane in the reactor, and thus including its formation by both reactions. It leads to the following equation:

$$r'_{CH_4} = \nu_{1,p} \cdot r'_1 + r'_2 \quad (III.31)$$

Solving the system of equations composed of Equations III.30 and III.31, an expression for  $r'_1$  and  $r'_2$ , only in terms of  $r'_{FT}$  and  $r'_{CH_4}$ , is achieved:

$$r'_1 = \frac{r'_{FT} - r'_{CH_4}}{1 - \nu_{1,p}} \quad (III.32)$$

$$r'_2 = \frac{r'_{\text{CH}_4} - \nu_{1,p} \cdot r'_{FT}}{1 - \nu_{1,p}} \quad (\text{III.33})$$

Then, the net reaction rates for each compound appearing in the two reactions described by Reactions III.28 and III.29 can be determined:

$$r'_{\text{CO}} = -r'_1 - r'_2 = -r'_{FT} \quad (\text{III.34})$$

$$r'_{\text{H}_2} = -U_{\text{H}_2} \cdot r'_1 - 3 \cdot r'_2 = \frac{(3 \cdot \nu_{1,p} - U_{\text{H}_2}) \cdot r'_{FT} - (3 - U_{\text{H}_2}) \cdot r'_{\text{CH}_4}}{1 - \nu_{1,p}} \quad (\text{III.35})$$

$$r'_{\text{H}_2\text{O}} = r'_1 + r'_2 = r'_{FT} \quad (\text{III.36})$$

$$r'_{\text{CH}_4} = \nu_{1,p} \cdot r'_1 + r'_2 = r'_{\text{CH}_4} \quad (\text{III.37})$$

$$r'_{i,p} = \nu_{i,p} \cdot r'_1 = \nu_{i,p} \cdot \frac{r'_{FT} - r'_{\text{CH}_4}}{1 - \nu_{1,p}} \quad \text{for } i = 2, \dots, 45 \quad (\text{III.38})$$

$$r'_{i,o} = \nu_{i,o} \cdot r'_1 = \nu_{i,o} \cdot \frac{r'_{FT} - r'_{\text{CH}_4}}{1 - \nu_{1,p}} \quad \text{for } i = 2, \dots, 45 \quad (\text{III.39})$$

$U_{\text{H}_2}$ ,  $\nu_{i,p}$  and  $\nu_{i,o}$  are unknowns needed to be calculated, thereby the stoichiometry is fully specified.

### III.4.1 Determination of Fischer-Tropsch product stoichiometric coefficients

To calculate the stoichiometric coefficients of Fischer-Tropsch products,  $\nu_{i,p}$  and  $\nu_{i,o}$ , a mass balance on carbon atoms in Reaction III.28 is conducted and further developed:

$$1 = \sum_{i=1}^{\infty} i \cdot \nu_{i,p} + \sum_{i=2}^{\infty} i \cdot \nu_{i,o} \quad (\text{III.40})$$

$$\Leftrightarrow 1 = 1 \cdot \nu_{1,p} + \sum_{i=2}^{\infty} i \cdot \nu_{i,p} + \sum_{i=2}^{\infty} i \cdot \nu_{i,o} \quad (\text{III.41})$$

$$\Leftrightarrow 1 = \nu_{1,p} + \sum_{i=2}^{\infty} (i \cdot \nu_{i,p} + i \cdot \nu_{i,o}) \quad (\text{III.42})$$

The theoretical stoichiometric coefficient  $\nu_i$  is introduced, which can be defined as:

$$\nu_i = \nu_{i,p} + \nu_{i,o} \quad (\text{III.43})$$

meaning that  $\nu_1 = \nu_{1,p}$ , as there is no olefin containing only one carbon atom (i.e.  $\nu_{1,o} = 0$ ). Subsequently:

$$\Leftrightarrow 1 = \nu_1 + \sum_{i=2}^{\infty} i \cdot \nu_i \quad (\text{III.44})$$

$$\Leftrightarrow 1 = 1 \cdot \nu_1 + \sum_{i=2}^{\infty} i \cdot \nu_i \quad (\text{III.45})$$

$$\Leftrightarrow 1 = \sum_{i=1}^{\infty} i \cdot \nu_i \quad (\text{III.46})$$

As stated previously, the Fischer-Tropsch products yielded by this reaction are assumed to follow an ideal ASF distribution, meaning that their respective mass fractions are calculated with Equation III.21. Then, using this equation and the additive property of mass fractions, it turns out that:

$$\sum_{i=1}^{\infty} w_i = \sum_{i=1}^{\infty} i \cdot \alpha^{i-1} \cdot (1 - \alpha)^2 = 1 \quad (\text{III.47})$$

Comparing this last equality with Equation III.46, the following relation is deduced:

$$\nu_i = \alpha^{i-1} \cdot (1 - \alpha)^2 \quad (\text{III.48})$$

Hillestad (2015) obtained the same general form for these stoichiometric coefficients. However, this equation only enables the calculation of the stoichiometric coefficients of  $C_i$  species without differentiating the stoichiometric coefficient for the paraffins and the one for the olefins. It is noticeable in Section III.3.2 that the paraffin and olefin molar fractions for a given chain length are linked through Equation III.24. To effectively observe this ratio in the product spectrum, the stoichiometric coefficients should respect this ratio as well, leading to:

$$\frac{\nu_{i,o}}{\nu_{i,p}} = e^{-0.3} \quad (\text{III.49})$$

and following the same reasoning that leads to Equation III.25 and III.26 for paraffin and olefin molar fractions, the following equations are obtained:

$$\nu_{i,p} = \frac{\nu_i}{1 + e^{-0.3}} = \frac{\alpha^{i-1} \cdot (1 - \alpha)^2}{1 + e^{-0.3}} \quad (\text{III.50})$$

$$\nu_{i,o} = \frac{e^{-0.3} \cdot \nu_i}{1 + e^{-0.3}} = \frac{e^{-0.3} \cdot \alpha^{i-1} \cdot (1 - \alpha)^2}{1 + e^{-0.3}} \quad (\text{III.51})$$

### III.4.2 Determination of hydrogen usage ratio

The hydrogen usage ratio is defined as the ratio between the amount of  $H_2$  and the amount of CO converted in Reaction III.28. It is determined by performing a mass balance on the hydrogen atoms in Reaction III.28:

$$2 U_{H_2} = \sum_{i=1}^{\infty} \nu_{i,p} \cdot (2i + 2) + \sum_{i=2}^{\infty} \nu_{i,o} \cdot 2i + 2 \quad (\text{III.52})$$

$$\Leftrightarrow 2 U_{H_2} = 2 \sum_{i=1}^{\infty} \nu_{i,p} \cdot (i + 1) + 2 \sum_{i=2}^{\infty} \nu_{i,o} \cdot i + 2 \quad (\text{III.53})$$

$$\Leftrightarrow U_{H_2} = \sum_{i=1}^{\infty} \nu_{i,p} \cdot (i + 1) + \sum_{i=2}^{\infty} \nu_{i,o} \cdot i + 1 \quad (\text{III.54})$$

$$\Leftrightarrow U_{H_2} = \sum_{i=1}^{\infty} \nu_{i,p} \cdot i + \sum_{i=1}^{\infty} \nu_{i,p} + \sum_{i=2}^{\infty} \nu_{i,o} \cdot i + 1 \quad (\text{III.55})$$

$$\Leftrightarrow U_{H_2} = 1 \cdot \nu_{1,p} + \sum_{i=2}^{\infty} \nu_{i,p} \cdot i + \sum_{i=2}^{\infty} \nu_{i,o} \cdot i + \sum_{i=1}^{\infty} \nu_{i,p} + 1 \quad (\text{III.56})$$

$$\Leftrightarrow U_{H_2} = \nu_1 + \sum_{i=2}^{\infty} (\nu_{i,p} + \nu_{i,o}) \cdot i + \sum_{i=1}^{\infty} \nu_{i,p} + 1 \quad (\text{III.57})$$

$$\xLeftrightarrow{(\text{III.43}),(\text{III.50})} U_{H_2} = \sum_{i=1}^{\infty} \nu_i \cdot i + \sum_{i=1}^{\infty} \frac{\nu_i}{1 + e^{-0.3}} + 1 \quad (\text{III.58})$$

$$\xLeftrightarrow{(\text{III.46}),(\text{III.48})} U_{H_2} = 2 + \frac{1}{1 + e^{-0.3}} \cdot \sum_{i=1}^{\infty} \alpha^{i-1} \cdot (1 - \alpha)^2 \quad (\text{III.59})$$

where the two last equivalences hold from the mass balance on carbon atoms. The sum appearing in Equation III.59 is transformed by taking advantage of the following property:

$$\sum_{i=1}^{\infty} m_i = 1 \xLeftrightarrow{(\text{III.14})} \sum_{i=1}^{\infty} \alpha^{i-1} \cdot (1 - \alpha) = 1 \Leftrightarrow \sum_{i=1}^{\infty} \alpha^{i-1} = \frac{1}{1 - \alpha} \quad (\text{III.60})$$

Thus, the hydrogen usage ratio is finally determined with the following equation:

$$U_{H_2} = 2 + \frac{1 - \alpha}{1 + e^{-0.3}} \quad (\text{III.61})$$

It is noticeable that the chain growth probability appearing in this expression decreases the  $H_2$  usage ratio. If the chain growth probability increases, longer hydrocarbon chains are produced as they are less likely to be terminated. As the termination step often involves the reaction with  $H_2$ , the amount of  $H_2$  consumed relative to the amount of CO consumed decreases.

## III.5 Implementation of balances

In the scope of this work, three balances are considered. The material balance describes the evolution of compound flow rates along the reactor. The energy balance describes the temperature evolution, a critical feature in the Fischer-Tropsch synthesis. Finally, the momentum balance assesses the potential pressure drop along the reactor.

As already mentioned previously, temperature control is paramount for highly exothermic reactions like FT synthesis. Generally, it leads to the utilisation of multi-tubular fixed-bed reactors at industrial scale (Guettel et al., 2008). On the other hand, lab-scale experiments are sometimes performed in single-tube reactors (Ermolaev et al., 2015), as will be the case at ULiège, as explained by Morales and Léonard (2022). In this perspective, and to be consistent with the previous work of Morales and Léonard (2022), the reactor is modelled as a single-tube plug-flow reactor with heterogeneous catalysis. Besides, this is relevant for the comparison of this model with Morales and Léonard (2022)'s one. The temperature control is carried out by a cooling jacket in which a coolant (pressurised water in the first instance) flows in a counter-current mode at a considerable flow rate. It ensures to keep the coolant temperature as constant as possible.

### III.5.1 Material balance

The material balance must be applied to each compound found or likely to be found within the reactor. A schematic view of a plug-flow reactor is represented in Figure III.6, serving as a basis for

the material balance derivation. The fundamental assumption associated with this kind of reactor is the plug-flow assumption, according to which the flow field may be modelled as a plug-flow profile. Then, no radial variations in velocity, concentration, temperature or reaction rate are considered, but only axial variations (Fogler, 2016).

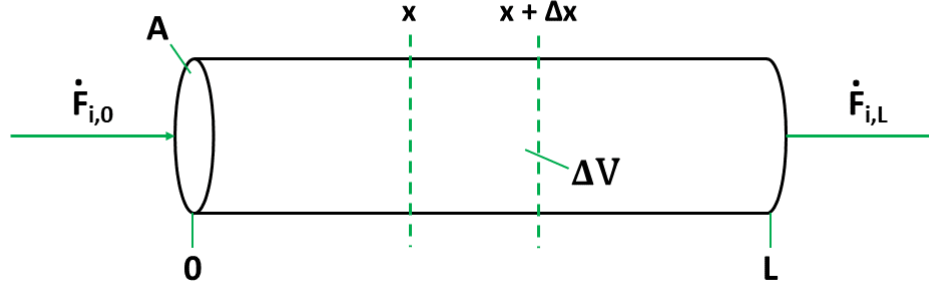


Figure III.6: Schematic representation of a plug-flow reactor of length  $L$ , cross-sectional area  $A$ , inlet and outlet molar flow rates for component  $i$   $\dot{F}_{i,0}$  and  $\dot{F}_{i,L}$ , respectively. An infinitesimal volume  $\Delta V$  is also represented

With that in mind, the material balance is derived on the infinitesimal volume  $\Delta V$ :

$$\frac{dN_i}{dt} = \dot{F}_i(x) - \dot{F}_i(x + \Delta x) + \int^{\Delta V} r_i dV \quad (\text{III.62})$$

where  $N_i$  corresponds to the number of moles of compound  $i$ ,  $\dot{F}_i$  to its molar flow rate and  $r_i$  to its production rate. The objective pursued in this work is to understand the reactor behaviour at steady-state, meaning that the time derivative cancels out. By combining the plug-flow hypothesis and the fact that the volume considered is infinitesimal, it is assumed that the reaction rate is constant in the volume. The cross-sectional area,  $A$ , is assumed to be constant along the reactor, leading to:

$$\frac{\dot{F}_i(x + \Delta x) - \dot{F}_i(x)}{\Delta x} = A \cdot r_i \quad (\text{III.63})$$

$\Delta x$  being an infinitesimal length element, the left-hand side of this equation is equivalent to a derivative with respect to the  $x$  coordinate, i.e. the axial coordinate, leading to:

$$\frac{d\dot{F}_i}{dx} = A \cdot r_i \quad (\text{III.64})$$

In this equation, the reaction rate units are implicitly  $\text{mol/s/m}^3_{\text{reactor}}$  for the homogeneity to be respected. However, as portrayed in Tables III.1 and III.2, the reaction rates used in this reactor model are expressed in  $\text{mol/s/g}_{\text{cat}}$ . The material balance should be slightly modified to be used with the reaction rates presented in these tables. It is denoted by  $r'_i$  in the next equation to differentiate it from the reaction rate in  $\text{mol/s/m}^3_{\text{reactor}}$ . It is done by multiplying the right-hand side of the balance by the catalyst bulk density  $\rho_b$  expressed in  $\text{g}_{\text{cat}}/\text{m}^3_{\text{reactor}}$ :

$$\frac{d\dot{F}_i}{dx} = A \cdot r'_i \cdot \rho_b = A \cdot r'_i \cdot \rho_c \cdot (1 - \phi) \quad (\text{III.65})$$



where  $\rho_c$  is the catalyst density and  $\phi$  the catalytic bed porosity. Alternatively, the derivation variable  $x$  can be replaced by another variable, which is the mass of catalyst used,  $W$ :

$$\frac{d\dot{F}_i}{dW} = r'_i \quad (\text{III.66})$$

for which the homogeneity is easily verified. From these two different formulations, the ratio between the required mass of catalyst,  $W$ , and the required reactor volume,  $V$ , emerges, which enables to pass from one to the other:

$$\frac{W}{V} = \rho_c \cdot (1 - \phi) \Leftrightarrow \frac{W}{L} = \rho_c \cdot (1 - \phi) \cdot A \quad (\text{III.67})$$

If both sides of the equation are multiplied by the cross-sectional area,  $A$ , the mass of catalyst used per unit length of the reactor emerges. The values for the catalytic bed characteristics are given in Table III.4, which come from the article of [Panahi et al. \(2012\)](#) and are also used by [Morales and Léonard \(2022\)](#). The catalyst characteristics are similar to the one used by [Morales and Léonard \(2022\)](#) to be consistent in the comparison of the two kinetic models. However, as there are some uncertainties on these values, it could be interesting to see the impact of their modification on the reactor behaviour. For instance, the catalytic bed volume fraction is small in this case, meaning that the influence of the catalyst on the total pressure should be relatively small. It could thus be of interest to see the effect of an increase of this volume fraction on the pressure drop and the heat released per unit length.

Characteristic	Meaning	Value	Units
$\rho_c$	catalyst density	2000	$\text{kg}_{\text{cat}}/\text{m}_{\text{cat}}^3$
$1 - \phi$	catalytic bed volume fraction	0.1	$\text{m}_{\text{cat}}^3/\text{m}_{\text{reactor}}^3$
$\rho_b$	catalytic bed bulk density	200	$\text{kg}_{\text{cat}}/\text{m}_{\text{reactor}}^3$

Table III.4: Meaning, value and units of the catalytic bed characteristics

### III.5.2 Energy balance

The Fischer-Tropsch synthesis is a highly exothermic reaction, which can induce large temperature rises if efficient temperature control is not set up. As explained earlier, the low-temperature cobalt-based Fischer-Tropsch synthesis must be operated in a limited temperature range to ensure an optimal efficiency. In other terms, the temperature should be kept as constant as possible, which is done with a counter-current cooling system as schematically represented in Figure III.7. The reaction medium flows in the central part, while the cooling medium is in the annulus section.

To determine the evolution of the reactor temperature along its length, the energy balance on the infinitesimal volume  $\Delta V$  is derived at steady-state:

$$\left(\sum_i \dot{F}_i \cdot h_i\right)(x) - \left(\sum_i \dot{F}_i \cdot h_i\right)(x + \Delta x) - \Delta\dot{Q} = 0 \quad (\text{III.68})$$

where the sum covers all components present in the reactor.  $\dot{F}_i$  is the molar flow rate of compound  $i$  and  $h_i$  its molar enthalpy. The heat exchange rate between the reactor and the cooling medium,  $\Delta\dot{Q}$ , is calculated as:

$$\Delta\dot{Q} = U \cdot \Delta A' \cdot (T - T_c) = U \cdot \pi \cdot D \cdot \Delta x \cdot (T - T_c) \quad (\text{III.69})$$

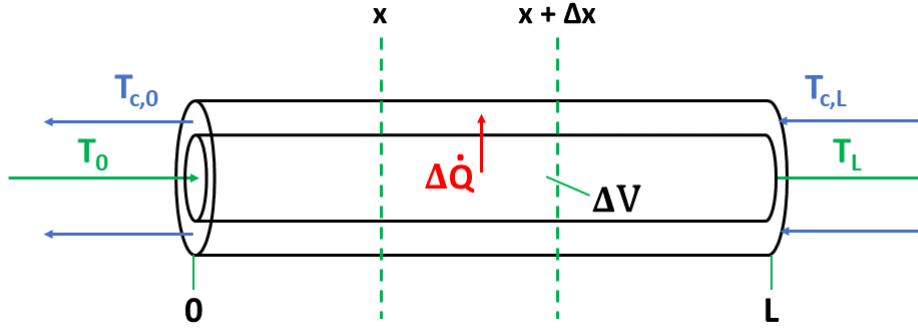


Figure III.7: Schematic representation of a plug-flow reactor with its cooling system and their respective inlet and outlet temperatures. An infinitesimal volume  $\Delta V$  in which the heat exchange rate  $\Delta \dot{Q}$  is also represented

where  $U$  is the overall heat transfer coefficient ( $\text{W/m}^2/\text{K}$ ),  $A'$  the exchange area between the reactor and the cooling medium ( $\text{m}^2$ ),  $D$  the diameter of the reactor tube (i.e. the internal diameter in m),  $T$  the reactor temperature (K), and  $T_c$  the coolant temperature (K). Incorporating this equation in the energy balance leads to:

$$\left( \sum_i \dot{F}_i \cdot h_i \right)(x) - \left( \sum_i \dot{F}_i \cdot h_i \right)(x + \Delta x) = U \cdot \pi \cdot D \cdot \Delta x \cdot (T - T_c) \quad (\text{III.70})$$

This balance can be further derived (see Appendix A for the complete derivation) to make the temperature derivative with respect to the axial coordinate appear, leading to:

$$\frac{dT}{dx} = \frac{(-\Delta H_{R,1} \cdot r_1 - \Delta H_{R,2} \cdot r_2) \cdot A \cdot \rho_b - U \cdot \pi \cdot D \cdot (T - T_c)}{\dot{F} \cdot C_P} \quad (\text{III.71})$$

where  $\Delta H_{R,i}$  (J/mol) is the heat of reaction  $i$  (the subscripts 1 and 2 refer to the two reactions presented in Section III.4),  $\dot{F}$  the total molar flow rate flowing through the reactor (mol/s) and  $C_P$  the heat capacity of the reaction medium (J/mol/K).

The first term in the numerator describes the energy released by the reactions, which tends to increase the temperature, as it is positive (the heat of reaction of an exothermic reaction being negative). Then, this heat generation term is balanced out by the second term in the numerator, corresponding to the heat exchanged with the cooling medium. From this expression, it turns out that the reactor temperature decreases if the heat removed by the coolant is greater than the heat generated in the reactor. The denominator translates the capacity of the reaction medium to limit the temperature increase by absorbing energy ( $C_P$ ) and by evacuating energy through its flow ( $\dot{F}$ ).

The heat of reactions appearing in Equation III.71 are calculated as the difference between the product enthalpies and the reagent molar enthalpies, which are all weighted with their respective stoichiometric coefficients in the corresponding reaction, the heat of reaction being given per unit mol of reacted CO:

$$\Delta H_{R,k} = \sum_i \nu_{i,k} \cdot h_i \quad (\text{III.72})$$

where the subscript  $k$  refers to the number of the considered reaction and  $i$  to the considered component. Then, the heats of reaction corresponding to Reactions III.28 and III.29 are calculated as:

$$\Delta H_{R,1} = \sum_{\text{paraffins}} \nu_{i,p} \cdot h_{i,p} + \sum_{\text{olefins}} \nu_{i,o} \cdot h_{i,o} + h_{\text{H}_2\text{O}} - h_{\text{CO}} - U \cdot h_{\text{H}_2} \quad (\text{III.73})$$

$$\Delta H_{R,2} = h_{\text{CH}_4} + h_{\text{H}_2\text{O}} - h_{\text{CO}} - 3 \cdot h_{\text{H}_2} \quad (\text{III.74})$$

As noticeable in Equation III.71, the temperature of the cooling medium intervenes. Thus, it is also necessary to predict the evolution of this temperature along the reactor. In this regard, a similar energy balance as the one previously done is derived, but this time the control volume corresponds to the cooling medium leading to:

$$-\dot{F}_c \cdot h_c(x) + \dot{F}_c \cdot h_c(x + \Delta x) + \Delta \dot{Q} = 0 \quad (\text{III.75})$$

The signs for this balance are different from the balance on the reactor. Heat is now transferred towards the inside of the control volume, and the flow direction is opposite. Another difference is that the coolant is assumed to be a pure component (pressurised water in this case), resulting in the absence of sums compared to the balance on the reactor. The same kind of development as for the balance on the reactor (see Appendix A for the complete derivation) is performed to obtain this final expression:

$$\frac{dT_c}{dx} = - \frac{U \cdot \pi \cdot D \cdot (T - T_c)}{\dot{F}_c \cdot C_{P,C}} \quad (\text{III.76})$$

where  $\dot{F}_c$  is the coolant molar flow rate and  $C_{P,C}$  its molar heat capacity. The presence of the minus sign in this equation is the consequence of the counter-current flow, which means that if the coolant flows in the same direction as the reaction medium, the same expression can be applied by removing the minus sign. As already mentioned at the beginning of this section, the coolant flow rate is set up sufficiently high for its temperature to be kept constant, which is understandable regarding Equation III.76: a greater flow rate incurs into a greater denominator, and thus a milder temperature variation.

This work discusses the same experimental reactor as the one described by Morales and Léonard (2022). Thus, the internal diameter,  $D$ , is chosen identically in the first instance, i.e. 0.05 m (Olbert et al., 2007). Concerning the overall heat transfer coefficient,  $U$ , the same constant value is used as well, i.e. 400 W/m<sup>2</sup>/K (Boda et al., 2017), assuming that the coolant is pressurised water at 206°C. One part of the analysis is to study the influence of this coolant temperature and its overall heat transfer coefficient on the temperature control.

### III.5.3 Momentum balance

The last balance to be implemented in the reactor model is the momentum balance used to assess the pressure drop along the reactor. It should be specified that only the pressure drop in the reaction medium is considered and that it is assumed that the coolant medium pressure remains constant. A well-known equation to evaluate pressure drops in packed-bed tubular reactors is the Ergun equation (Fogler, 2016):

$$\frac{dP}{dx} = - \frac{u}{d_P} \cdot \left( \frac{1 - \phi}{\phi^3} \right) \cdot \left( \frac{150 \cdot (1 - \phi) \cdot \mu}{d_P} + 1.75 \cdot \rho \cdot u \right) \quad (\text{III.77})$$

Table III.5 gathers the meaning, value and units of all parameters and variables appearing in this equation. The bed void volume fraction value is already discussed in the material balance section. Concerning the catalyst particle diameter in the bed, its value is chosen to be equivalent to the one used by [Morales and Léonard \(2022\)](#). This diameter may seem a bit small compared to optimal values found in the literature ([Jess and Kern, 2009](#); [Kaskes et al., 2016](#)), which mostly lie between 1 and 2 mm. Thus, it is of interest to see the influence of this parameter on the pressure drop.

Variable	Meaning	Value	Units
$P$	total pressure	-	Pa
$x$	axial coordinate (length down the reactor)	-	m
$u$	superficial velocity (ratio of volumetric flow rate and cross-sectional area)	-	m/s
$\mu$	viscosity	-	Pa.s
$\rho$	density	-	kg/m <sup>3</sup>
<b>Parameter</b>			
$\phi$	bed void volume fraction	0.9	-
$d_P$	catalyst particle diameter	0.0005	m

Table III.5: Meaning, value and units of the variables and parameters used in the Ergun equation (see Equation III.77)

# Chapter IV

## Results analysis and discussion

In this chapter, an analysis of the results yielded by the Fischer-Tropsch reactor model described in the previous chapter is conducted. It starts with a validation study of the kinetics and stoichiometry implemented in the model, using experimental measurements performed by [Ma et al. \(2014a,b\)](#). Then, the reactor model is run with base case conditions that are identical to the one used by [Morales and Léonard \(2022\)](#) such that a comparison between the two models is possible. It enables seeing the impact of the kinetics and the stoichiometry on the reactor performance. The limits of the kinetics model are also investigated. The last section of this chapter covers sensitivity analyses performed on different parameters and variables taking part in the model to understand which are the most critical. Thus, these analyses aim to find the appropriate range for these variables and parameters to observe an optimal reactor operation.

### IV.1 Kinetics model validation

The validation concerns more the kinetics than the stoichiometry of the reactions, as [Ma et al. \(2014a,b\)](#) developed only a kinetic model and not a whole reactor model. However, if the reactor model developed in this study correlates with the experimental data, it should mean that both the kinetics and the stoichiometry are correctly implemented. An error in the stoichiometry of the reactions would lead to more consequential deviations from experimental measurements, even if the kinetic model is correctly set up.

The reactor model is slightly modified to perform this validation in comparison to what is described in the last chapter since [Ma et al. \(2014a,b\)](#) conducted their kinetics experiments in a continuous-stirred tank reactor, which is assumed to be at a constant temperature and pressure. It means that the energy and momentum balances both simplify to:

$$dT = 0 \quad (\text{IV.1})$$

$$dP = 0 \quad (\text{IV.2})$$

In other words, the inlet stream temperature and pressure are supposed to be the same as the outlet stream counterparts, equivalent to the conditions inside the reactor. Concerning the material balance, it does not make any derivative expression appear, and it is simply written as:

$$\dot{F}_i = \dot{F}_{i,0} + r'_i \cdot m_{\text{cat}} \quad (\text{IV.3})$$

which can be translated as the molar flow rate at the outlet of the reactor ( $\dot{F}_i$ ) being equal to its initial molar flow rate ( $\dot{F}_{i,0}$ ) plus its molar production rate ( $r'_i \cdot m_{\text{cat}}$ ), which is the product of its specific reaction rate and the mass of catalyst used in the reactor. It should be specified that the CSTR model assumes that the reactor is perfectly mixed. Thus, the temperature, pressure, concentration and reaction rates are identical at each reactor point, including its outlet.

Ma et al. (2014a,b) communicate their experimental data through the reaction rates  $r'_{FT}$  and  $r'_{\text{CH}_4}$ :

$$r'_{FT} = 3.694 \times 10^{-6} \exp \left( \frac{104 \times 10^3}{8.314} \left( \frac{1}{493.15} - \frac{1}{T} \right) \right) \cdot \frac{p_{\text{CO}}^{-0.31} \cdot p_{\text{H}_2}^{0.88}}{1 - 0.24 \cdot \frac{p_{\text{H}_2\text{O}}}{p_{\text{H}_2}}} \quad (\text{IV.4})$$

$$r'_{\text{CH}_4} = 2.925 \times 10^{-7} \exp \left( \frac{136 \times 10^3}{8.314} \left( \frac{1}{493.15} - \frac{1}{T} \right) \right) \cdot \frac{p_{\text{CO}}^{-0.86} \cdot p_{\text{H}_2}^{1.32}}{1 + 0.46 \cdot \frac{p_{\text{H}_2\text{O}}}{p_{\text{H}_2}}} \quad (\text{IV.5})$$

in the reactor (equivalently at the outlet of the reactor) at 220°C for different space velocities, total pressures (given in MPa) and syngas ratios. The space velocity ( $SV$ ) is expressed in NL/h/g<sub>cat</sub> and defined as a volumetric flow rate per unit of catalyst mass. This space velocity can be transformed into a molar flow rate using the ideal gas law without forgetting that  $SV$  is given at normal conditions (i.e.  $T^0 = 273.15$  K and  $P^0 = 1$  atm):

$$\dot{F} = \frac{\frac{SV^0}{1000} \cdot m_{\text{cat}} \cdot P^0}{1000 \cdot R \cdot T^0} = \frac{0.101325 \cdot SV^0 \cdot m_{\text{cat}}}{273.15 \cdot R} \quad (\text{IV.6})$$

where the superscript 0 refers to normal conditions,  $\dot{F}$  is the total molar flow rate expressed in kmol/h and  $m_{\text{cat}}$  the mass of catalyst used in the reactor in g. The reactor model is thus run for the different experimental conditions to calculate the partial pressures in CO, H<sub>2</sub> and H<sub>2</sub>O found at the outlet of the reactor such that they are incorporated in Equations IV.4 and IV.5 to calculate  $r'_{FT}$  and  $r'_{\text{CH}_4}$  and to compare their values with the experimental data. The squared correlation coefficient of the two data sets, i.e. the experimental and the model data sets, is calculated to quantify this comparison. It is defined for the reaction rate  $r_i$  as (Wehenkel, 2019):

$$r^2 = \left[ \frac{\sum_{i=1}^n (r_{i,\text{exp}} - \bar{r}_{\text{exp}}) \cdot (r_{i,\text{mod}} - \bar{r}_{\text{mod}})}{\sqrt{\sum_{i=1}^n (r_{i,\text{exp}} - \bar{r}_{\text{exp}})^2} \sqrt{\sum_{i=1}^n (r_{i,\text{mod}} - \bar{r}_{\text{mod}})^2}} \right]^2 \quad (\text{IV.7})$$

where  $n$  is the number of experimental conditions, the subscript 'exp' refers to the experimental data set, the subscript 'mod' to the model data set and a bar refers to the mean of the corresponding data set.

All the test conditions and their corresponding detailed results are found in Appendices B and C, respectively, where there are in the form of tables. But to have a visual representation of the results, a parity plot is constructed for  $r'_{FT}$  and  $r'_{\text{CH}_4}$ . A parity plot is a convenient way to display experimental and tabulated points and compare them. Each point in the graph corresponds to one of the experimental conditions for which the abscissa is the experimental value, and the ordinate is the model value. The straight line  $y = x$  is added to ease the comparison because if a point lies on this line, it means that the model value equals the experimental one, and thus the closer the point to the line, the closer the model and experimental values. The parity plot for the Fischer-Tropsch reaction rate is found in Figure IV.1, while the one for the methane reaction rate is in Figure IV.2. For both experimental procedures, the temperature was kept constant at 220°C for all tests, and the inlet stream only contained CO and H<sub>2</sub>.

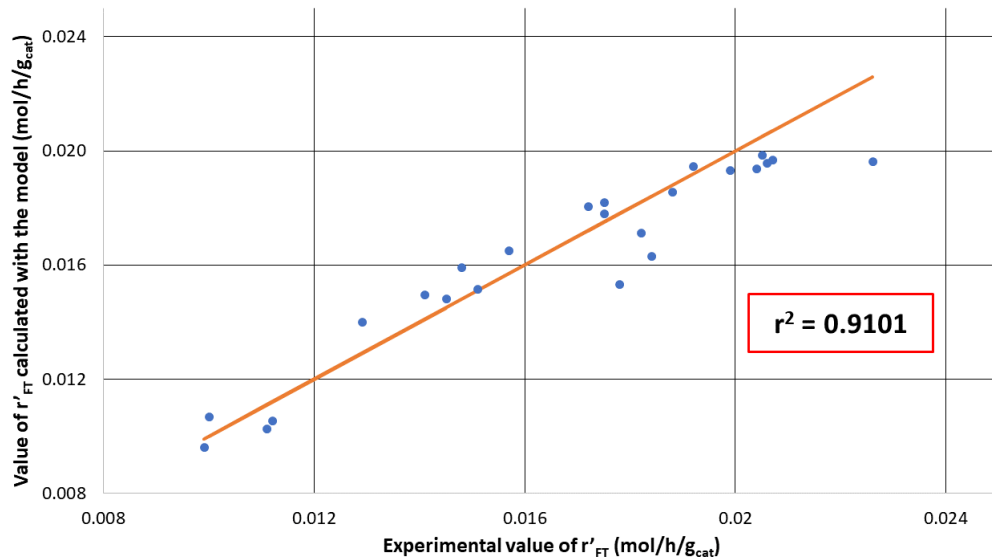


Figure IV.1: Parity plot for comparison of experimental (Ma et al., 2014a) and calculated Fischer-Tropsch reaction rate  $r'_{FT}$ . Their squared correlation coefficient  $r^2$  is also shown

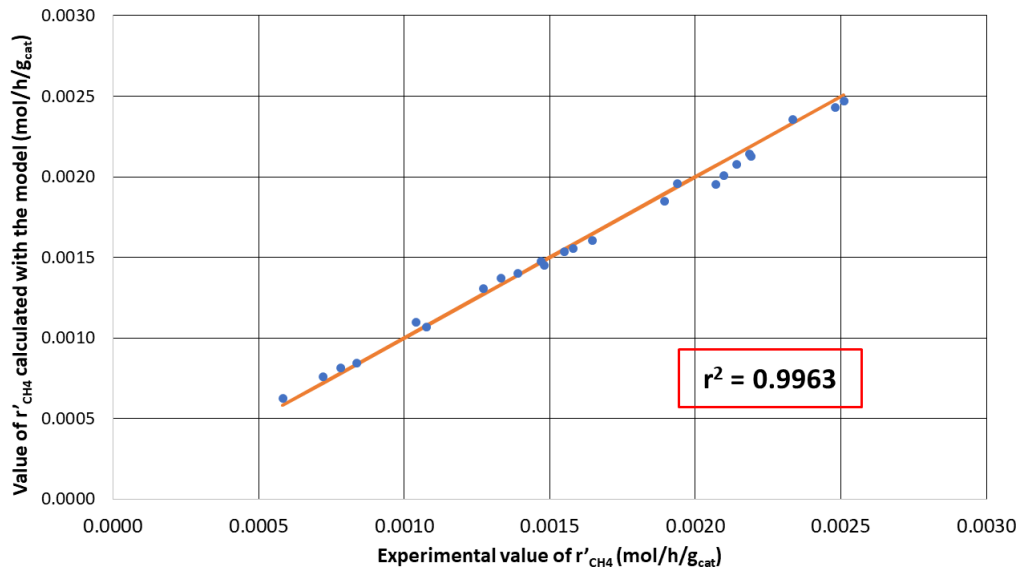


Figure IV.2: Parity plot for comparison of experimental (Ma et al., 2014b) and calculated methane reaction rate  $r'_{CH_4}$ . Their squared correlation coefficient  $r^2$  is also shown

The first thing that arises from these two parity plots is that the correlation between the calculated and experimental values is satisfactory for both reaction rates, exhibiting squared correlation coefficients above 90% in both cases. The correlation coefficient is close to 1 for the methane reaction rate for which  $r^2 = 0.9963$ . The squared correlation coefficient for  $r'_{FT}$  is high and close to 1 as well ( $r^2 = 0.9101$ ). An explanation of the difference between both values is given by calculating the squared correlation coefficient with which Ma et al. (2014a,b) validated their kinetics model. On top of their experimental data points, they provide the reaction rates calculated with their kinetics model (see Appendix C for the values). It turns out that the Fischer-Tropsch kinetics model is validated with a  $r^2 = 0.9209$  and the methane kinetics model with  $r^2 = 0.9948$ . It means that there is also a certain difference between the  $r'_{FT}$  and  $r'_{CH_4}$  squared correlation coefficient in their case. Furthermore, the



proximity of their  $r^2$  values with the respective ones calculated in this work suggests that the kinetics and the stoichiometry are correctly implemented in the current reactor model.

As mentioned previously, this validation ensures the correct implementation of the kinetics model and the reaction stoichiometry in the reactor model. However, this is done for a CSTR, while the developed model is for a tubular plug-flow reactor. Eventually, the reactor model needs to be validated with experimental data obtained on a tubular plug-flow reactor such that the correct implementation of the whole model is assessed. It will hopefully be possible with the future pilot installation at ULiège. Another worthy perspective concerning the model validation would be to validate the Fischer-Tropsch product distribution. In that way, it would fully ensure the correct stoichiometry model implementation. Here, it is assumed to be correctly implemented because it is supposed that errors in the stoichiometry would probably result in divergence in the kinetics model from experimental data.

## IV.2 Base case results

### IV.2.1 Analysis of inlet conditions

The conditions corresponding to the base case for the analysis of the reactor behaviour are the same as the one presented by [Morales and Léonard \(2022\)](#) in their work and are found in Table IV.1. These base case conditions come from the work of [Knutsen \(2013\)](#) and are typical of a low-temperature Fischer-Tropsch synthesis operated at lab scale.

<b>Molar flow rate (kmol/h)</b>	0.0915
<b>CO molar fraction (-)</b>	0.323
<b>H<sub>2</sub> molar fraction (-)</b>	0.677
<b>Syngas ratio (-)</b>	2.1
<b>Temperature (°C)</b>	210
<b>Pressure (bar)</b>	20

Table IV.1: Base case inlet conditions similar to [Morales and Léonard \(2022\)](#)

It is tested beforehand whether these inlet base conditions suit the objective pursued. In the scope of this study, the aim is to produce kerosene, i.e. to maximise the formation of products containing between 12 and 20 carbon atoms in the Fischer-Tropsch product spectrum. In other words, the goal is to maximise the mass fraction of C12-C20 products in the product spectrum. It is shown in Section III.3.1 that the product mass fractions in the distribution are calculated as:

$$w_n = n \cdot \alpha^{n-1} \cdot (1 - \alpha)^2 \quad (\text{IV.8})$$

where  $\alpha$  is calculated by:

$$\alpha = \frac{1}{1 + k_\alpha \cdot \left(\frac{C_{H_2}}{C_{CO}}\right)^\beta \cdot \exp\left(\frac{\Delta E_\alpha}{R} \left(\frac{1}{493.15} - \frac{1}{T}\right)\right)} \quad (\text{IV.9})$$

It is noticeable that the temperature and the syngas ratio intervene in this last equation, suggesting that these two equations can be used to check which temperature and syngas ratio ranges maximise the kerosene production. Figure IV.3 shows how the mass fraction of different product fractions evolves with the chain growth probability, which helps to seek the value maximising the C12-C20 fraction.

As can be seen, the product fraction corresponding to kerosene is maximised when the chain growth probability is around 0.9 or just slightly below. It is now possible to find for what temperature and syngas ratio this chain growth probability reaches a value around 0.9 with Equation IV.9.

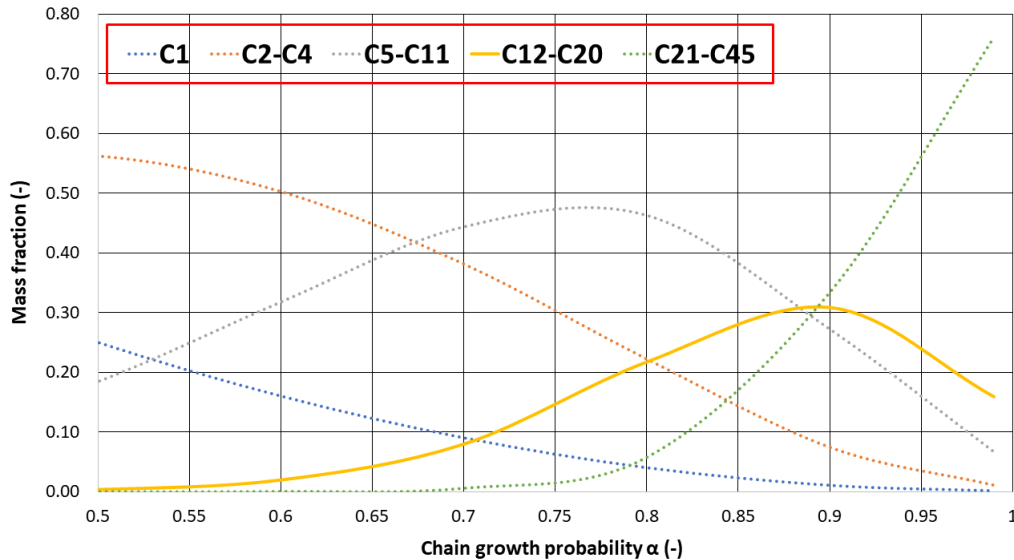


Figure IV.3: Variation of the mass fraction of Fischer-Tropsch product fractions with chain growth probability  $\alpha$

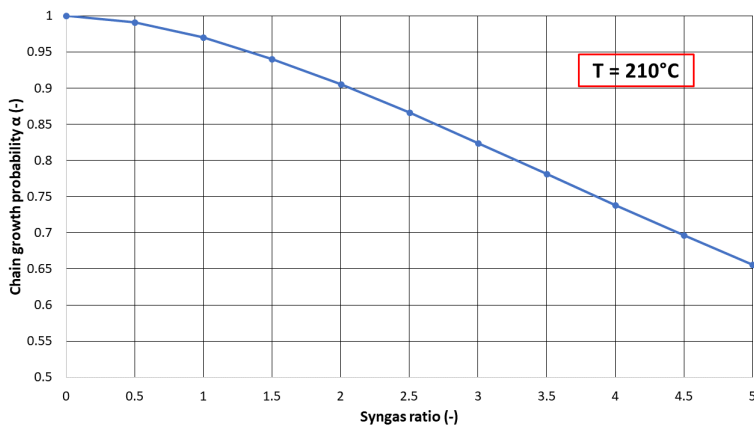


Figure IV.4: Variation of chain growth probability  $\alpha$  with syngas ratio,  $H_2/CO$ , at  $210^\circ C$

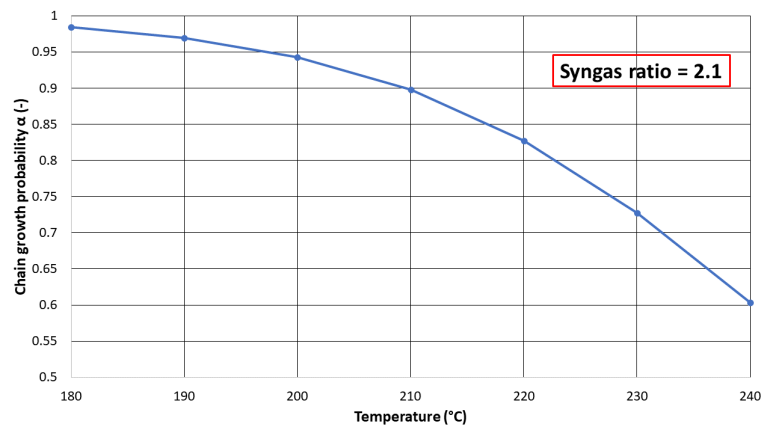


Figure IV.5: Variation of chain growth probability  $\alpha$  with temperature for a syngas ratio of 2.1

Figures IV.4 and IV.5 exhibit the chain growth probability decrease with both the syngas ratio and the temperature. The decrease induced by the syngas ratio increase is explained by the role played by  $H_2$  in the termination step and similarly by the role of  $CO$  in the propagation step. If the amount of  $CO$  is larger than the amount of  $H_2$ , i.e. if the syngas ratio is small, then the hydrocarbon chains are more likely to propagate, and the chain growth probability increases. Conversely, if the amount of  $H_2$  is greater than the amount of  $CO$ , the chains are more likely to be terminated, and the chain growth probability decreases. The temperature effect can probably be explained by the endothermic nature of the desorption, which is favoured at high temperatures, leading to a decrease in the chain growth

probability. As mentioned above, the chain growth probability must be around 90% or slightly below to maximise kerosene production. By looking at Figures IV.4 and IV.5, it turns out that the syngas ratio should be kept as much as possible a little bit above 2 and the temperature around 210°C to reach this optimal kerosene production. In conclusion, this small analysis enables showing the origin of the base case conditions presented in Table IV.1. These results are further supported by the literature (Botes et al., 2009; You and Wang, 2011).

## IV.2.2 Analysis of base case results

### IV.2.2.a Reactor performance

The point of this section is to compare the results obtained with two different kinetics, the one implemented by Morales and Léonard (2022) and the one presented in this work, and to observe to what extent the differences in these kinetics influence the reactor performance. For this comparison to be relevant, the inlet conditions are kept similar (see Table IV.1). They mention in their article that they reach a CO conversion of around 50% and 0.3 mol/h of C12-C20 hydrocarbon chains with a reactor of 2.5 L, which corresponds to a catalyst mass of 0.5 kg (volume/catalyst mass conversion performed with Equation III.67). The reactor has an internal diameter of 0.05 m and measures 1.275 m in length. Keeping identical specifications, the model developed in this work gives a CO conversion of 19% and a production of 0.1 mol/h of the hydrocarbon fraction of interest. To reach a conversion of 50% in CO with this model, the catalyst mass to be used should be equal to 1.25 kg, which is equivalent to a reactor of 6.25 L. Keeping the same length-to-diameter ratio as Morales and Léonard (2022), i.e. 25.5, the reactor would be 0.069 m in diameter and 1.75 m in length.

The difference observed in the reactor performance between these two models is explained by various factors. An explanation could be the fact that Morales and Léonard (2022) modelled the reactor for Fischer-Tropsch products containing up to 20 carbon atoms plus a lumped component for products containing between 21 and 30 carbon atoms. On top of that, only the paraffins were considered without accounting for the presence of olefins. Another explanation could be the differences in the stoichiometric coefficients attributed to Fischer-Tropsch products. However, these hypotheses only partly explain why there may be a different production of C12-C20 chains, but they cannot definitely explain such a big gap between the values and the difference in CO conversion. The main differentiation point comes from the kinetics model used in both reactor models. The kinetics model used by Morales and Léonard (2022) consists of two different reaction rates, one accounting for CO consumption through a classical Fischer-Tropsch reaction and the other accounting for its consumption by a methanation reaction (Iglesia et al., 1993; Panahi et al., 2012):

$$r'_{\text{Ig.,FT}} = \frac{2.105 \times 10^{-4} \cdot P_{\text{H}_2}^{0.6} \cdot P_{\text{CO}}^{0.65}}{1 + 33 \cdot P_{\text{CO}}} \quad (\text{IV.10})$$

$$r'_{\text{Ig.,CH}_4} = \frac{7.317 \times 10^{-6} \cdot P_{\text{H}_2} \cdot P_{\text{CO}}^{0.05}}{1 + 33 \cdot P_{\text{CO}}} \quad (\text{IV.11})$$

No temperature dependence is given for the kinetic constants appearing in these equations, but Iglesia et al. (1993) mention that the kinetics are valid between 200 and 210°C. The constants appearing in these equations are transformed such that the partial pressures are expressed in MPa and that the reaction rates are expressed in mol/s/g<sub>cat</sub>, just like the reaction rates used for this study (see Equations IV.4 and IV.5).

It is worth mentioning that  $-r'_{\text{Ig},FT}$  does not represent the whole CO consumption (contrarily to  $r'_{FT}$ , see Equation IV.4). According to [Iglesia et al. \(1993\)](#), the whole CO consumption is the sum of  $r'_{\text{Ig},FT}$  and  $r'_{\text{Ig},CH_4}$ . To draw a parallel with this work, the meaning of these reaction rates is equivalent to  $r'_1$  and  $r'_2$  derived in Section III.4 (see Equations III.32 and III.33). The total CO consumption can thus be written as:

$$r'_{\text{Ig},CO} = r'_{\text{Ig},FT} + r'_{\text{Ig},CH_4} = \frac{P_{H_2} \cdot P_{CO}^{0.05} \cdot \left( 2.105 \times 10^{-4} \cdot P_{H_2}^{-0.4} \cdot P_{CO}^{0.6} + 7.317 \times 10^{-6} \right)}{1 + 33 \cdot P_{CO}} \quad (\text{IV.12})$$

It is worthy to compare this specific reaction rate for CO with the one calculated in this study (see Equation IV.4). To put these two models in perspective, the model presented in this work is run for a catalyst mass of 1.25 kg. The partial pressures in CO, H<sub>2</sub> and H<sub>2</sub>O are retrieved at each node in the reactor, and the instantaneous CO consumption rate is calculated with both kinetic models. The ratio of these two specific reaction rates down the reactor is plotted in Figure IV.6. The first thing that can be mentioned is that this ratio slightly decreases as the conversion progresses, which can be explained by the slower decline of CO consumption when calculated with [Ma et al. \(2014a\)](#)'s model. The positive kinetic effect of water in this model may be this feature origin.

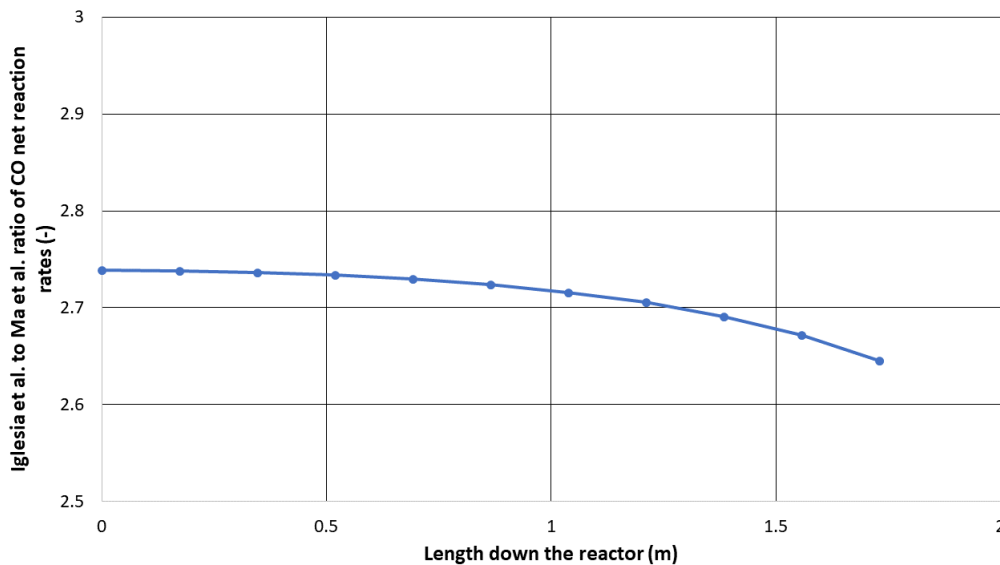


Figure IV.6: Evolution of ratio between CO net reaction rate calculated with [Iglesia et al. \(1993\)](#)'s model and the one calculated with [Ma et al. \(2014a\)](#)'s model down the reactor for 1.25 kg of catalyst in the base case conditions

Interestingly enough, it is notable that the ratio oscillates between 2.65 and 2.75 for the conditions found in the reactor. This pretty large ratio explains why one model concludes that 1.25 kg of catalyst is necessary to reach a 50% conversion, while the other model shows that only 0.5 kg is required. It is thus argued that the differences in the reactor performance mainly come from the different kinetic models used to describe CO consumption. When both kinetic models (Equations IV.4 and IV.12) are compared, it turns out that their intrinsic form differs. [Iglesia et al. \(1993\)](#)'s model obeys a Langmuir-Hinshelwood expression, while [Ma et al. \(2014a\)](#)'s model is based on a more complex expression involving a water kinetic effect (see Equation III.11). The fact that both models were derived from two different general kinetic expressions inevitably leads to differences in the observed results. The temperature dependence of both models could also bring some differentiation points. Nevertheless, this point is difficult to argue given that [Iglesia et al. \(1993\)](#)'s model does not make the temperature

dependence appear in its expression. However, it still seems that the kinetic constant plays a significant role in differentiating both models as the one for [Iglesia et al. \(1993\)](#)'s model is around two orders of magnitude greater than the one for [Ma et al. \(2014a\)](#)'s model.

Then, the point is to understand why two models that are supposed to describe the same physical phenomenon lead to such a difference in the conclusions. The first information is that both kinetics models were regressed with two catalysts which are not perfectly similar. As a catalyst has its specific kinetics, it inevitably leads to variations in the results. [Ma et al. \(2014a\)](#) mention in their article that the catalyst used for their experiments is an unpromoted 25%Co/Al<sub>2</sub>O<sub>3</sub> catalyst, but [Iglesia et al. \(1993\)](#) only specify that they used a SiO<sub>2</sub>-supported Co catalyst without mentioning details on the catalyst loading, catalyst particle size or the potential utilisation of a promoter. According to the literature, it seems that the catalyst support influences the selectivity of the Fischer-Tropsch products through structural effects inducing transport limitations, which are also influenced by metal particle size ([Ma et al., 2004](#); [Hodala et al., 2021](#)). On the other side, it seems that catalyst loading has a significant effect on syngas conversion ([Iglesia et al., 1992](#); [Ma et al., 2004](#)). Thus, a difference in the loading of the catalyst used to regress the kinetics model could be a motive explaining the differences. However, this assumption is partly denied by the fact that the kinetics used in [Morales and Léonard \(2022\)](#)'s model is the one modified by [Panahi et al. \(2012\)](#) who transformed the kinetics model to express it in more convenient units by assuming a catalyst loading of 20%.

This discussion testifies that it is hard to conclude the origin of the significant differences observed in the kinetics models, except that the two catalysts used to derive them are not perfectly similar. A solution that could bring more information to this discussion would be to compare the results provided by these two models with the ones stemming from a third model. Another step would be to compare the two plug-flow reactor models with experimental data obtained in a reactor with the same catalyst to keep the most general expression. Even if the model developed by [Ma et al. \(2014a\)](#) includes the influence of the water kinetic effect and is associated with a more complex stoichiometry, it does not guarantee a more general representation of Fischer-Tropsch kinetics. Another idea could be to see to what extent [Iglesia et al. \(1993\)](#)'s model can predict [Ma et al. \(2014a,b\)](#)'s experimental data. The ultimate step will be to confirm the results provided by the model with experimental measurements performed on the future lab-scale installation at ULiège. Another conclusion arising from these observations is that the quantitative results presented in this work should be taken carefully, especially for the sensitivity analyses presented below. However, the qualitative information brought by these analyses remains relevant in principle, as it shows how the reactor model behaves with respect to some of its parameters and variables.

#### IV.2.2.b Temperature profiles

On top of these considerations on the reaction kinetics, the analysis of the base case results also testifies the cooling system efficiency for maintaining the temperature inside the reactor around 210°C. The inlet temperature of the cooling medium is set at 206°C and its flow rate to a sufficiently high value (30 kmol/h) such that its temperature is kept more or less constant. The temperature profiles inside the reactor and the cooling medium are represented in Figure [IV.7](#). The temperature profile inside the reactor shows a slight increase at the entrance caused by the exothermicity of the reaction followed by a slow temperature decrease along the reactor, demonstrating the proper functioning of the cooling system. As mentioned earlier, it is desired to keep the temperature close to 210°C to optimise the C12-C20 fraction production, which is pretty well respected in this situation where the largest gap is 1.6°C. As shown in the following sensitivity analyses, it is possible to keep the

temperature even closer to 210°C by varying different parameters.

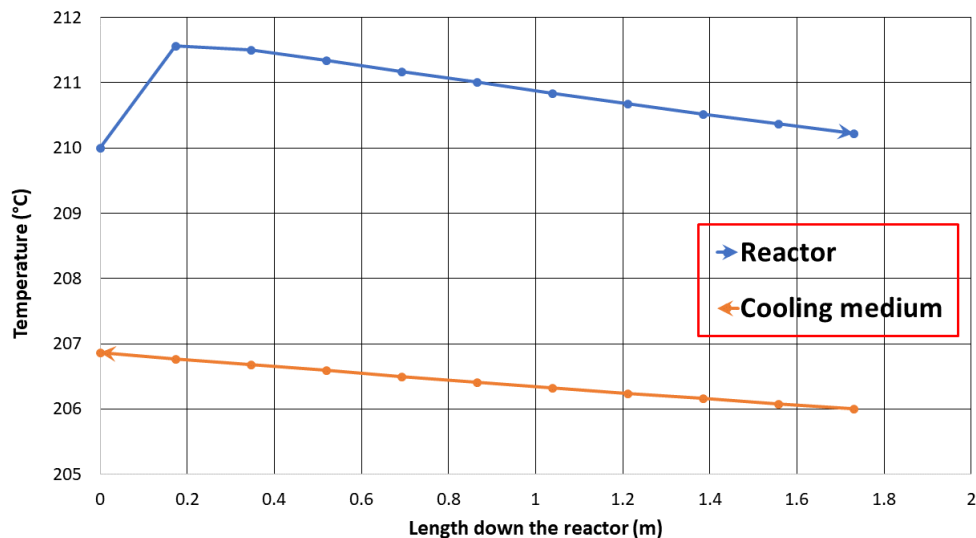


Figure IV.7: Temperature profiles of the reactor and cooling medium for 1.25 kg of catalyst in the base case conditions

It is worth highlighting the fact that a temperature slightly above 210°C is beneficial from a kinetic point of view and thus for syngas conversion, but not for maximising jet fuel production as explained earlier (see Figure IV.5). The decision concerning the ideal operating temperature is then influenced by the objective pursued, but it must be kept in mind that higher the temperature, faster the deactivation mechanisms, especially sintering (Tsakoumis et al., 2010). Concerning the cooling medium temperature profile, its inlet corresponds to the reactor outlet because of the counter-current mode of the flow. It is observable that its temperature moderately increases along the reactor with an overall temperature variation of less than 1°C. This temperature could be kept even more constant by increasing the flow rate of the coolant or using a coolant with a greater molar heat capacity. More insights about the influence of some parameters on the reaction temperature control are given below.

#### IV.2.2.c Pressure profile

As explained in the previous chapter, the Ergun equation aims at considering the pressure drops in the reactor. It is interesting to observe how the total pressure in the reactor evolves and whether or not significant pressure drops are experienced. As the pressure inside the cooling medium is assumed to be constant, only the pressure profile inside the reactor is represented in Figure IV.8. It is apparent in this figure that the pressure drop in the reactor is negligible and that the total pressure remains equal to its initial value all along the reactor. This result may seem questionable in the first instance, as one of the first-mentioned drawbacks of packed-bed reactors is the significant pressure drops that they may experience compared to other reactor types (Sie and Krishna, 1999). Nevertheless, the pressure drop scales with the square of the superficial velocity, as can be seen in the Ergun equation (see Equation III.77). Thus, as the base case conditions correspond to a lab-scale reactor, the flow rate is mild, inducing a low superficial velocity. On an industrial scale, the flow rate becoming much greater, it results in greater pressure drops. Another reason for the small observed pressure drop is the high catalytic bed porosity (see Table III.5), inducing a lowered constraint for the flow. For lower porosity values, the flow is more constrained due to higher friction forces with catalyst particles and



thus inducing higher pressure drops. The impact of different parameters on the pressure drops in the reactor is further discussed below.

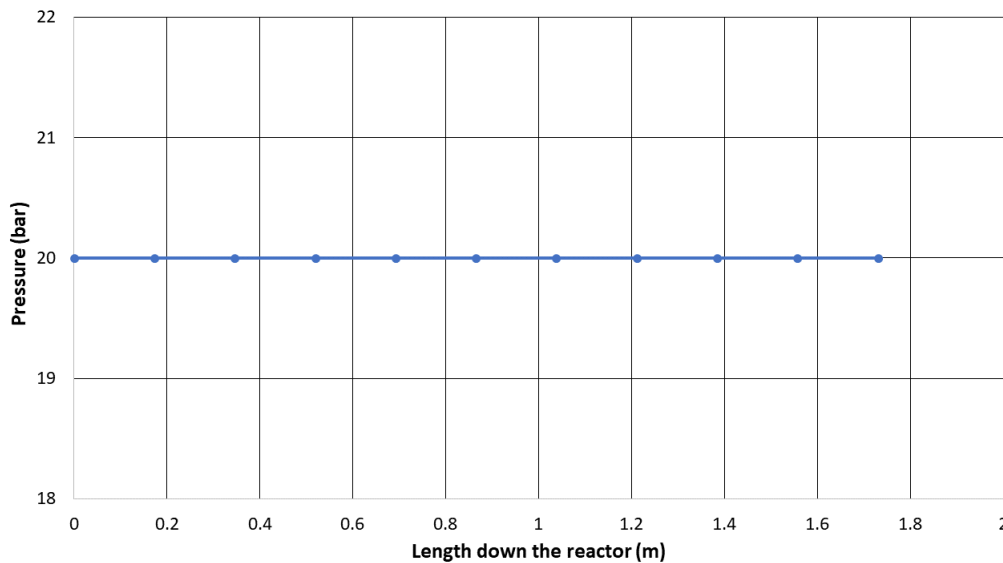


Figure IV.8: Pressure profile in the reactor for 1.25 kg of catalyst in the base case conditions

#### IV.2.2.d Fischer-Tropsch product distribution

Another point discussed in this base case results analysis concerns the Fischer-Tropsch product distribution. It is shown in Section III.3.1 that if Fischer-Tropsch products follow an ideal ASF distribution, the logarithm of their molar fraction in the product spectrum is linearly proportional to the number of carbon atoms in the hydrocarbon chain. In the scope of this model, it is assumed that all Fischer-Tropsch products follow an ideal ASF distribution except for methane, for which its observed deviation is considered. It is verified by constructing a plot similar to the one represented in Figure III.4, but this time with the results yielded by the model evaluated in the base case conditions and for a catalyst mass of 1.25 kg. The above-mentioned plot is represented in Figure IV.9.

The first thing to mention about this plot is that the regression is performed on all points except the one associated with methane, as it is not part of the ideal ASF distribution, unlike the other products. The methane deviation is represented in this graph, as shown by the corresponding molar fraction being several times larger than if methane had followed the ideal distribution. It is mentioned in the literature that the observed methane carbon-atom selectivity is typically found between 3 and 10%, while the selectivity predicted by the ideal distribution is around 1% (Todic et al., 2017). This statement is verified in this case by calculating both carbon-atom selectivities, which are defined in general terms as (Förtsch et al., 2015):

$$S_n = \frac{n \cdot m_n}{\sum_{i=1}^{\infty} i \cdot m_i} \quad (\text{IV.13})$$

where  $m_i$  is the molar fraction of hydrocarbon chains containing  $i$  carbon atoms in the product spectrum. The results show that the actual methane selectivity is 9.1%, whereas the methane selectivity that would be obtained from the ideal distribution is 1.2%, which correlates with the literature. The methane selectivity predicted by the ASF model is calculated using the linear regression equation noticeable in Figure IV.9.



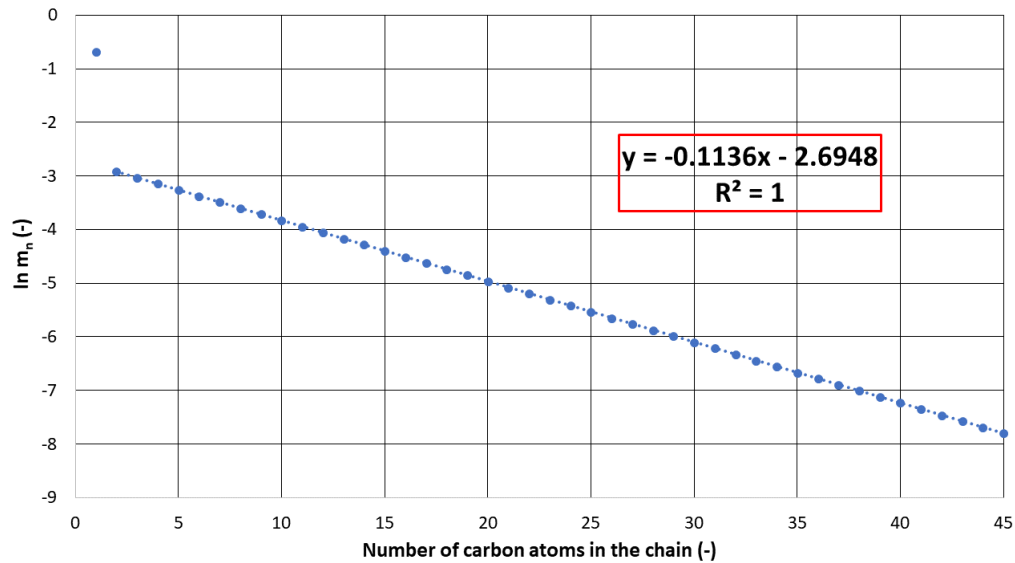


Figure IV.9: Distribution of Fischer-Tropsch product molar fractions in the product spectrum at the reactor outlet for 1.25 kg of catalyst in the base case conditions

As it is shown by Equation III.22, the slope of the straight line describing the ideal ASF distribution equals  $\ln \alpha$ . Then, it is possible to calculate the chain growth probability associated with the distribution shown in Figure IV.9 using the equation of the linear regression. It turns out that it corresponds to a chain growth probability of 0.893. This value is put in perspective with the  $\alpha$  values observed along the reactor, which are gathered in Table IV.2 with their corresponding mean value.

Length down the reactor (m)	Value of $\alpha$ (-)	Temperature ( $^{\circ}\text{C}$ )	Syngas ratio (-)
0	0.898	210	2.1
0.17	0.889	211.6	2.097
0.35	0.889	211.5	2.095
0.52	0.890	211.3	2.092
0.69	0.892	211.2	2.089
0.86	0.893	211.0	2.085
1.04	0.894	210.8	2.082
1.21	0.895	210.7	2.078
1.38	0.897	210.5	2.074
1.56	0.898	210.4	2.070
1.73	0.899	210.2	2.066
<b>Mean value</b>	<b>0.894</b>	<b>210.8</b>	<b>2.084</b>
<b>Standard deviation</b>	<b>0.0035</b>	<b>0.51</b>	<b>0.011</b>

Table IV.2: Evolution of chain growth probability  $\alpha$ , temperature and syngas ratio down the reactor with their corresponding mean value and standard deviation for 1.25 kg of catalyst in the base case conditions

It is noticeable in this table that the mean  $\alpha$  value in the reactor is close to the value obtained from the linear regression equation with a relative difference of 0.15%. It is also interesting to recall that, as discussed above, the base case conditions are such that they correspond to an optimal C12-C20 frac-

tion production, which is possible if  $\alpha$  is around 0.9 or slightly below. This condition is maintained in the reactor, which is quantified by the standard deviation around the mean equal to 0.0035. The origin of this small standard deviation for the chain growth probability is on one side, the small variation of temperature along the reactor, which is enabled by the proper functioning of the cooling system and on the other side, the small variation of the syngas ratio.

This consistency in the syngas ratio is related to its initial value and the relative consumption of  $H_2$  and CO. An initial amount of CO equal to  $Q_0$  is considered to develop this statement. The initial  $H_2$  amount is assumed to equal  $SR_0 \cdot Q_0$ , resulting in an initial syngas ratio of  $SR_0$ . According to this assumption, the quantity of CO left at the  $i^{\text{th}}$  step in the reactor is written as:

$$Q_{CO}(i) = Q_0 - i, \quad \forall i \geq 0 \quad (\text{IV.14})$$

where it is supposed that 1 mol of CO is consumed at each step. Similarly, the quantity of  $H_2$  left is written:

$$Q_{H_2}(i) = Q_{H_2}(i-1) - C_{H_2}(i-1), \quad \forall i > 0 \quad (\text{IV.15})$$

where  $C_{H_2}$  corresponds to the consumed amount of  $H_2$  per consumed mole of CO, which is calculated as:

$$C_{H_2} = \frac{r'_1}{r'_{FT}} \cdot U_{H_2} + \frac{r'_2}{r'_{FT}} \cdot 3 \quad (\text{IV.16})$$

where  $r'_{FT}$  corresponds to the overall CO consumption rate (see Equation IV.4),  $r'_1$  and  $r'_2$  to the CO consumption rate in Reactions III.28 and III.29, respectively, and where  $C_{H_2}$  corresponds to an overall stoichiometric coefficient for  $H_2$ . It is calculated with the weighted average of its two stoichiometric coefficients in Reactions III.28 and III.29. The syngas ratio at the  $i^{\text{th}}$  step is thus equal to:

$$SR(i) = \frac{Q_{H_2}(i-1) - C_{H_2}(i-1)}{Q_0 - i} \quad \forall i > 0 \quad (\text{IV.17})$$

If the initial syngas ratio  $SR_0$  is exactly equivalent to the consumed amount of  $H_2$  per consumed mole of CO at the entrance of the reactor ( $C_{H_2}(0)$ ), then the syngas ratio at node 1 is:

$$SR(1) = \frac{Q_{H_2}(0) - C_{H_2}(0)}{Q_0 - 1} = \frac{SR_0 \cdot Q_0 - SR_0}{Q_0 - 1} = \frac{SR_0 \cdot (Q_0 - 1)}{Q_0 - 1} = SR_0 \quad (\text{IV.18})$$

which induces that the syngas ratio at the first node in the reactor equals its initial value. Then the syngas ratio at the second node in the reactor is calculated by:

$$SR(2) = \frac{Q_{H_2}(1) - C_{H_2}(1)}{Q_0 - 2} \stackrel{(\text{IV.15})}{=} \frac{Q_{H_2}(0) - C_{H_2}(0) - C_{H_2}(1)}{Q_0 - 2} \quad (\text{IV.19})$$

For this reasoning, the assumption of an isothermal reactor is made, such that only the effect of the syngas ratio and not the one associated with temperature variation is observed. It signifies that if two nodes have the same syngas ratio and temperature, then they have the same chain growth probability  $\alpha$ , and thus the same hydrogen usage ratio  $U_{H_2}$ . Neglecting the variation of  $r'_1/r'_{FT}$  and  $r'_2/r'_{FT}$ , it is assumed that the overall  $H_2$  stoichiometric coefficient is equivalent from one node to the other in this situation. The last equation is thus simplified as:

$$SR(2) = \frac{Q_{H_2}(0) - C_{H_2}(0) - C_{H_2}(0)}{Q_0 - 2} = \frac{Q_{H_2}(0) - 2 \cdot C_{H_2}(0)}{Q_0 - 2} = \frac{SR_0 \cdot Q_0 - 2 \cdot SR_0}{Q_0 - 2} = SR_0 \quad (\text{IV.20})$$

and it is shown that the syngas ratios at the three first nodes are equivalent. If this reasoning is extended to the other nodes of the reactor, it is proven that the syngas ratio remains constant all along the reactor, given the fact that the temperature is constant and that the initial syngas ratio equals the initial overall  $H_2$  stoichiometric coefficient. It implies that for an isothermal reactor operating at a given temperature, there exists only one initial syngas ratio that is such that its value will remain unchanged as the reaction proceeds. This value is calculated by solving the following equation for  $SR_0$ :

$$SR_0 = \frac{r_{1,0}}{r_{FT,0}} \cdot \left\{ 2 + \frac{1 - \left[ 1 + SR_0^\beta \cdot \exp \left( \frac{\Delta E_\alpha}{R} \cdot \left( \frac{1}{493.15} - \frac{1}{T} \right) \right) \right]^{-1}}{1 + e^{-0.3}} \right\} + \frac{r_{2,0}}{r_{FT,0}} \cdot 3 \quad (IV.21)$$

which is obtained by incorporating the definition of  $\alpha$  (see Equation IV.9) in the hydrogen usage ratio definition (see Equation III.61), which is used in Equation IV.16 where the initial overall  $H_2$  stoichiometric coefficient equals the initial syngas ratio. This equation, as it is constructed, implies that the initial syngas ratio,  $SR_0$ , which is sought, is equivalent to the initial overall  $H_2$  stoichiometric coefficient,  $C_{H_2,0}$ , thus inducing a steady value of the syngas ratio in the reactor, as just explained.

The results show that the initial syngas ratio should equal 2.145 to observe this trend. It is graphically demonstrated in Figure IV.10 where the variation of the syngas ratio down the reactor is represented for three different initial values. For the construction of this plot, the reactor is assumed to be isothermal to observe only the effect of the syngas ratio and not the one associated with temperature variation, as already mentioned. It is observable on this plot that for an initial syngas ratio of 2.145, its value remains more or less constant at each point of the reactor, as expected from the previous discussion.

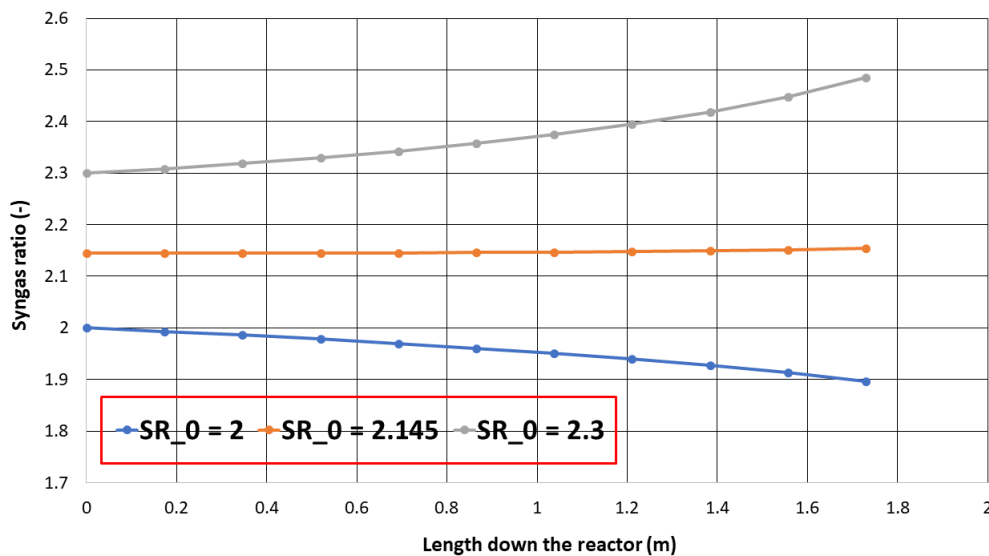


Figure IV.10: Evolution of syngas ratio in an isothermal reactor as a function of its initial value for 1.25 kg of catalyst in the base case conditions

Its value is not perfectly constant down the reactor because only a slight deviation in the value of the syngas ratio impacts the  $\alpha$  value. It induces a hydrogen usage ratio variation, influencing the value of the overall  $H_2$  stoichiometric coefficient, impacting the following syngas ratio,... The assumption according to which the  $r'_1/r'_{FT}$  and  $r'_2/r'_{FT}$  ratios are constant at each point of the reactor may also

have an influence. For this initial value of 2.145, the relative difference between the outlet and inlet syngas ratio is less than 0.5% and is probably caused by an accumulation of small imprecisions that are reported in the different equations at the various points in the reactor. However, the syngas ratio is assumed to be roughly constant in the reactor, given the negligible variation of the value between the inlet and the outlet.

For the two other curves, the initial syngas ratio is either greater or smaller than the pivot value of 2.145, and it is observed that the distance between the syngas ratio and this value gradually increases as the reaction proceeds. Interestingly enough, it is noticed that if the initial syngas ratio is smaller than the pivot value, it decreases along the reactor, whereas it increases if its initial value is greater than 2.145. The reason for this observed trend is explained with the equations presented above. The difference in syngas ratio between node 1 and node 0 writes:

$$\begin{aligned} SR(1) - SR(0) &= \frac{SR_0 \cdot Q_0 - C_{H_2}(0)}{Q_0 - 1} - SR_0 = \frac{SR_0 \cdot Q_0 - C_{H_2}(0) - SR_0 \cdot Q_0 + SR_0}{Q_0 - 1} \\ &= \frac{SR_0 - C_{H_2}(0)}{Q_0 - 1} \quad (IV.22) \end{aligned}$$

It turns out that the syngas ratio at node 1 is greater than the initial syngas ratio if this latter is greater than the initial overall  $H_2$  stoichiometric coefficient. Conversely, if the initial syngas ratio is lower than this initial coefficient, the difference above becomes negative, leading to a syngas ratio at node 1 smaller than the initial value. In other words, it confirms the patterns observed in Figure IV.10.

This mathematical reasoning is simplified by considering the chemical meaning of the three configurations illustrated in Figure IV.10. If the initial syngas ratio is greater or lower than the initial  $H_2$  overall stoichiometric coefficient, it signifies that the reagents are not in stoichiometric amounts. In the situation where the syngas ratio is greater,  $H_2$  is the excess reagent, meaning that a fraction of the initial  $H_2$  amount never reacts, as CO is consumed in the first place. Then, as the reaction proceeds, both the numerator and denominator of the syngas ratio decrease. The numerator tends towards a finite value, while the denominator tends towards 0, resulting in a ratio increasing along the reactor and tending towards infinity. For the situation concerning a lower initial syngas ratio, CO is in excess compared to  $H_2$ . In this configuration, the numerator tends towards 0, while the denominator tends towards a finite value, inducing a syngas ratio tending towards 0. The fact that in one situation, the ratio heads towards infinity, whereas it heads towards 0 in the other one may be an explanation for the greater increase of the syngas ratio for which the initial value is 2.3 compared to the decrease in the syngas ratio starting at 2, as can be seen in Figure IV.10. This hypothesis seems to be confirmed when the mass of catalyst used increases, i.e. for a greater conversion in the reactor.

### IV.3 Reactor sizing and kinetics model limits

As explained previously, a reactor of 2.5 L, equivalent to a catalyst mass of 0.5 kg, leads to a conversion of 50% for Morales and Léonard (2022)'s model and 19% for this model. If the catalyst mass is increased up to 1.25 kg, the model studied in this work reaches the 50% CO conversion. Then, it would be interesting to determine the reactor volume, equivalently the catalyst mass, corresponding to an optimised conversion. As the reactions dealt with in this study are not limited to an equilibrium, the conversion can theoretically reach 100%. For an isothermal reactor, which is the case here as the temperature is kept constant as much as possible, it is shown that the conversion evolution along the reactor is qualitatively represented as in Figure IV.11. It is shown in Section III.5.1 that the variation

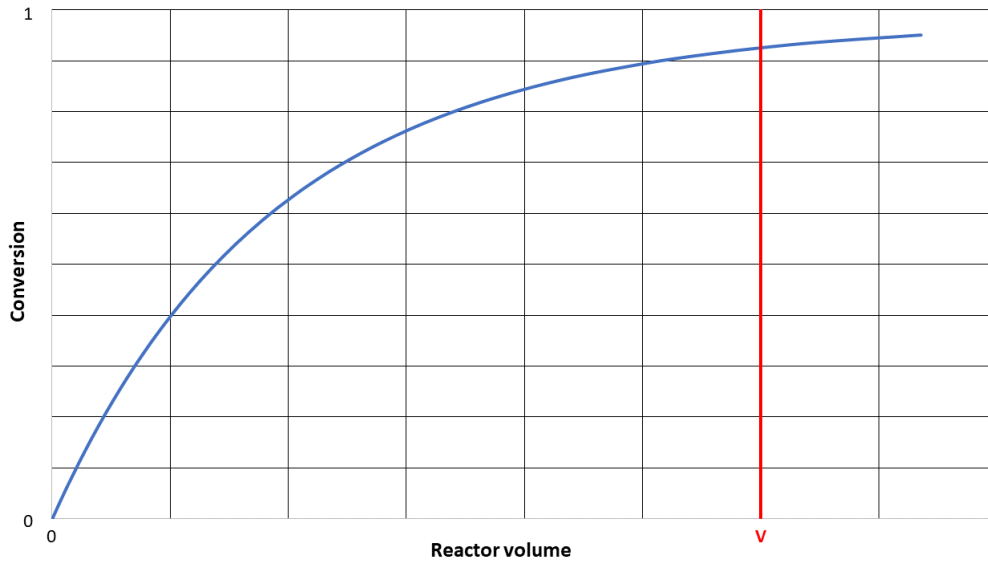


Figure IV.11: Qualitative representation of the conversion evolution with reactor volume for an isothermal plug-flow reactor

of the flow rate of component  $i$  with the reactor volume writes:

$$\frac{d\dot{F}_i}{dV} = r_i \quad (\text{IV.23})$$

Knowing that the conversion of component  $i$  is calculated as:

$$X = \frac{\dot{F}_{i,0} - \dot{F}_i}{\dot{F}_{i,0}} \quad (\text{IV.24})$$

where  $\dot{F}_{i,0}$  is the initial molar flow rate of component  $i$ , the differential equation is transformed in:

$$\frac{dX}{dV} = \frac{-r_i}{\dot{F}_{i,0}} \quad (\text{IV.25})$$

Assuming that  $i$  is a reagent,  $r_i$  becomes negative by definition, meaning that the conversion increases with the reactor volume. As the consumption rate of component  $i$  is maximal at the inlet of the reactor, the concentrations being maximal, the slope of a curve describing the conversion evolution with the reactor volume is maximal at the entrance. The curve slope progressively decreases, given that the consumption rate tends towards 0 as the reagent concentrations decrease. This brief reasoning correlates with the qualitative sketch represented in Figure IV.11. The optimal reactor volume is generally chosen when this curve starts to flatten because, at this point, the increase in the reactor volume necessary to reach the next per cent of conversion becomes too large. For instance, this decision can be made from an economic point of view: the optimal reactor volume corresponds to the point where the additional cost induced by the volume increase is not compensated by the additional revenues obtained by the higher reached conversion. Such an optimal reactor volume is qualitatively represented in red in Figure IV.11.

This methodology could be applied to the model developed in this study to find an optimal reactor volume. However, the general form of the Fischer-Tropsch reaction rate:

$$r'_{FT} = \frac{k_{FT} \cdot p_{\text{CO}}^{a_{FT}} \cdot p_{\text{H}_2}^{b_{FT}}}{1 + q_{FT} \cdot \frac{p_{\text{H}_2\text{O}}}{p_{\text{H}_2}}} \quad (\text{IV.26})$$

prevents this application. It is explained in Section III.2 that  $q_{FT}$  is negative, translating a positive water kinetic effect. Because of this negative sign, the denominator in the reaction rate progressively tends towards 0 as the conversion increases, keeping in mind that the water partial pressure increases while the  $H_2$  partial pressure decreases. This feature leads to a discontinuity in the kinetics model, which is characterised by a vertical asymptote. Thus, the model can only be used in a given conversion range. This limiting condition occurs when the denominator equals zero leading to:

$$1 - 0.24 \cdot \frac{p_{H_2O}}{p_{H_2}} > 0 \quad (IV.27)$$

where  $q_{FT}$  is replaced by its actual value and where it is specified that the denominator must be strictly positive. On the other side of the vertical asymptote, the reaction rate  $r'_{FT}$  would become negative, inducing CO production instead of its consumption, which is not physically possible. The kinetics model is thus valid as long as the conversion is such that the following condition is respected:

$$\frac{p_{H_2O}}{p_{H_2}} < \frac{1}{0.24} \quad (IV.28)$$

Then, it is possible to find the limiting reactor volume, or equivalently limiting catalyst mass, imposed by the structure of the kinetics model and its associated limiting conversion. This limiting value is of course dependent on the inlet conditions which are here the base case conditions. It is done by plotting the ratio of water and  $H_2$  partial pressures as a function of the catalyst mass, as represented in Figure IV.12, and finding the catalyst mass for which the ratio of the partial pressures equals 4.167.

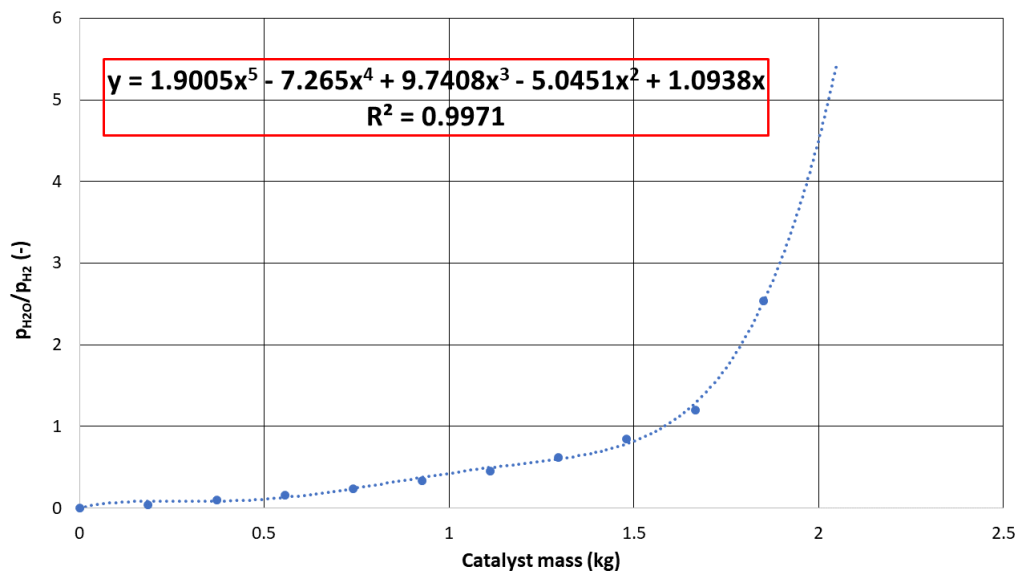


Figure IV.12: Evolution of water-to-hydrogen partial pressures ratio as a function of the catalyst mass used in the reactor in the base case conditions

In this situation, it is not that simple, as the model cannot run for the case where the ratio exactly equals its limiting value, as it would induce an infinite reaction rate. Then, the limiting value must be determined by the extrapolation of the numerically reachable points. It is observable in Figure IV.12 that the last reachable data point corresponds to a catalyst mass of 1.85 kg. A greater catalyst mass induces the solver convergence to fail, as the model gets too close to its limiting region. When using the regression equation presented in this figure, it can be calculated that the catalyst mass for which the ratio  $p_{H_2O}/p_{H_2}$  would reach 4.167 equals 1.9795 kg. Following the same assumptions

as previously, this is equivalent to a reactor volume of 9.9 L. As explained previously, this mass of catalyst, in these conditions, cannot ensure the proper run of the model. Therefore, it is not possible to know the associated CO conversion from the model. However, the conversion associated with the last reachable point, i.e. for a catalyst mass of 1.85 kg, is known from the model and equals 83.5%.

It leads to the conclusion that for the base case conditions presented above, the kinetics model developed by [Ma et al. \(2014a\)](#) is numerically valid for a conversion range between 0 and 83.5%. Above this conversion, the kinetics model has not reached its limiting value yet, as the ratio of the partial pressures is not yet equal to 4.167, but the reactor model fails to converge. A perspective for this project could be to modify this kinetics model for predicting the whole conversion range, from 0 to 100%. A hypothesis could be to build a model including the water partial pressure in the numerator instead of the denominator. In that way, when the partial pressure of one reagent equals zero, the reaction rate would be equal to zero as well ([Lualdi et al., 2011](#)).

The discussion conducted in the previous paragraphs is only correct from a mathematical point of view. In reality, there is strong evidence that the limiting conversion value is smaller than 83.5%. The determination of the validity range for the kinetics model conducted previously tolerates that at some point, the water kinetic effect can be such that the reaction rate  $r'_{FT}$  stops decreasing and starts increasing, as can be seen in Figure IV.13. In this figure, the coordinate along the reactor is the catalyst mass and no longer the reactor volume.

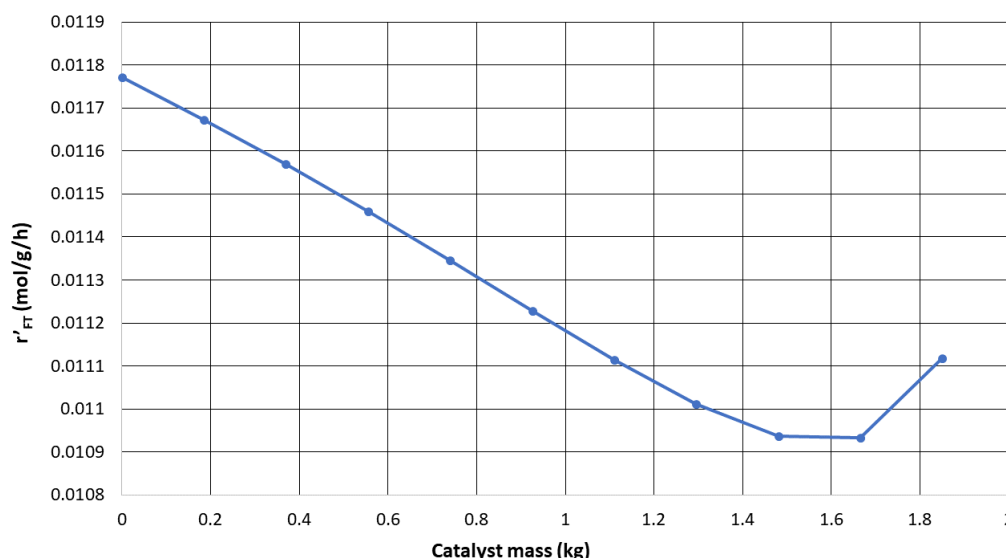


Figure IV.13: Evolution of Fischer-Tropsch reaction rate  $r'_{FT}$  along the reactor in the base case conditions

It is possible to find reaction examples in which the reaction rate increases in the reactor, namely the case of an exothermic reaction inducing a temperature increase. It leads to a larger kinetic constant value increase compared to the decrease in the reagent concentrations resulting from the reaction progress. In the present case, it is not a temperature effect but a component effect which is discussed. Thus, the chemical feasibility of such an increase is questioned.

As already said previously, the kinetic effect of water during Fischer-Tropsch synthesis over cobalt-based catalysts is the scope of various discussions in the literature. Many studies showed that the introduction of water in the reactor leads to an increase in the reaction rate ([Okoye-Chine et al.,](#)



2019). However, another study performed on Re-promoted  $\text{Co}/\gamma\text{-Al}_2\text{O}_3$  catalyst shows that the positive kinetic effect of water seems to level off as the water partial pressure increases, induced by a rapid and extensive deactivation of the catalyst (Lögberg et al., 2011). This water kinetic effect attenuation seems to be contradictory with the rise observed in Figure IV.13 at advanced conversion values. Then, the validity domain of the kinetics model should be further restricted to be in harmony with the observations made by Lögberg et al. (2011). Thus, the Fischer-Tropsch reaction rate would not observe such an increase at higher conversion. In that configuration, the kinetics model could not be applied for conversions as high as 83.5%, but it is difficult to determine the new boundary. One solution could be to validate the utilisation of the kinetics model only if the reaction rate decreases with the conversion. In that case, the validity boundary limit would be for a catalyst mass of around 1.67 kg, corresponding to a CO conversion of 71%. However, even this proposition seems to hide a too strong positive kinetic effect of water. It is noticeable in Figure IV.13 that the decrease in the reaction rate between a catalyst mass of 1.48 and 1.67 kg is negligible compared to the one between 1.3 and 1.48 kg. The reagent concentrations approaching zero cannot explain it because it occurs for a reaction rate that is still pretty close to its initial value. The usual decrease in the slope of this type of graph is generally observed for reaction rates much closer to 0. Then, this softening of the slope can probably be attributed to a water kinetic effect increase, meaning that the validity range should be even more restricted to correlate with experimental observations. As this discussion testifies, it is tough to determine the validity range of the kinetics model to agree with a levelling off of the water kinetic effect as the reaction proceeds. The kinetics model should be modified to account for this observation. A proposition could be to use a water effect constant  $q_{FT}$  that decreases (in absolute value) when the water partial pressure rises in the reactor. Another idea could be the consideration of the deactivation induced by water in the kinetics (Pandey et al., 2021).

Another way to determine the limiting conversion value is to assume that, beyond the highest conversion experimentally reached by Ma et al. (2014a), the kinetics model is inaccurate. It ensures that the limiting conversion is reachable in reality, which is not the case with the less rigorous determination conducted above. However, it cannot be ensured that the kinetics model is undoubtedly inaccurate beyond the highest conversion reached by Ma et al. (2014a). Their highest reached conversion is 52% at 220°C, 17 bar, for a inlet total molar flow rate of 0.0013 kmol/h, an inlet syngas ratio of 2.5 and a catalyst mass of around 10 g. Thus, it turns out that the validity domain is even more restricted than before.

This section shows that it is laborious to determine accurately the kinetics model validity range. The limiting value can significantly vary, depending on the assumptions taken to assess this limit. It is shown that only considering the mathematical behaviour of the model may probably lead to a too loose tolerance on the limiting conversion value. It seems to be confirmed by the literature, which mentions a levelling off with the conversion of the positive kinetic effect induced by water. On the contrary, considering only the experimental data used to regress the model seems the strictest way to assess the validity domain. However, it does not ensure the model inaccuracy beyond this domain, and the restriction may be too strong. Two options are available to properly determine this kinetics model validity domain and should be further deepened in the future of this work. The first option consists in finding experimental values in the literature to see to what degree the kinetics model can predict experimental data. The other option is to directly conduct experiments, which would make it easier to find the validity range of the kinetics model by appropriately selecting the experimental conditions. It is an appealing perspective which could be considered for the future pilot plant at ULiège.

In the next section, sensitivity analyses are conducted. For some of them, the impact of the considered variable on the conversion is studied. As the validity domain of the kinetics model is not entirely determined yet, conversion may reach values greater than 52%, i.e. the maximal conversion observed experimentally by [Ma et al. \(2014a\)](#). Thus, some points may be conducive to greater uncertainty if they correspond to a high conversion value. However, even with these uncertainties, the global trend followed by the various curves should be valid, keeping in mind that the water effect may be overrated.

## IV.4 Sensitivity analyses

The sensitivity analyses presented in this section aim to give an insight into how the reactor model developed in this study behaves when some of its parameters and variables are varied. It is important to specify that the values of unvaried variables correspond to the base case conditions. The catalyst mass used for these simulations is 1.25 kg, i.e. the catalyst mass corresponding to a 50% CO conversion in the base case conditions. These sensitivity analyses can be split into three main categories. In the first instance, the influence of the feed variables on the reactor performance is assessed by studying key indicative variables, including CO conversion, C1 and C12-C20 mass fractions in the product spectrum, i.e. the mass fraction at the outlet of the reactor without including water and unreacted syngas. This variable is sometimes referred to as the given fraction selectivity. Then, it is shown how some variables can influence the temperature control in the reactor. Finally, the importance of the catalytic bed characteristics for the pressure drop and reactor performance is evaluated.

### IV.4.1 Operating variables influence on reactor performance

#### IV.4.1.a Operating temperature influence

The reactor is assumed to be isothermal to observe the temperature influence on the reactor performance. In that way, the temperature control quality does not interfere with the analysis. Exceptionally for this analysis, the catalyst mass used is not 1.25 kg but 0.5 kg because, at too high temperatures, the conversion reaches the kinetics model limit. Thus, decreasing the catalyst mass ensures that the model remains within its validity range, as discussed previously.

The first thing that arises in Figure [IV.14](#) is the fact that CO conversion increases rapidly with the reactor temperature. This trend underlines a kinetic effect, as kinetics are generally faster at higher temperatures. It is shown in Section [III.2](#) that the rate constants  $k_{FT}$  and  $k_{CH_4}$  follow a classical Arrhenius law, which exhibits an exponential dependence on temperature. It turns out that the associated reaction rates depend exponentially on the temperature, and therefore the CO consumption and its conversion as well.

Concerning the two other curves, they confirm that the optimal operating temperature is around 210°C, as it corresponds to a maximum in the C12-C20 mass fraction and a minimum for the methane mass fraction. To be more precise, it consists in an optimal situation for the separation steps coming after the reactor, as the difference in mass fraction between the desired product and the most undesired product is the largest at that point. However, if the easiness of the separation steps is not the pursued objective, but the goal is rather to maximise the production of the C12-C20 fraction, then the optimal operating temperature becomes 220°C as demonstrated in Figure [IV.15](#).

It is explained by the combination of two opposed phenomena. On one side, CO conversion increases with temperature and thus the formation of products as well. But on the other side, the chain growth

probability  $\alpha$  decreases with temperature and thus does the selectivity for the C12-C20 fraction, as shown in Figure IV.3. Between 220 and 230°C, the conversion increase cannot counterbalance the decrease in C12-C20 selectivity, resulting in the observed production decrease.

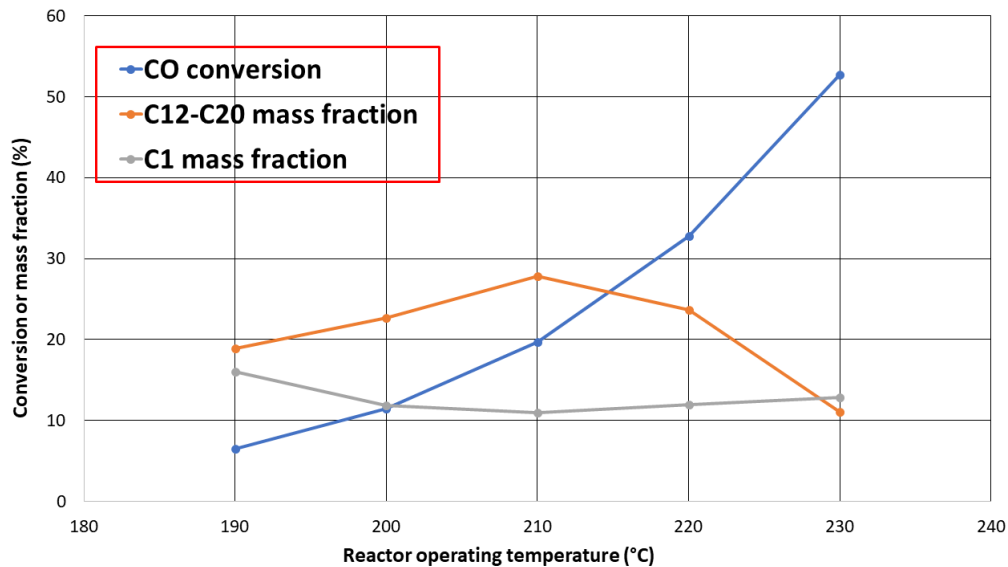


Figure IV.14: Influence of reactor operating temperature on CO conversion and methane and C12-C20 mass fractions at the reactor outlet for 0.5 kg of catalyst in the base case conditions

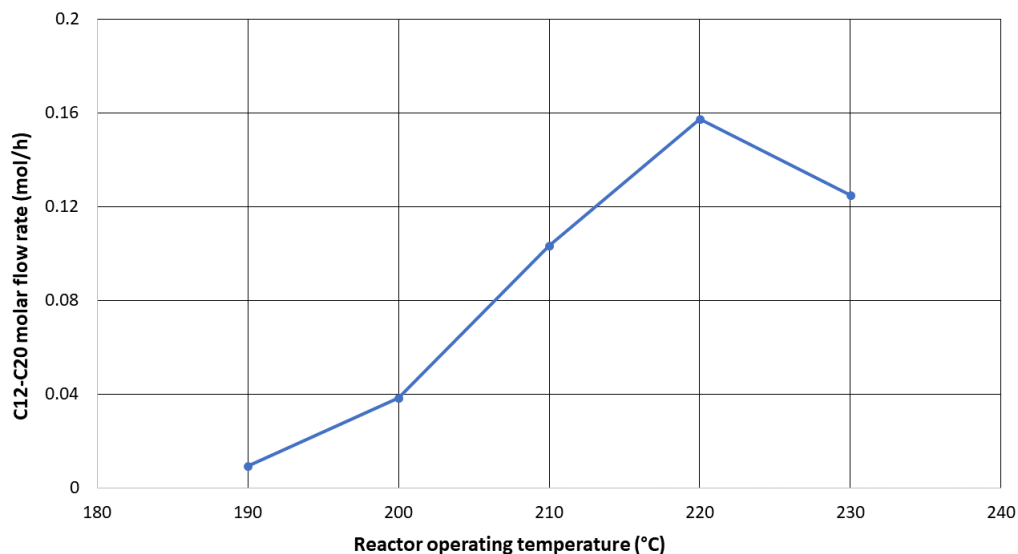


Figure IV.15: Influence of reactor operating temperature on the C12-C20 molar flow rate at the reactor outlet for 0.5 kg of catalyst in the base case conditions

Another interesting point in Figure IV.14 concerns the methane mass fraction. It is explained previously that the chain growth probability decreases with temperature and the methane mass fraction decreases with the chain growth probability. When gathering those two observations, it turns out that the methane mass fraction should increase with the temperature, but here it involves a minimum. However, methane does not follow the ideal ASF distribution, inducing, at low temperature, a higher observed mass fraction than expected, which is explained by a kinetic effect. As explained in Section

III.4, it is assumed that methane is produced through the ideal ASF distribution ( $r'_1$ ) and a second methanation reaction ( $r'_2$ ). It turns out that the methane production induced by  $r'_2$  is greater than the one induced by  $r'_1$  at low temperatures. The production stemming from the methanation reaction is sufficient to increase the methane mass fraction at low temperatures, explaining the curve trend observed in Figure IV.14.

Then, the situation in which methane is produced only by the ideal ASF distribution is considered to confirm this hypothesis, i.e.  $r'_2$  is assumed to be null. The evolution of the methane mass fraction in the reactor is investigated. In the scope of this assumption, it turns out that the methane mass fraction at low conversion is smaller than represented in Figure IV.14, and there is no more minimum in the curve. It justifies the hypothesis stating that the higher observed methane mass fraction is probably induced by the methanation reaction at low conversion. At high temperatures, this effect is hindered on one side, by the fact that the specific methane reaction rate linked to the ideal ASF production is greater than for the methanation reaction and on the other side, by the fact that the mass fraction should be high anyway following the lower  $\alpha$  value at this temperature.

#### IV.4.1.b Operating pressure influence

The influence of the reactor operating pressure is illustrated in Figure IV.16. It is noticeable that the CO conversion at the reactor outlet is higher when the operating pressure is intensified. For a given inlet composition, a higher operating pressure induces larger partial pressures of the reagents. Given the fact that the CO consumption rate is proportional to the partial pressures of the reagents, the consumption rate increases with the operating pressure. Thus, a higher conversion is achieved at the reactor outlet. The increase seems to be more or less linear in this case, which can probably be explained by the mild positive proportionality of the consumption rate to the overall pressure. Looking at Equation III.7, it appears that the CO consumption rate is proportional to  $P^{0.57}$ . If the pressure was further increased, and if the kinetics model did not feature a positive water kinetic effect, the curve would have presented a typical positive curvature associated with a function that is proportional to  $P^{0.57}$ .

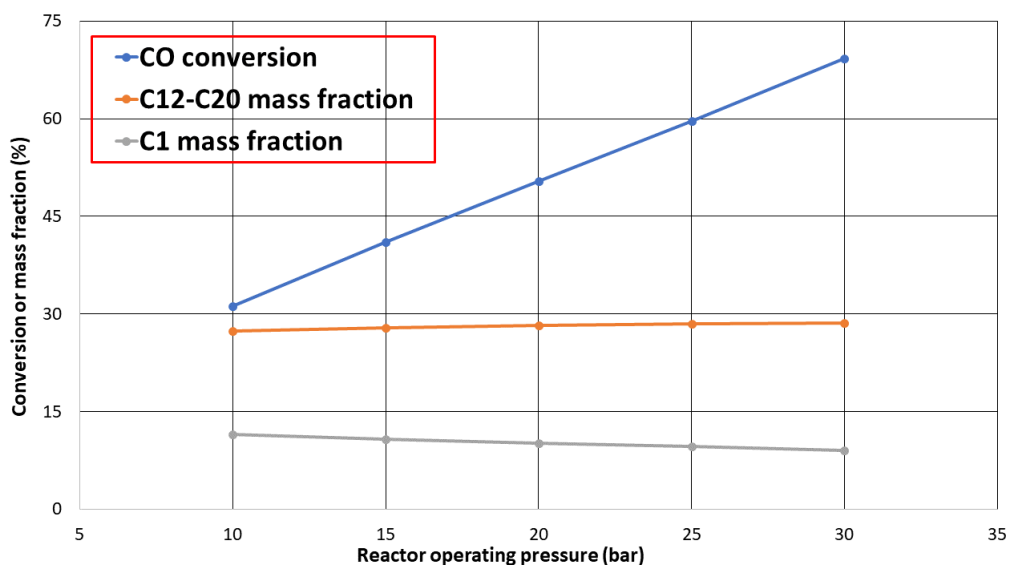


Figure IV.16: Influence of reactor operating pressure on CO conversion and methane and C12-C20 mass fractions at the reactor outlet for 1.25 kg of catalyst in the base case conditions

Unlike the temperature, the effect of the reactor operating pressure on the methane and C12-C20 mass fractions is less obvious, as shown by the orange and grey curves in Figure IV.16. The operating pressure should not influence the Fischer-Tropsch product distribution, as the chain growth probability only depends on temperature and syngas ratio. However, there is still a slight observable variation in the plot. It can presumably be explained by the fact that the temperature and syngas ratio variations along the reactor are not similar for each operating pressure. For each studied case, the initial temperature and syngas ratio are the same and correspond to the base case conditions, but the cooling system parameters are the same in each case as well. As the CO conversion varies, the heat released by the reaction also varies, thus explaining a different temperature variation in the reactor for the diverse operating pressures and then different selectivities obtained at the outlet. On top of this explanation, another effect might explain the slight observed variation. It turns out that the methane specific reaction rate associated with the additional methane production ( $r'_2$ ) is larger than the one concerning the ideal ASF production at 210°C, i.e. the base case temperature, and even more at low pressure. It might explain a larger methane mass fraction at low pressure. Lastly, it turns out that the molar production of the C12-C20 fraction is maximised at high pressure, given that its mass fraction in the product spectrum is relatively stable and that the CO conversion continually rises.

It is shown in the previous sensitivity analysis that the optimal operating temperature to maximise the C12-C20 mass fraction and the one to maximise the molar production do not coincide, inducing the necessity of a trade-off on the optimal temperature depending on the pursued objective. But with the observation made concerning the dependence on pressure, the mass fraction and the molar flow rate could be optimised by setting the temperature at 210°C, such that the selectivity is optimal and by imposing a high pressure to increase the molar production. In conclusion, it seems that the pressure and the temperature should be optimised in combination to ensure the best possible performance of the reactor.

#### IV.4.1.c Inlet syngas ratio influence

For the same reason concerning the kinetics model limits as explained for the operating temperature, this sensitivity analysis is conducted for a catalyst mass of 0.5 kg instead of 1.25 kg. The evolution of CO conversion and mass fractions of interest with the inlet syngas ratio is sketched in Figure IV.17. This figure shows that the CO conversion increases with the inlet syngas ratio. The kinetics model describing CO consumption (see Equation III.7) observes a positive dependence on the H<sub>2</sub> partial pressure, while its dependence on CO partial pressure is negative. Therefore, the kinetics are favoured at high H<sub>2</sub> and low CO concentrations, or in other words, at high syngas ratio.

The behaviour of the mass fraction curves is similar to the one in the analysis of the operating temperature, which is understandable as both the temperature and the syngas ratio decrease the chain growth probability  $\alpha$ . The optimal inlet syngas ratio seems to lie between 2 and 2.5, which correlates with the previous findings developed in Section IV.2.1. It turns out that this optimal syngas ratio is also close to the pivot value for which it remains constant all along the reactor, as discussed at the end of Section IV.2.2.d. It makes sense because for other inlet values, as they are distant from the pivot value, the syngas ratio experiences a stronger variation as the reaction proceeds, inducing a variation in the chain growth probability, which is detrimental from a selectivity point of view. Once again, the greater methane specific reaction rate for the methanation reaction ( $r'_2$ ) compared to methane production from the ideal ASF distribution ( $r'_1$ ) at low conversion can probably explain the minimum observed in the methane selectivity curve. It is worth mentioning that the optimal molar production of C12-C20 is reached for a syngas ratio slightly higher than the optimum for the mass fraction, similarly

as observed in the temperature analysis. The explanation behind this observation is the same as for the temperature: the syngas ratio increases the conversion but decreases the chain growth probability, just like the temperature does.

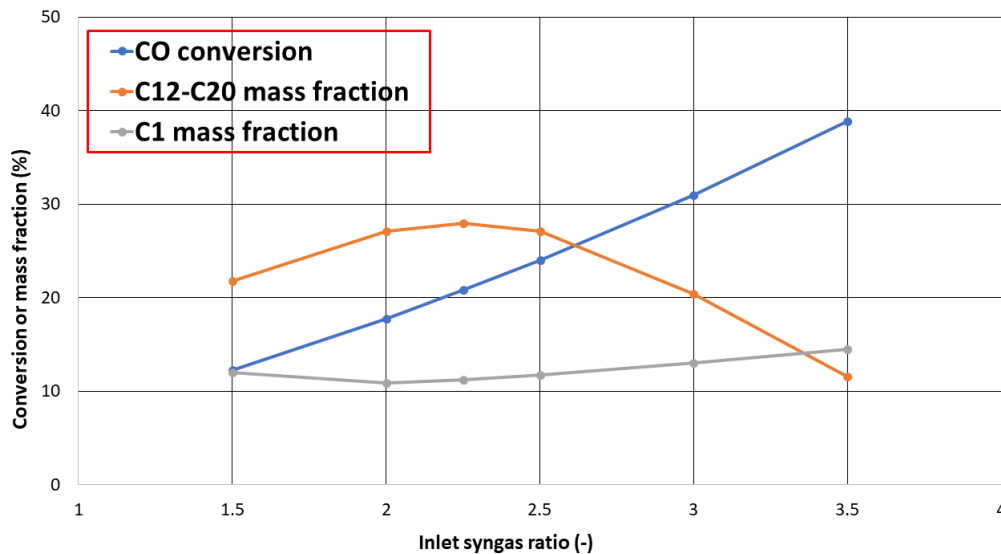


Figure IV.17: Influence of inlet syngas ratio on the CO conversion and methane and C12-C20 mass fractions at the reactor outlet for 0.5 kg of catalyst in the base case conditions

#### IV.4.1.d Inlet total flow rate influence

Figure IV.18 shows that the CO conversion decreases with the inlet total molar flow rate. If the overall flow rate is modified while maintaining all other variables constant, then the concentrations in the inlet stream are unchanged, and consequently, the partial pressures are also similar. It implies that the initial reaction rate is unchanged. However, as the overall flow rate increases, the molar flow rates of reagents inevitably increase. In these conditions, and for a given mass of catalyst, the amount of CO consumed is roughly identical whether the inlet flow rate is large or small. Then, for a small inlet molar flow rate, this CO consumption represents a large fraction of the available CO in the inlet stream, leading to a large conversion value. In other words, as the flow rate decreases, the residence time increases and thus does the conversion. The reasoning is reversed when having a high inlet flow rate. It is confirmed by the equation describing the evolution of the conversion along the reactor (see Equation IV.25) in which an inverse proportionality between the conversion and the inlet molar flow rate appears. It suggests that the conversion varies less rapidly for a higher inlet molar flow rate at a given reactor volume, equivalently a given catalyst mass, leading thus to a smaller conversion value at the outlet.

The inlet molar flow rate seems to have a negligible impact on the methane and C12-20 selectivities, which can be explained by the independence of the chain growth probability  $\alpha$  from the overall inlet flow rate. A small decay in the methane mass fraction can still be observed at high conversion values, i.e. at a low inlet molar flow rate. The additional methane amount brought by the methanation reaction ( $r'_2$ ) becoming less consequential at high conversion may explain this decrease. Then, if this methane source is reduced, the methane mass fraction decreases as, in the base case conditions, the  $\alpha$  value is such that the methane produced through the ideal ASF distribution is smaller than the methane produced by the methanation reaction.

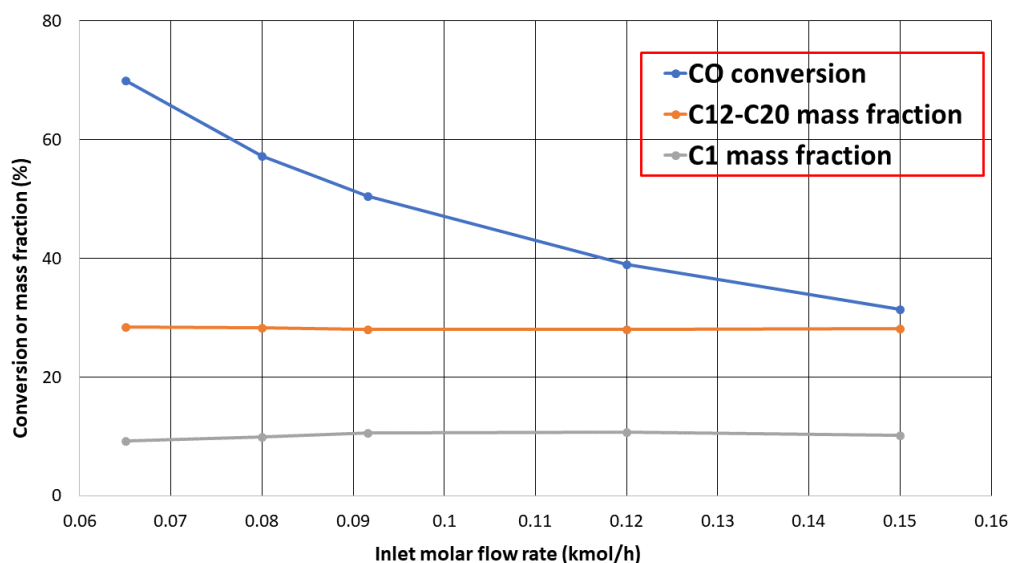


Figure IV.18: Influence of inlet total molar flow rate on CO conversion and methane and C12-C20 mass fractions at the reactor outlet for 1.25 kg of catalyst in the base case conditions

#### IV.4.1.e Influence of the presence of water in the inlet stream

As already discussed above, the kinetics model implemented in the studied reactor model features a positive water kinetic effect. Thus, it is of interest to seek the influence of the presence of water in the inlet stream by keeping all other variables as in the base case conditions, including an inlet syngas ratio of 2.1. In an actual installation, the presence of water in the inlet stream could be observed due to a recycle stream, when the whole water could not be eliminated in the separation steps. Figure IV.19 describes how CO conversion and methane and C12-C20 selectivities evolve with water content in the inlet stream varying between 0 and 15%.

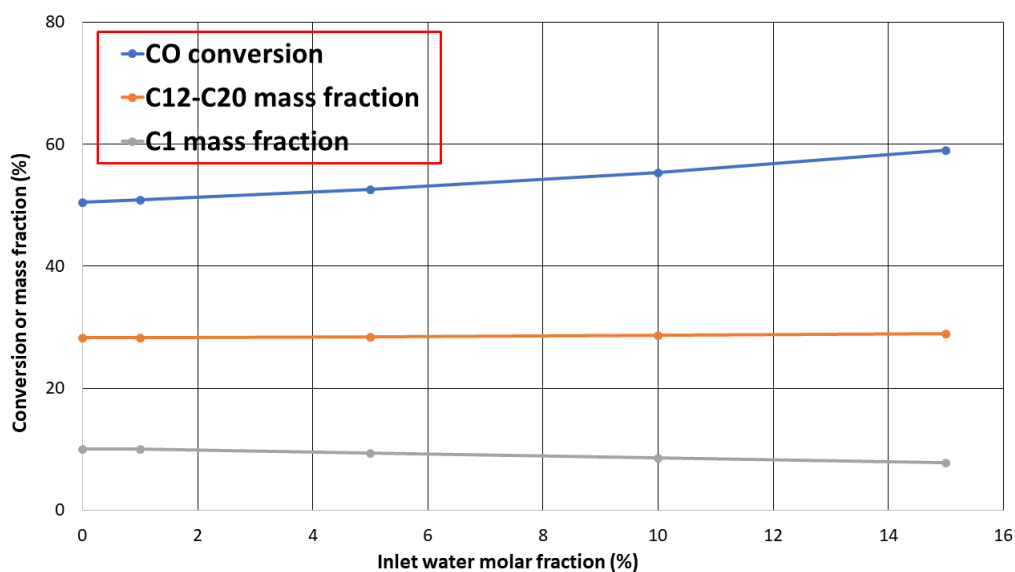


Figure IV.19: Influence of inlet water molar fraction on CO conversion and methane and C12-C20 mass fractions at the reactor outlet for 1.25 kg of catalyst in the base case conditions



It is noticeable that the conversion increases with the amount of water present in the reactor, which correlates with the presence of a positive water kinetic effect. The water partial pressure rise tends to increase the reaction rate through this positive kinetic effect, but it also causes a decrease in the partial pressures of the reagents, as the overall pressure is identical in all cases. If the conversion over the whole reactor is considered, the decrease in the concentration of the reagents is not sufficient to be detrimental for this conversion, and the water effect counterbalances it. It leads the conversion to increase and not decrease, as it would normally be expected from a reagents concentration decrease.

However, if the reaction rate is regarded at the beginning of the reactor, the water effect is not strong enough to counterbalance the lower concentrations, and the reaction rate is slightly higher when there is no water in the inlet stream. This phenomenon is depicted in Table IV.3 in which the inlet reaction rate is given for various inlet water contents. This observation is only valid at the beginning of the reactor because the consumption rate is globally higher in the whole reactor for higher water contents, as testified by the conversion increase observed in Figure IV.19. It is also observable in this figure that the water content seems to not influence the product selectivities, which can be explained by the fact that the chain growth probability does not depend on this variable. The small decrease in methane mass fraction at high conversion is probably due to the kinetic effect already explained in the other sensitivity analyses.

Inlet water content (%)	0	1	5	10	15
Inlet CO consumption rate (mol/h/g <sub>cat</sub> )	0.0118	0.0117	0.0117	0.0115	0.0114

Table IV.3: Inlet CO consumption rate for various inlet water contents for 1.25 kg of catalyst in the base case conditions

It is relevant to mention that such an increase in the conversion is only visible at steady-state. It was shown in the literature that the introduction of water in the reactor results in a decrease in the catalyst activity, probably due to water adsorption, reducing the number of active sites available for Fischer-Tropsch synthesis. The oxidation of catalyst particles leading to irreversible deactivation is also mentioned (Dalai and Davis, 2008; Ma et al., 2014a). Dalai and Davis (2008) state that the water effect can vary depending on the type of support that is used.

## IV.4.2 Cooling system variables influence on temperature control and reactor performance

### IV.4.2.a Comparison of co- and counter-current cooling

The better efficiency of a counter-current heat exchanger than a co-current heat exchanger is common engineering knowledge. The temperature difference diminishes along the exchanger length, and the temperatures on both sides of the exchanger tend towards the same value for a co-current heat exchanger. It induces the feature that a co-current heat exchanger is very efficient at the inlet, as the temperature difference is maximal, while its efficiency significantly decreases as it approaches the outlet due to a smaller temperature difference. In a counter-current heat exchanger, the temperature difference along the length is globally greater than in the case of a co-current exchange, leading to better heat transfer performance. Furthermore, the outlet temperature of one side of the exchanger is no more limited by the other side's outlet temperature. It is then interesting to observe to what extent the counter-current cooling is more efficient for maintaining the temperature in the reactor in the present model study and if there is any impact on the reactor performance.

Figure IV.20 shows the temperature profiles in the reactor and the cooling medium for a co-current cooling (dashed line) and a counter-current cooling (full line). The coolant inlet temperature and molar flow rate are the same in both cases. It is verified in the plot that the inlet coolant temperature is the same in both configurations with a value of 206°C. Interestingly enough, it turns out that its outlet temperature is the same, no matter the direction of the coolant flow, which is a consequence of the desire to keep this temperature as stable as possible by setting a large coolant flow rate. Concerning the temperature in the reactor, it is noticeable that the initial quick rise of the temperature is milder in the case of a co-current cooling, which is observed because of the slightly lower coolant temperature at the reactor inlet in that configuration. However, the counter-current cooling manages to bring back the reactor temperature close to the initial value of 210°C, unlike the co-current cooling, for which the reactor temperature continues slowly to increase. Even if this temperature rise is quite slow, it is expected to continue for higher conversion values. With a proper tuning and full optimisation of cooling system parameters, it would be possible to stabilise the reactor temperature at 210°C without further decrease, as the optimal catalyst operating temperature lies around 210°C.

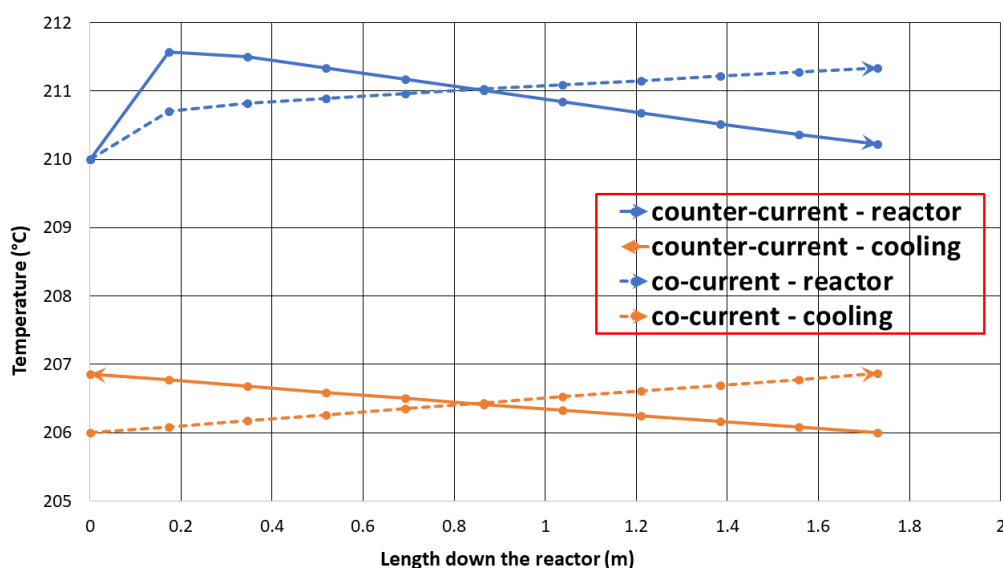


Figure IV.20: Comparison of the temperature profiles in the reactor and the cooling medium for co- and counter-current cooling modes for 1.25 kg of catalyst in the base case conditions

However, it should be mentioned that in this case, the temperature variations are small given the size of the installation, which is at lab scale. The heat released by the reaction is directly proportional to the amount of reagents converted and is thus more important for a reactor on a larger scale. Then, it turns out that these temperature modifications have a slight influence on the reactor performance, as shown in Table IV.4. The fact that the performance is better in the case of the co-current cooling can be attributed to a kinetic effect induced by a slightly higher temperature, as observed in Figure IV.20. However, the difference is not large enough to justify the utilisation of co-current cooling, especially if a bigger installation is considered, for which the expected temperature rise would be larger, as explained, and thus detrimental from a selectivity point of view.

This positive kinetic effect presence is highlighted by comparing the results with the values that would be obtained in a perfectly isothermal reactor, i.e. a reactor that would not experience any temperature rise and that would operate at each point at 210°C. The perfectly isothermal reactor yields a smaller conversion as it does not experience the positive kinetic effect induced by the temperature rise.

Variable	Counter-current cooling	Co-current cooling	Perfectly isothermal reactor
Conversion (%)	50.44	50.77	48.12
C12-C20 molar flow rate (mol/h)	0.2699	0.2725	0.2532
C12-C20 mass fraction (%)	28.20	28.24	28.04
C1 mass fraction (%)	10.16	10.14	10.18

Table IV.4: Influence of the cooling mode on CO conversion, C12-C20 molar production and methane and C12-C20 mass fractions at the reactor outlet for 1.25 kg of catalyst in the base case conditions. The values for a perfectly isothermal reactor are shown for comparison

#### IV.4.2.b Coolant inlet temperature and flow rate influence

In the frame of the analysis concerning the coolant inlet temperature influence, the reactor is cooled down in the counter-current mode with a coolant flow rate sufficiently large (30 kmol/h) to ensure its temperature maintain all along the reactor. Figure IV.21 represents how the temperature in the reactor evolves down its length for different inlet coolant temperatures.

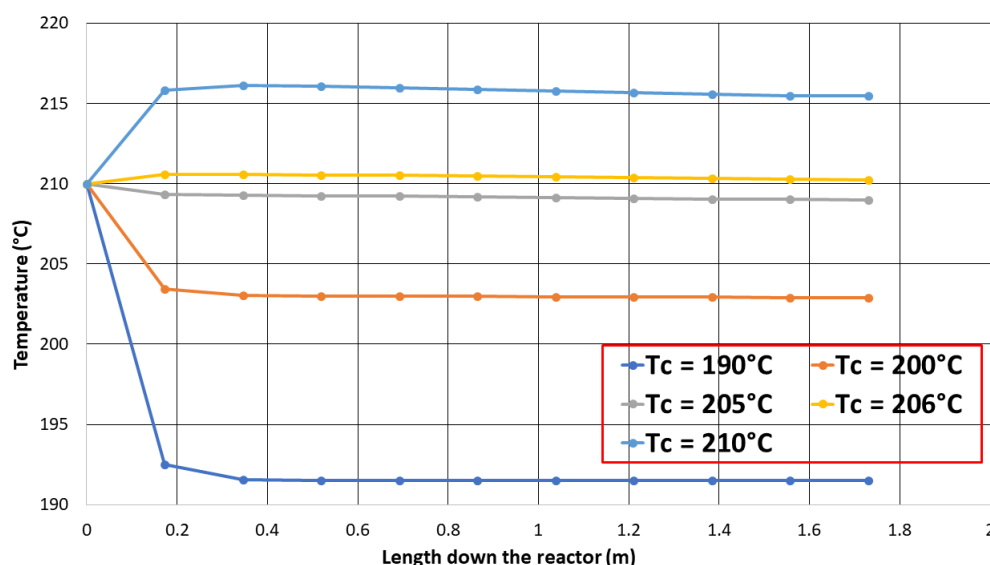


Figure IV.21: Inlet coolant temperature influence on the reactor temperature profile for 1.25 kg of catalyst in the base case conditions

The first thing that arises from this figure is that the cooling system is quite sensitive to the inlet coolant temperature, as only a small change in its value results in a different profile. It is seemingly a consequence of the small temperature variations for a reactor of this size, leading to a greater sensitivity to this variable. For instance, it is notable that the curve corresponding to an inlet coolant temperature of 206°C (i.e. the base case) observes a temperature rise, while the one corresponding to an inlet temperature of 205°C directly decreases. It suggests that the optimal coolant temperature is somewhat found between 205 and 206°C.

Then, it is interesting to observe the inlet coolant temperature influence on the reactor performance. Logically, the conclusions that are drawn from Figure IV.22 correlate with the ones made after the analysis of the operating temperature influence on the reactor performance. It is seen that the conversion increases with the coolant temperature, as the higher this temperature is, the more likely the

reactor temperature reaches high values and thus high conversions because of the positive temperature kinetic effect. Concerning the Fischer-Tropsch product selectivities, an optimal temperature seems to be around 206°C, which turns out to be the value for which the reactor temperature remains the closest to 210°C, as shown in Figure IV.21, keeping the chain growth probability in the optimal range that maximises the C12-C20 fraction.

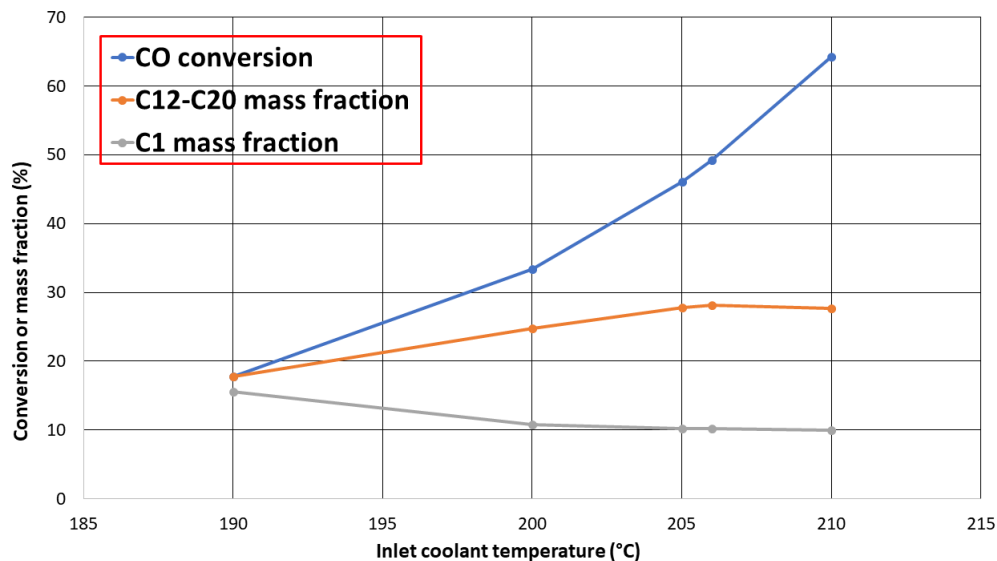


Figure IV.22: Inlet coolant temperature influence on CO conversion and methane and C12-C20 mass fractions at the reactor outlet for 1.25 kg of catalyst in the base case conditions

Concerning the optimal flow rate for the cooling medium, as already said, it should be as high as technically possible. The higher the flow rate, the more likely the coolant temperature will remain constant. Ensuring a constant temperature enables maximising the temperature difference with the reactor and thus optimising the heat transfer at each point. If the flow rate is not sufficiently large, the coolant temperature rises between its inlet and outlet, decreasing the temperature difference with the reactor at some points. On top of some technical considerations, the optimal flow rate should also be chosen from an economic perspective. It is assumed in this study that the coolant is pressurised water. However, after the first discussions concerning the future pilot installation at ULiège, it seems that the selected coolant would rather be a thermal oil. Then, it would be of interest to conduct an economic study to see if the thermal oil flow rate can be set as high as the water flow rate without being detrimental from an economic point of view.

#### IV.4.2.c Overall heat transfer coefficient influence

It is of interest to study the overall heat transfer coefficient influence because if a thermal oil is used instead of pressurised water, its value is susceptible to be larger than 400 W/m<sup>2</sup>/K, i.e. the value used in the base case conditions (Duratherm Extended Life Fluids, 2022). But it is also interesting to try to predict the effect of a coefficient going below 400 W/m<sup>2</sup>/K, which could result from a dysfunction of the cooling system induced by impurities or clogging, for instance. Figure IV.23 shows how the temperature profile along the reactor differs for different overall heat transfer coefficients,  $U$ , ranging between 250 and 1000 W/m<sup>2</sup>/K.

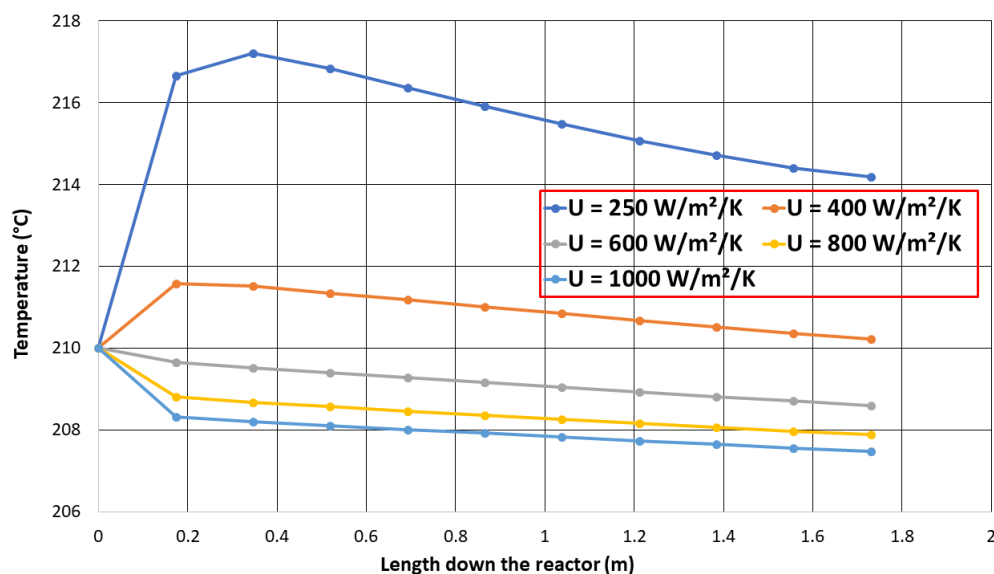


Figure IV.23: Overall heat transfer coefficient,  $U$ , influence on the reactor temperature profile for 1.25 kg of catalyst in the base case conditions

The first noticeable point in this figure is that a decrease in the overall heat transfer coefficient has a bigger impact on the temperature control than an increase in its value. It can probably be explained by the fact that in the heat transfer expression, the temperature is inversely related to the heat transfer coefficient. It is a relevant observation as it demonstrates the importance of maintaining the heat transfer coefficient at a high value. The heat transfer is optimised when the value increases, explaining why the reactor temperature reaches lower values. It suggests that if the chosen coolant and materials are such that the overall heat transfer coefficient is large, it enables the adaptation of the other cooling system parameters to less strict values. For instance, a larger coefficient would induce a milder sensitivity of the reactor temperature to the coolant temperature, meaning that small variations of this temperature would have a smaller impact on the reactor behaviour. Another advantage of having a large heat transfer coefficient is that it limits the temperature rise which is generally observed at the beginning of the reactor, a feature that is interesting in the case where the temperature variations in the reactor should be kept as negligible as possible.

These analyses of the cooling system variables show that proper optimisation of all variables should be performed to have the best temperature control possible. If the goal is to have the highest possible conversion, then the parameters tuning could be such that it allows some slight temperature rises. However, another tuning of the parameters should be considered if the objective is to keep the temperature as close as possible to a specific value.

## IV.4.3 Catalytic bed characteristics influence on pressure drop and reactor performance

### IV.4.3.a Catalytic bed porosity influence

In the analysis of the base case results (see Section IV.2.2), it is shown that there is no perceptible pressure drop in the reactor, which is supposed to be the consequence of the relatively small flow rate in the reactor due to the laboratory scale. A point not specified in that section is that lowering the initial pressure results in higher pressure drops in the reactor. However, in this situation, the pressure

drop remains negligible even if the pressure is decreased down to 10 bar. Another assumption made previously is that the catalytic bed porosity is set to 90%, which means that in a reactor of 1 m<sup>3</sup>, 0.1 m<sup>3</sup> is occupied by the catalyst bed. As mentioned in Section IV.2.2, this porosity value is relatively high. Thus, it is interesting to study how the pressure drop and the reactor performance evolve if this parameter is varied. The reactor is assumed to be perfectly isothermal to study the porosity influence on the pressure drop. It enables the dismissal of large temperature rises resulting from a porosity variation, as explained below. The pressure profiles for porosity values varying between 10 and 90% are shown in Figure IV.24.

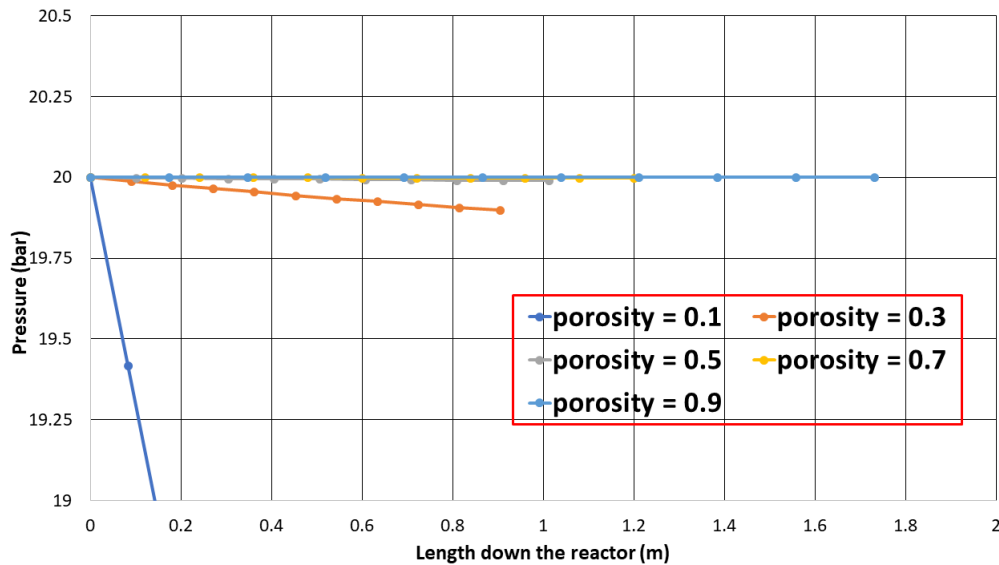


Figure IV.24: Catalytic bed porosity influence on the pressure profile in the reactor for 1.25 kg of catalyst in the base case conditions and a perfectly isothermal reactor

The first thing to notice in this figure is that the reactor length in each case is different since the simulation for each case is performed for the same catalyst mass (1.25 kg) but with a different catalytic bed porosity. As the calculation of the reactor volume from the catalyst mass includes the porosity (see Equation III.67), it is expected to have different reactor volumes and thus different reactor lengths.

It turns out that the higher the porosity, the longer the reactor, which makes sense as the lower the porosity, the denser the catalytic bed. Thus, the same amount of catalyst can be packed in a smaller volume. Concerning the pressure drop along the length, it appears that for a porosity above 50%, the passage of the flow is not enough obstructed to cause a perceptible pressure drop. Thus, it is assumed that if the porosity of the bed remains above 50%, the operating pressure remains more or less constant in the reactor. When this porosity is decreased, the resistance for the flow increases. It results in a larger pressure drop, as can be seen for the porosity values of 10 and 30%. At 30%, the pressure drop is still manageable, and as it is shown afterwards, the effect on reactor performance is negligible. However, at a 10% porosity, the flow experiences a too strong resistance, and the pressure drop becomes huge. The pressure at the reactor outlet for this porosity is not represented to ease the comparison, but it turns out that the pressure drop over the whole reactor at 10% porosity equals 5.9 bar. Note that the larger difference between the porosity of 10 and 30% than between 30 and 50% is a consequence of the inverse proportionality between the pressure variation along the length and the porosity in the Ergun equation (see Equation III.77).

It is then interesting to put these pressure profiles in perspective with the reactor performance reached with these different porosity values. Figure IV.25 shows the impact of the catalytic bed porosity on the CO conversion and methane and C12-C20 mass fractions in the product spectrum.

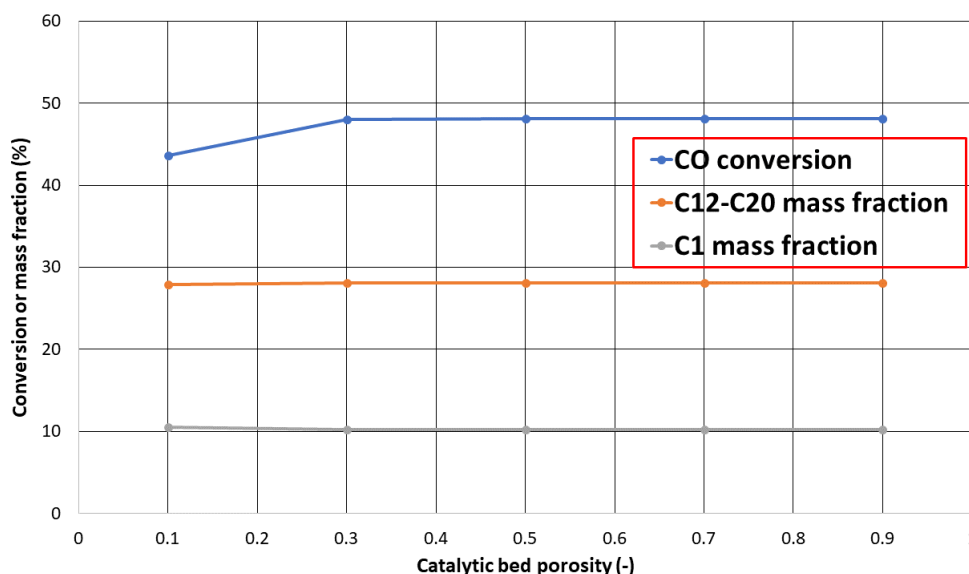


Figure IV.25: Catalytic bed porosity influence on the CO conversion and methane and C12-C20 mass fractions at the reactor outlet for 1.25 kg of catalyst in the base case conditions and a perfectly isothermal reactor

This figure matches the conclusions drawn from the sensitivity analysis performed on the reactor operating pressure, as it shows that the catalytic bed porosity does not influence the Fischer-Tropsch product selectivity. It also shows that the small pressure drop observed for a 30% porosity barely influences the conversion reached at the reactor outlet. A more visible impact is observed for the 10% porosity, which is understandable as the pressure is decreased by almost 6 bar between the reactor inlet and outlet, inducing a reagent concentrations decay and thus a lower achieved conversion.

As mentioned at the beginning of this section, the different pressure profiles available in Figure IV.24 are generated assuming a perfectly isothermal reactor. This decision is made because a decrease in the catalytic bed porosity induces significant temperature rises, inducing larger conversion and thus approaching the kinetics model limits. These large temperature rises can be explained by the increased density of the catalytic bed when its porosity decreases, which results in more catalyst per unit volume or equivalently per unit length. The consequence is that the same amount of CO is converted within a shorter reactor section, and thus the same amount of heat is released within this shorter section as well. As the cooling system parameters are not modified from one porosity value to another, the observed temperature rise at the reactor entrance increases as the catalytic bed density decreases. This observation sheds light on an important point: decreasing the catalytic bed porosity may be advantageous from an economic point of view, as it enables reaching a similar conversion with a shorter reactor (given the fact that the pressure drop remains manageable), but the temperature control becomes more complicated as the same amount of heat is released within a smaller volume. It implies a stricter cooling system parameters tuning which can become highly complicated. To take an example, using a catalytic bed porosity of 80% leads to a maximal deviation from the inlet temperature of 7°C, while it is only 1.6°C at 90% porosity (see Section IV.2.2). At 90% porosity, the cooling system manages to bring back the temperature close to 210°C, while at 80%, the outlet temperature is 214°C.



It was decided here to describe the effect of the catalytic bed porosity as it impacts both the pressure drop through the Ergun equation and the temperature control through the amount of heat released per unit length. However, it should be mentioned that the catalyst density has a similar effect on the temperature control because, in reality, it is truly the catalytic bed bulk density which has an influence through its apparition in the material and energy balances (see Equations III.65 and III.71, respectively). As mentioned previously, this catalytic bed bulk density is calculated as the product of the catalyst density and the bed solid fraction (i.e.  $1 - \phi$ ). On the other side, the catalyst density does not influence the pressure drop in the reactor.

#### IV.4.3.b Catalyst particle diameter influence

Figure IV.26 shows how the pressure profile in the reactor evolves as a function of the catalyst particles diameter. It is decided to generate this plot for a catalyst porosity of 30% to see a certain evolution in the pressure profile. The base case conditions normally consider a 90% porosity, but the pressure drop is negligible at that value. It can be seen that the larger the particle diameter, the lower the pressure drop, which is expected looking at the Ergun equation (see Equation III.77). It should be specified that the vertical axis scale is chosen to ease the comparison but unfortunately does not enable to see the outlet pressure for a 0.1 mm diameter. It turns out that the pressure drop over the reactor goes over 2.5 bar for a catalyst particle diameter of 0.1 mm.

From a physical point of view, smaller particles generate higher pressure drops because the intensity of the friction forces is greater in this case, induced by a greater specific surface area, which increases for small particles. Then, a sensible point of view would be to maximise the particle diameter to minimise the pressure drop in the reactor as much as possible. However, it should not be forgotten that if the particle diameter increases too much, diffusional transport limitations of reagents and products inside the particle could appear, leading to a decrease of the apparent kinetic constant. It is generally assumed that the apparent kinetic constant is inversely proportional to the particle diameter (Fogler, 2016). Then, a proper particle diameter analysis should be led to find a value that minimises pressure drop in the reactor while avoiding diffusional limitations inside the particle.

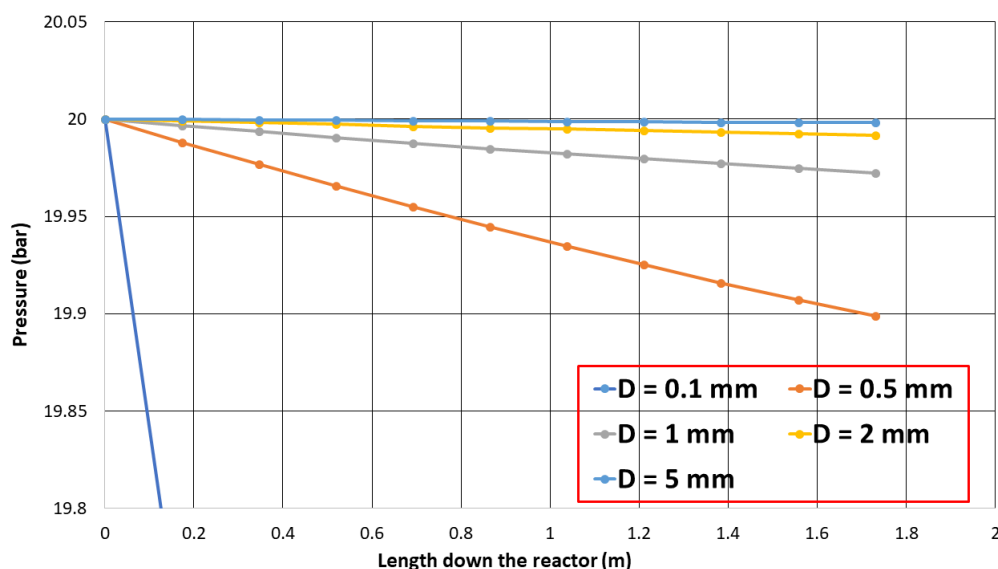


Figure IV.26: Catalyst particle diameter influence on the pressure profile in the reactor for 1.25 kg of catalyst in the base case conditions and a catalytic bed porosity of 30%

It is interesting to notice that the trends observed in the sensitivity studies performed in this work correlate with the one observed by [Meurer and Kern \(2021\)](#). They found similar tendencies concerning the impact of temperature, pressure, inlet molar flow rate and inlet syngas ratio on CO conversion. They also highlight the existence of optimal values for the inlet temperature and syngas ratio which maximise the kerosene fraction (C12-C20). Similarly to this work, their optimal inlet syngas ratio is slightly above 2. However, their optimal temperature is higher than 210°C (around 220°C). The fact that they considered the kerosene fraction to be C8-C16 might explain this difference. The optimal temperature is higher as the higher the temperature, the lower the chain growth probability and thus shorter the products (see Section [IV.2.1](#)). The difference may also come from divergences in the construction of the model; the kinetics model is the same, but the stoichiometry is differently implemented, as explained at the beginning of Chapter [III](#).

Concerning the sensitivity analyses conducted on temperature control and pressure drops, it turns out that they lead to expected results for plug-flow reactors. It is still relevant to investigate these behaviours as it shows that the model correctly reacts as it should. Thus, it demonstrates the proper implementation of energy and momentum balances. Interestingly enough, [Meurer and Kern \(2021\)](#) also identified the reactor temperature as a critical parameter impacting the Fischer-Tropsch product distribution at the reactor outlet.

# Chapter V

## Conclusions and perspectives

The introduction of this work is a bit alarmist about the earth's situation and the climate emergency that we are currently facing. Even if this emergency is evident, there are many reasons to think that the ecological transition has already begun. There are isolated examples, on a country scale, such as in Norway, where 70% of all cars sold in 2020 were electric ones and where diesel vehicles only accounted for 9% of newly registered cars ([Statista, 2022](#)). But some initiatives are also launched on a larger scale. For instance, in September 2021, Climeworks, a Swiss company, has inaugurated the world's largest direct air capture plant in Iceland, which captures 4000 tonnes of CO<sub>2</sub>/year directly from the atmosphere ([Climeworks, 2022](#)). The 2021 Global Status of CCS report showed that there are 135 commercial carbon capture and storage facilities in the world, including 27 fully operational, capturing 40 Mtpa of CO<sub>2</sub>. Once the 135 units are operational, they will capture almost 150 Mtpa of CO<sub>2</sub> ([Global CCS Institute, 2021](#)). These solutions are possible because of a political and scientific increased interest in the energy transition. Then, even though this master thesis does not claim to bring a complete breakthrough in this domain, it is part of all the scientific work that aims at finding and enhancing solutions to reduce the anthropogenic environmental impact and mitigate climate change.

From this perspective, the discussion conducted in this work is about the concept of Power-to-Liquids, a solution to store renewable energy in the medium and long term. The thesis is especially focused on the production of e-kerosene through the low-temperature cobalt-based Fischer-Tropsch synthesis. After a short literature review of the global Power-to-X concept and the Fischer-Tropsch synthesis, the reactor model developed in Aspen Custom Modeler<sup>®</sup> is presented with a particular interest given to the kinetics model. The implementation of material, heat and momentum balances following traditional engineering laws is described. The intricate Fischer-Tropsch product distribution, which follows the Anderson-Schulz-Flory model, is also discussed. The deviation from this ideal model for methane is described by developing the complete stoichiometry of the model. The kinetics model is validated with [Ma et al. \(2014a,b\)](#)'s experimental data to assess its correct utilisation in a whole reactor model, which had not been done previously. The squared correlation coefficients for  $r'_{FT}$  and  $r'_{CH_4}$  are evaluated to 91.0% and 99.6%, respectively.

The analysis of the results yielded by the reactor model shows a significant difference from the results obtained by [Morales and Léonard \(2022\)](#), who implemented a different kinetics model and stoichiometry. It turns out that to reach the same conversion, the model developed in this study yields a reactor volume around 2.5 times greater in the same conditions. A distinct CO consumption rate between both models explains the difference. This feature could result from dissimilarities in the catalyst used in the experiments from which the models were regressed or different assumptions taken to build the models.

The kinetics model developed by [Ma et al. \(2014a,b\)](#) comprises a term translating the positive kinetic effect induced by water on the Fischer-Tropsch reaction. It is explained that the intrinsic form of the model brings some limitations, restricting its application up to a limited conversion value, which depends on the assumptions made to determine it. It is shown that a numerical approach yields a limiting conversion value of 83.5%, while a fully experimental approach leads to a value of 52%.

Finally, some sensitivity studies are conducted. They highlight the presence of optimal temperature and syngas ratio values which optimise the kerosene fraction selectivity. A reactor temperature of 210°C with a syngas ratio slightly above 2 corresponds to an optimal configuration, further confirmed by the literature. These sensitivity analyses also show the importance of appropriate temperature control for the reactor performance, which goes through proper optimisation of the tuning of the cooling system parameters.

As mentioned in the introduction, this master's thesis is part of a project conducted at ULiège, which aims at building a lab-scale Power-to-Liquids process for e-kerosene production. Thus, various perspectives are considered for this project. In the first instance, it is necessary to refine this model to increase its robustness and include vapour-liquid equilibrium calculations to have a model as close as possible to reality. A closer look at the kinetics model validity range should also be given. In this work, the kinetics are validated. It is assumed that it also partly validates the stoichiometry model as errors in this model would result in deviations from experimental data. Validation of the Fischer-Tropsch product distribution could increase the validity of the stoichiometry model.

The next step will probably be the implementation of a third kinetics model, which is more detailed than the one investigated in this work. A possible idea could be the model developed by [Pandey et al. \(2021\)](#) which considers both the methane and ethene deviations from the ideal ASF model. The deactivation mechanisms are also accounted for in the kinetics, especially the oxidation caused by water, neglected in this work. The comparison of the three kinetics models with experimental data obtained in a tubular reactor will help determine the necessary precision extent of the kinetics model and thus the model which best represents reality. On the simulation side, the objective is to transfer the reactor model from Aspen Custom Modeler® to Aspen Plus® to build a whole Power-to-Liquids process model around this reactor. It will include the Fischer-Tropsch reactor, the reverse water-gas shift reactor, which converts CO<sub>2</sub> into CO, the separation and purification units, but also the H<sub>2</sub> generation as well as the CO<sub>2</sub> capture units. On the experimental side, the objective is to set up the lab-scale process to conduct our own experiments to ultimately validate the reactor model.

# Bibliography

- Abelló, S. and Montané, D. (2011), 'Exploring iron-based multifunctional catalysts for Fischer-Tropsch synthesis: A review', *ChemSusChem* **4**, 1538–1556.
- Adeleke, A. A., Liu, X., Lu, X., Moyo, M. and Hildebrandt, D. (2020), 'Cobalt hybrid catalysts in Fischer-Tropsch synthesis', *Reviews in Chemical Engineering* **36**, 437–457.
- Al-Aboosi, F. Y., El-Halwagi, M. M., Moore, M. and Nielsen, R. B. (2021), 'Renewable ammonia as an alternative fuel for the shipping industry', *Current Opinion in Chemical Engineering* **31**, 100670.
- Alshafei, F. H., Park, Y., Zones, S. I. and Davis, M. E. (2021), 'Methanol-to-olefins catalysis on ERI-type molecular sieves: towards enhancing ethylene selectivity', *Journal of Catalysis* **404**, 620–633.
- Aspen Technology Inc (2022), 'aspenONE® Product Portfolio'. Accessed on 28 April 2022.  
URL: <https://www.aspentech.com/en/products/full-product-listing>
- Barrios, A. J., Gu, B., Luo, Y., Peron, D. V., Chernavskii, P. A., Virginie, M., Wojcieszak, R., Thybaut, J. W., Ordonsky, V. V. and Khodakov, A. Y. (2020), 'Identification of efficient promoters and selectivity trends in high temperature Fischer-Tropsch synthesis over supported iron catalysts', *Applied Catalysis B: Environmental* **273**.
- Bertole, C. J., Mims, C. A. and Kiss, G. (2002), 'The effect of water on the cobalt-catalyzed Fischer-Tropsch synthesis', *Journal of Catalysis* **210**, 84–96.
- Boda, M. A., Deshetti, S. S. and Gavade, M. A. (2017), 'Design and Development of Parallel-Counter Flow Heat Exchanger', *S. S. Deshetti International Journal of Innovative Research in Advanced Engineering (IJIRAE)* **4**.
- Borg, O., Eri, S., Blekkan, E. A., Storsæter, S., Wigum, H., Rytter, E. and Holmen, A. (2007), 'Fischer-Tropsch synthesis over  $\gamma$ -alumina-supported cobalt catalysts: Effect of support variables', *Journal of Catalysis* **248**, 89–100.
- Botes, F. G., Dyk, B. V. and McGregor, C. (2009), 'The development of a macro kinetic model for a commercial Co/Pt/Al<sub>2</sub>O<sub>3</sub> Fischer-Tropsch catalyst', *Industrial and Engineering Chemistry Research* **48**, 10439–10447.
- Buffo, G., Marocco, P., Ferrero, D., Lanzini, A. and Santarelli, M. (2019), *Power-to-X and power-to-power routes*, Elsevier, pp. 529–557.
- Carnall, A., Gibbs, A., Calderwood, L. U., Coupland, S., Dupslaff, M., Heid, B., Lash, N., Li, L., Riedel, R., Riefer, D., Steinbach, J. and Watzinger, A. (2022), *Clean Skies for Tomorrow: Delivering on the Global Power-to-Liquid Ambition*, Technical report, World Economic Forum in partnership with McKinsey & Company.

- Cheng, K., Virginie, M., Ordonsky, V. V., Cordier, C., Chernavskii, P. A., Ivantsov, M. I., Paul, S., Wang, Y. and Khodakov, A. Y. (2015), 'Pore size effects in higher temperature Fischer-Tropsch synthesis over supported iron catalysts', *Journal of Catalysis* **328**, 139–150.
- Clarion Energy Content Directors (2021), 'INEOS, ENGIE launch hydrogen pilot project in Belgium', POWER Engineering. Accessed on 06 June 2022.  
**URL:** <https://www.power-eng.com/gas/ineos-engie-launch-hydrogen-pilot-project-in-belgium/#gref>
- Climate.gov (2021a), 'Climate Change: Mountain glaciers'. Accessed on 21 May 2022.  
**URL:** <https://www.climate.gov/news-features/understanding-climate/climate-change-glacier-mass-balance>
- Climate.gov (2021b), 'Climate Change: Atmospheric Carbon Dioxide'. Accessed on 21 May 2022.  
**URL:** <https://www.climate.gov/news-features/understanding-climate/climate-change-atmospheric-carbon-dioxide#:~:text=Based%20on%20preliminary%20analysis%2C%20the,to%20the%20COVID%2D19%20pandemic.>
- Climate.gov (2022), 'Climate Change: Global Temperature'. Accessed on 21 May 2022.  
**URL:** <https://www.climate.gov/news-features/understanding-climate/climate-change-global-temperature>
- Climeworks (2022), 'Orca: the first large-scale plant'. Accessed on 24 May 2022.  
**URL:** <https://climeworks.com/roadmap/orca>
- Dalai, A. K. and Davis, B. H. (2008), 'Fischer-Tropsch synthesis: A review of water effects on the performances of unsupported and supported Co catalysts', *Applied Catalysis A: General* **348**, 1–15.
- Davidson, C., Neues, E., Schwab, A. and Vimmerstedt, L. (2014), An overview of aviation fuel markets for biofuels stakeholders, Technical report, National Renewable Energy Laboratory (NREL).
- de Klerk, A. (2012), *Fischer-Tropsch Refining*, Wiley.
- Delhez, E. J. M. (2017), *Séries classiques et sommation de séries*, version 2017-2018 edn, Faculté des Sciences Appliquées (ULiège).
- Dieterich, V., Buttler, A., Hanel, A., Spliethoff, H. and Fendt, S. (2020), 'Power-to-liquid via synthesis of methanol, DME or Fischer-Tropsch-fuels: a review', *Energy and Environmental Science* **13**, 3207–3252.
- Doliente, S. S., Narayan, A., Tapia, J. F. D., Samsatli, N. J., Zhao, Y. and Samsatli, S. (2020), 'Bio-aviation Fuel: A Comprehensive Review and Analysis of the Supply Chain Components', *Frontiers in Energy Research* **8**.
- Dry, M. E. (2002), 'High quality diesel via the Fischer-Tropsch process - A review', *Journal of Chemical Technology and Biotechnology* **77**, 43–50.
- Duratherm Extended Life Fluids (2022), 'Heat Transfer Coefficient Calculator'. Accessed on 19 May 2022.  
**URL:** <https://durathermfluids.com/resources/calculators/heat-transfer-coefficient/>

- ENGIE (2022), 'Engie et Infinium annoncent un partenariat pour développer un hib industriel d'envergure européenne de production de carburants de synthèse à Dunkerque'. Accessed on 06 June 2022.  
**URL:** <https://www.laborelec.com/columbus-project-engie-carmeuse-cockerill-reduction-of-co2-emissions-in-wallonia/>
- ENGIE Laborelec (2022), 'Columbus Project'. Accessed on 06 June 2022.  
**URL:** <https://www.laborelec.com/columbus-project-engie-carmeuse-cockerill-reduction-of-co2-emissions-in-wallonia/>
- Eos (2022), 'Australian Wildfires Linked to Ozone Layer Depletion'. Accessed on 21 May 2022.  
**URL:** <https://eos.org/articles/australian-wildfires-linked-to-ozone-layer-depletion>
- Ermolaev, V. S., Gryaznov, K. O., Mitberg, E. B., Mordkovich, V. Z. and Tretyakov, V. F. (2015), 'Laboratory and pilot plant fixed-bed reactors for Fischer-Tropsch synthesis: Mathematical modeling and experimental investigation', *Chemical Engineering Science* **138**, 1–8.
- European Environment Agency (EEA) (2021), 'Global and European sea level rise'. Accessed on 21 May 2022.  
**URL:** <https://www.climate.gov/news-features/understanding-climate/climate-change-global-temperature>
- Eurostat (2022), 'Oil and petroleum products - a statistical overview'. Accessed on 28 May 2022.  
**URL:** [https://ec.europa.eu/eurostat/statistics-explained/index.php?title=Oil\\_and\\_petroleum\\_products\\_-\\_a\\_statistical\\_overview&oldid=315177#Trade\\_in\\_petroleum\\_products](https://ec.europa.eu/eurostat/statistics-explained/index.php?title=Oil_and_petroleum_products_-_a_statistical_overview&oldid=315177#Trade_in_petroleum_products)
- Fischer, F. and Tropsch, H. (1923), 'The preparation of synthetic oil mixtures (synthol) from carbon monoxide and hydrogen', *Brennstoff-Chem* **4**, 276–285.
- Flory, P. J. (1936), 'Molecular Size Distribution in Linear Condensation Polymers', *Journal of the American Chemical Society* **58**, 1877–1885.
- Fogler, H. S. (2016), *Elements of Chemical Reaction Engineering*, Fifth Edition edn, Pearson Education, Inc.
- Foit, S. R., Vinke, I. C., de Haart, L. G. J. and Eichel, R.-A. (2017), 'Power-to-Syngas - eine Schlüsseltechnologie für die Umstellung des Energiesystems?', *Angewandte Chemie* **129**, 5488–5498.
- Förtsch, D., Pabst, K. and Groß-Hardt, E. (2015), 'The product distribution in Fischer-Tropsch synthesis: An extension of the ASF model to describe common deviations', *Chemical Engineering Science* **138**, 333–346.
- Ghaib, K. and Ben-Fares, F. Z. (2018), 'Power-to-Methane: A state-of-the-art review', *Renewable and Sustainable Energy Reviews* **81**, 433–446.
- Gholami, Z., Tišler, Z. and Rubáš, V. (2021), 'Recent advances in Fischer-Tropsch synthesis using cobalt-based catalysts: a review on supports, promoters, and reactors', *Catalysis Reviews - Science and Engineering* **63**, 512–595.
- Global CCS Institute (2021), CCS accelerating to net zero, in 'Global Status of CCS 2021'.



- Gross, S. (2020), The Challenge of Decarbonizing Heavy Transport, Technical report, Foreign Policy.
- Guettel, R., Kunz, U. and Turek, T. (2008), 'Reactors for Fischer-Tropsch synthesis', *Chemical Engineering and Technology* **31**, 746–754.
- Harrington, T. (2022), 'International partnership to produce e-kerosene using CO<sub>2</sub> extracted from cement production', GREENAIR. Accessed on 29 May 2022.  
URL: <https://www.greenairnews.com/?p=2889>
- Hillestad, M. (2015), 'Modeling the Fischer-Tropsch Product Distribution and Model Implementation', *Chemical Product and Process Modeling* **10**, 147–159.
- Hodala, J. L., Moon, D. J., Reddy, K. R., Reddy, C. V., Kumar, T. N., Ahamed, M. I. and Raghu, A. V. (2021), 'Catalyst design for maximizing C5+ yields during Fischer-Tropsch synthesis', *International Journal of Hydrogen Energy* **46**, 3289–3301.
- Hu, G., Chen, C., Lu, H. T., Wu, Y., Liu, C., Tao, L., Men, Y., He, G. and Li, K. G. (2020), 'A Review of Technical Advances, Barriers, and Solutions in the Power to Hydrogen (P2H) Roadmap', *Engineering* **6**, 1364–1380.
- Huff, G. A. and Satterfield, C. (1984), 'Evidence for Two Chain Growth Probabilities on Iron Catalysts in the Fischer-Tropsch Synthesis', *Journal of Catalysis* **85**, 370–379.
- Iglesia, E., Reyes, S. C., Madon, R. J. and Soled, S. L. (1993), 'Selectivity Control and Catalyst Design in the Fischer-Tropsch Synthesis: Sites, Pellets, and Reactors', *Advances in Catalysis* **39**.
- Iglesia, E., Soled, S. L. and Fiato, R. A. (1992), 'Fischer-Tropsch synthesis on cobalt and ruthenium. Metal dispersion and support effects on reaction rate and selectivity', *Journal of Catalysis* **137**, 212–224.
- Ikäheimo, J., Kiviluoma, J., Weiss, R. and Holttinen, H. (2018), 'Power-to-ammonia in future North European 100 % renewable power and heat system', *International Journal of Hydrogen Energy* **43**, 17295–17308.
- Ince, A. C., Colpan, C. O., Hagen, A. and Serincan, M. F. (2021), 'Modeling and simulation of Power-to-X systems: A review', *Fuel* **304**.
- IPCC (2022), Climate Change 2022: Mitigation of Climate Change, Technical report, World Meteorological Organization (WMO) & UN Environment Programme (UNEP).
- Jacobs, G., Das, T. K., Zhang, Y., Li, J., Racoillet, G. and Davis, B. H. (2002), 'Fischer-Tropsch synthesis: support, loading, and promoter effects on the reducibility of cobalt catalysts', *Applied Catalysis A: General* **233**, 263–281.
- Jancovici, J.-M. (2007), 'Quels sont les gaz à effet de serre'. Accessed on 21 May 2022.  
URL: <https://jancovici.com/changement-climatique/gaz-a-effet-de-serre-et-cycle-du-carbone/quels-sont-les-gaz-a-effet-de-serre-quels-sont-leurs-contribution-a-leffet-de-serre/>
- Jess, A. and Kern, C. (2009), 'Modeling of multi-tubular reactors for Fischer-Tropsch synthesis', *Chemical Engineering and Technology* **32**, 1164–1175.

- Kallio, P., Pásztor, A., Akhtar, M. K. and Jones, P. R. (2014), 'Renewable jet fuel', *Current Opinion in Biotechnology* **26**, 50–55.
- Kaskes, B., Vervloet, D., Kapteijn, F. and van Ommen, J. R. (2016), 'Numerical optimization of a structured tubular reactor for Fischer-Tropsch synthesis', *Chemical Engineering Journal* **283**, 1465–1483.
- KEROGREEN (2022), 'Sustainable & green aviation fuel production'. Accessed on 29 May 2022.  
URL: <https://www.kerogreen.eu/index.php>
- Khalighi, R., Bahadoran, F., Panjeshahi, M. H., Zamaniyan, A. and Tahouni, N. (2020), 'Effects of Nickel Aluminate Spinel ( $\text{NiAl}_2\text{O}_4$ ) as Catalyst Support and Promoters (Ru, Rh) in Fischer-Tropsch Synthesis', *ChemistrySelect* **5**, 7934–7940.
- Knutsen, K. T. (2013), Modelling and optimization of a Gas-to-Liquid plant, Master's thesis, NTNU - Trondheim.
- Koj, J. C., Wulf, C. and Zapp, P. (2019), 'Environmental impacts of power-to-X systems - A review of technological and methodological choices in Life Cycle Assessments', *Renewable and Sustainable Energy Reviews* **112**, 865–879.
- Korberg, A. D., Mathiesen, B. V., Clausen, L. R. and Skov, I. R. (2021), 'The role of biomass gasification in low-carbon energy and transport systems', *Smart Energy* **1**, 100006.
- Küngas, R. (2020), 'Review-Electrochemical  $\text{CO}_2$  Reduction for CO Production: Comparison of Low- and High-Temperature Electrolysis Technologies', *Journal of The Electrochemical Society* **167**(4), 044508.
- Laan, G. P. V. D. and Beenackers, A. A. (1999), 'Kinetics and Selectivity of the Fischer-Tropsch Synthesis: A Literature Review', *Catalysis Reviews - Science and Engineering* **41**, 255–318.
- Lam, N. L., Smith, K. R., Gauthier, A. and Bates, M. N. (2012), 'Kerosene: A review of household uses and their hazards in low-and middle-income countries', *Journal of Toxicology and Environmental Health - Part B: Critical Reviews* **15**, 396–432.
- Le Monde (2021), 'Les inondations de juillet en Allemagne et en Belgique sont bien liées au réchauffement climatique'. Accessed on 20 May 2022.  
URL: [https://www.lemonde.fr/planete/article/2021/08/24/les-inondations-de-juillet-en-allemande-et-en-belgique-sont-bien-liees-au-rechauffement-climatique\\_6092170\\_3244.html#:~:text=Terre%20d'inspiration-,Les%20inondations%20de%20juillet%20en%20Allemagne%20et%20en%20Belgique%20sont,de%20recherche%20dans%20le%20monde.](https://www.lemonde.fr/planete/article/2021/08/24/les-inondations-de-juillet-en-allemande-et-en-belgique-sont-bien-liees-au-rechauffement-climatique_6092170_3244.html#:~:text=Terre%20d'inspiration-,Les%20inondations%20de%20juillet%20en%20Allemagne%20et%20en%20Belgique%20sont,de%20recherche%20dans%20le%20monde.)
- Le Temps (2022), 'L'Ethiopie frappée par la "pire sécheresse jamais vécue"'. Accessed on 20 May 2022.  
URL: <https://www.letemps.ch/monde/lethiopie-frappee-pire-secheresse-jamais-vecue>
- Lee, A. (2020), 'Chemicals giant that runs 'world's most polluting plant' wants to buy wind and solar', RECHARGE. Accessed on 04 June 2022.  
URL: <https://www.rechargenews.com/transition/chemicals-giant-that->

[runs-worlds-most-polluting-plant-wants-to-buy-wind-and-solar/2-1-809308](#)

- Li, T., Wang, H., Yang, Y., Xiang, H. and Li, Y. (2014), 'Study on an iron-nickel bimetallic Fischer-Tropsch synthesis catalyst', *Fuel Processing Technology* **118**, 117–124.
- Liu, G., Yan, B. and Chen, G. (2013), 'Technical review on jet fuel production', *Renewable and Sustainable Energy Reviews* **25**, 59–70.
- Lualdi, M., Lögdberg, S., Regali, F., Boutonnet, M. and Järås, S. (2011), 'Investigation of mixtures of a Co-based catalyst and a Cu-based catalyst for the Fischer-Tropsch synthesis with Bio-Syngas: The importance of indigenous water', *Topics in Catalysis* **54**, 977–985.
- Léonard, G. (2021a), La capture et le stockage du CO<sub>2</sub>, in 'Gestion durable des combustibles : approvisionnement, synthèse et utilisation', Département du Chemical Engineering - ULiège, pp. 90–100.
- Léonard, G. (2021b), Les e-fuels et la réutilisation du CO<sub>2</sub>, in 'Gestion durable des combustibles : approvisionnement, synthèse et utilisation', Département du Chemical Engineering - ULiège, pp. 1–94.
- Lögdberg, S., Boutonnet, M., Walmsley, J. C., Järås, S., Holmen, A. and Blekkan, E. A. (2011), 'Effect of water on the space-time yield of different supported cobalt catalysts during Fischer-Tropsch synthesis', *Applied Catalysis A: General* **393**, 109–121.
- Ma, W., Ding, Y. J. and Lin, L. W. (2004), 'Fischer-Tropsch Synthesis over Activated-Carbon-Supported Cobalt Catalysts: Effect of Co Loading and Promoters on Catalyst Performance', *Industrial and Engineering Chemistry Research* **43**, 2391–2398.
- Ma, W., Jacobs, G., Das, T. K., Masuku, C. M., Kang, J., Pendyala, V. R. R., Davis, B. H., Klettlinger, J. L. and Yen, C. H. (2014b), 'Fischer-Tropsch synthesis: Kinetics and water effect on methane formation over 25%Co/ $\gamma$ -Al<sub>2</sub>O<sub>3</sub> catalyst', *Industrial and Engineering Chemistry Research* **53**, 2157–2166.
- Ma, W., Jacobs, G., Sparks, D. E., Gnanamani, M. K., Pendyala, V. R. R., Yen, C. H., Klettlinger, J. L., Tomsik, T. M. and Davis, B. H. (2011), 'Fischer-Tropsch synthesis: Support and cobalt cluster size effects on kinetics over Co/Al<sub>2</sub>O<sub>3</sub> and Co/SiO<sub>2</sub> catalysts', *Fuel* **90**, 756–765.
- Ma, W., Jacobs, G., Sparks, D. E., Spicer, R. L., Davis, B. H., Klettlinger, J. L. and Yen, C. H. (2014a), 'Fischer-Tropsch synthesis: Kinetics and water effect study over 25%Co/Al<sub>2</sub>O<sub>3</sub> catalysts', *Catalysis Today* **228**, 158–166.
- Mahmoudi, H., Mahmoudi, M., Doustdar, O., Jahangiri, H., Tsolakis, A., Gu, S. and LechWyszynski, M. (2018), 'A review of Fischer-Tropsch synthesis process, mechanism, surface chemistry and catalyst formulation', *Biofuels Engineering* **2**, 11–31.
- Meurer, A. and Kern, J. (2021), 'Fischer-Tropsch synthesis as the key for decentralized sustainable kerosene production', *Energies* **14**.
- Morales, A. and Léonard, G. (2022), Simulation of a Fischer-Tropsch reactor for jet fuel production using Aspen Custom Modeler. Accepted for publication in Computer Aided Chemical Engineering.

- Mousavi, S., Zamaniyan, A., Irani, M. and Rashidzadeh, M. (2015), 'Generalized kinetic model for iron and cobalt based Fischer-Tropsch synthesis catalysts: Review and model evaluation', *Applied Catalysis A: General* **506**, 57–66.
- Ng, K. S., Farooq, D. and Yang, A. (2021), 'Global biorenewable development strategies for sustainable aviation fuel production', *Renewable and Sustainable Energy Reviews* **150**, 111502.
- Oberg, S., Odenberger, M. and Johnsson, F. (2022), 'Exploring the competitiveness of hydrogen-fueled gas turbines in future energy systems', *International Journal of Hydrogen Energy* **47**(1), 624–644.
- Okoye-Chine, C. G., Moyo, M., Liu, X. and Hildebrandt, D. (2019), 'A critical review of the impact of water on cobalt-based catalysts in Fischer-Tropsch synthesis', *Fuel Processing Technology* **192**, 105–129.
- Olbert, G., Corr, P. F., Reuter, L. and Wambach, U. (2007), Multi-tube fixed-bed reactor, especially for catalytic gas phase reactions, Technical report, US 7,226,567 B1.
- Orban, F., Léonard, G. and Yonekura, Y. (2021), BELGIUM'S NEXT CENTURY SAF / E-FUEL ECOSYSTEM, in 'Neutral Kero Lime Presentation to Energia'.
- Pallardy, R. (2022), 'IPCC Report Analysis: The Top Five Measures to Halve Emissions by 2030', NESTE. Accessed on 21 May 2022.  
**URL:** [https://journeytozerostories.neste.com/sustainability/ipcc-report-analysis-top-five-measures-halve-emissions-2030?gclid=Cj0KCQjwm6KUBhC3ARIsACIwxBgt\\_VRAFKDL905Osa0v28JWvkbyI4U7QQakI4Tjbl870bp9rvFvCiYaAgsAEALw\\_wcB](https://journeytozerostories.neste.com/sustainability/ipcc-report-analysis-top-five-measures-halve-emissions-2030?gclid=Cj0KCQjwm6KUBhC3ARIsACIwxBgt_VRAFKDL905Osa0v28JWvkbyI4U7QQakI4Tjbl870bp9rvFvCiYaAgsAEALw_wcB)
- Panahi, M., Rafiee, A., Skogestad, S. and Hillestad, M. (2012), 'A natural gas to liquids process model for optimal operation', *Industrial and Engineering Chemistry Research* **51**, 425–433.
- Panahi, M., Skogestad, S. and Yelchuru, R. (2010), 'Steady State Simulation for Optimal Design and operation of a GTL Process'.
- Pandey, U., Runnigen, A., Gavrilović, L., Jørgensen, E. A., Putta, K. R., Rout, K. R., Rytter, E., Blekkan, E. A. and Hillestad, M. (2021), 'Modeling Fischer-Tropsch kinetics and product distribution over a cobalt catalyst', *AIChE Journal* **67**.
- Panzone, C., Philippe, R., Chappaz, A., Fongarland, P. and Bengaouer, A. (2020), 'Power-to-Liquid catalytic CO<sub>2</sub> valorization into fuels and chemicals: Focus on the Fischer-Tropsch route', *Journal of CO<sub>2</sub> Utilization* **38**, 314–347.
- Peters, R., Wegener, N., Samsun, R. C., Schorn, F., Riese, J., Grünwald, M. and Stolten, D. (2022), 'A Techno-Economic Assessment of Fischer-Tropsch Fuels Based on Syngas from Co-Electrolysis', *Processes* **10**(4).
- Pour, A. N. and Housaindokht, M. R. (2013), 'The olefin to paraffin ratio as a function of catalyst particle size in Fischer-Tropsch synthesis by iron catalyst', *Journal of Natural Gas Science and Engineering* **14**, 204–210.
- Ritchie, H., Roser, M. and Rosado, P. (2020), 'CO<sub>2</sub> and Greenhouse Gas Emissions', Our World in Data. Accessed on 21 May 2022.  
**URL:** <https://ourworldindata.org/emissions-by-sector>

- RTBF (2021), ‘Vague de froid au Brésil: jusqu’à moins 10 degrés sous zéro, des sans-abri meurent et les plantations de café souffrent du gel’. Accessed on 21 May 2022.  
**URL:** <https://www.rtbef.be/article/vague-de-froid-au-bresil-jusqua-moins-10-degres-sous-zero-des-sans-abri-meurent-et-les-plantations-de-cafe-souffrent-du-gel-10815469>
- Rytter, E., Yang, J., Øyvind Borg and Holmen, A. (2020), ‘Significance of C3 olefin to paraffin ratio in cobalt Fischer–Tropsch synthesis’, *Catalysts* **10**.
- Sasol (2022), ‘Gas-to-Liquids technology’. Accessed on 23 May 2022.  
**URL:** <https://www.sasol.com/innovation/gas-liquids/technology#parent>
- Schwab, E., Milanov, A., Schunk, S. A., Behrens, A. and Schödel, N. (2015), ‘Dry reforming and reverse water gas shift: Alternatives for syngas production?’, *Chemie-Ingenieur-Technik* **87**, 347–353.
- Semmel, M., Ali, R. E., Ouda, M., Schaadt, A., Sauer, J. and Hebling, C. (2021), *Power-to-DME: a cornerstone towards a sustainable energy system*, Elsevier, pp. 123–151.
- Shafer, W. D., Gnanamani, M. K., Graham, U. M., Yang, J., Masuku, C. M., Jacobs, G. and Davis, B. H. (2019), ‘Fischer-Tropsch: Product selectivity-the fingerprint of synthetic fuels’, *Catalysts* **9**.
- Shell (2022), ‘Gas-to-Liquids’. Accessed on 23 May 2022.  
**URL:** <https://www.shell.com/energy-and-innovation/natural-gas/gas-to-liquids.html>
- Shepherd, J. E., Nuyt, C. D., Lee, J. J. and Woodrow, J. E. (2000), Flash Point and Chemical Composition of Aviation Kerosene (Jet A), Technical report, California Institute of Technology.
- Sie, S. T. and Krishna, R. (1999), ‘Fundamentals and selection of advanced Fischer-Tropsch reactors’, *Applied Catalysis A: General* **186**, 55–70.
- Smit, E. D. and Weckhuysen, B. M. (2008), ‘The renaissance of iron-based Fischer-Tropsch synthesis: On the multifaceted catalyst deactivation behaviour’, *Chemical Society Reviews* **37**, 2758–2781.
- Smith, B. L. and Bruno, T. J. (2007), ‘Composition-explicit distillation curves of aviation fuel JP-8 and a coal-based jet fuel’, *Energy and Fuels* **21**, 2853–2862.
- Sonal, Pant, K. K. and Upadhyayula, S. (2020), ‘An insight into the promotional effect on Fe-Co bimetallic catalyst in the Fischer-Tropsch reaction: A DRIFTS study’, *Fuel* **276**.
- Soone, J. (2020), Sustainable aviation fuels, Technical report, European Parliamentary Research Service (EPRS).
- Statista (2022), ‘Number of electric cars and plug-in hybrids in Norway from 2012 to 2020’. Accessed on 24 May 2022.  
**URL:** <https://www.statista.com/statistics/696187/electric-and-hybrid-cars-number-in-norway/>
- Stenger, H. . . and Askonas, C. F. (1986), ‘Thermodynamic Product Distributions for the Fischer-Tropsch Synthesis’, *Ind. Eng. Chem. Fundam* **25**, 410–413.

- Steynberg, A., Espinoza, R., Jager, B. and Vosloo, A. (1999), 'High temperature Fischer–Tropsch synthesis in commercial practice', *Applied Catalysis A: General* **186**(1), 41–54.
- Steynberg, A. P., Dry, M. E., Davis, B. H. and Breman, B. B. (2004), 'Fischer-Tropsch reactors', *Studies in Surface Science and Catalysis* **152**, 64–195.
- Storsæter, S., Borg, Blekkan, E. A. and Holmen, A. (2005), 'Study of the effect of water on Fischer-Tropsch synthesis over supported cobalt catalysts', *Journal of Catalysis* **231**, 405–419.
- Sun, B., Xu, K., Nguyen, L., Qiao, M. and Tao, F. F. (2012), 'Preparation and Catalysis of Carbon-Supported Iron Catalysts for Fischer-Tropsch Synthesis', *ChemCatChem* **4**, 1498–1511.
- Synkero (2022), 'Futureproof aviation'. Accessed on 29 May 2022.  
URL: <https://synkero.com/>
- Teimouri, Z., Abatzoglou, N. and Dalai, A. K. (2021), 'Kinetics and selectivity study of Fischer-Tropsch synthesis to C5+ hydrocarbons: A review', *Catalysts* **11**, 1–32.
- Todic, B., Ma, W., Jacobs, G., Nikacevic, N., Davis, B. H. and Bukur, D. B. (2017), 'Kinetic Modeling of Secondary Methane Formation and 1-Olefin Hydrogenation in Fischer–Tropsch Synthesis over a Cobalt Catalyst', *International Journal of Chemical Kinetics* **49**, 859–874.
- Tsakoumis, N. E., Rønning, M., Øyvind Borg, Rytter, E. and Holmen, A. (2010), 'Deactivation of cobalt based Fischer-Tropsch catalysts: A review', *Catalysis Today* **154**, 162–182.
- Unicef (2020), 'Catastrophes naturelles: le lot quotidien des pays d'Asie du sud?'. Accessed on 20 May 2022.  
URL: <https://www.unicef.fr/article/catastrophes-naturelles-le-lot-quotidien-des-pays-d-asie-du-sud#:~:text=Certaines%20communaut%C3%A9s%20aux%20Philippines%20commencent,r%C3%A9gions%20les%20plus%20fortement%20affect%C3%A9es.>
- van Dyk, J., Keyser, M. and Coertzen, M. (2006), 'Syngas production from South African coal sources using Sasol–Lurgi gasifiers', *International Journal of Coal Geology* **65**(3), 243–253. Hydrogen from Coal.
- van Helden, P., Prinsloo, F., van den Berg, J. A., Xaba, B., Erasmus, W., Claeys, M. and van de Loosdrecht, J. (2020), 'Cobalt-nickel bimetallic Fischer-Tropsch catalysts: A combined theoretical and experimental approach', *Catalysis Today* **342**, 88–98.
- Vervloet, D., Kapteijn, F., Nijenhuis, J. and Ommen, J. R. V. (2012), 'Fischer-Tropsch reaction-diffusion in a cobalt catalyst particle: Aspects of activity and selectivity for a variable chain growth probability', *Catalysis Science and Technology* **2**, 1221–1233.
- Visconti, C. G., Tronconi, E., Lietti, L., Forzatti, P., Rossini, S. and Zennaro, R. (2011), 'Detailed kinetics of the Fischer-Tropsch synthesis on cobalt catalysts based on H-assisted CO activation', *Topics in Catalysis* **54**, 786–800.
- Wang, W.-C., Liu, Y.-C. and Nugroho, R. A. A. (2022), 'Techno-economic analysis of renewable jet fuel production: The comparison between Fischer-Tropsch synthesis and pyrolysis', *Energy* **239**, 121970.



- Wehenkel, L. (2019), Introduction - Analyse de données exploratoire, in 'Eléments de statistique', Département d'Electricité, Electronique et Informatique - ULiège, p. 37.
- Wilson, A. (2021), Revision of the Renewable Energy Directive: Fit for 55 package, Technical report, European Parliamentary Research Service (EPRS).
- Xu, X., Liu, E., Zhu, N., Liu, F. and Qian, F. (2022), 'Review of the Current Status of Ammonia-Blended Hydrogen Fuel Engine Development', *Energies* **15**(3).
- Yang, J., Qi, Y., Zhu, J., Zhu, Y. A., Chen, D. and Holmen, A. (2013), 'Reaction mechanism of CO activation and methane formation on Co Fischer-Tropsch catalyst: A combined DFT, transient, and steady-state kinetic modeling', *Journal of Catalysis* **308**, 37–49.
- Yang, M., Fan, D., Wei, Y., Tian, P. and Liu, Z. (2019), 'Recent Progress in Methanol-to-Olefins (MTO) Catalysts', *Advanced Materials* **31**.
- Yao, G., Staples, M. D., Malina, R. and Tyner, W. E. (2017), 'Stochastic techno-economic analysis of alcohol-to-jet fuel production', *Biotechnology for Biofuels* **10**.
- Yates, I. C. and Satterfield, C. N. (1991), 'Intrinsic Kinetics of the Fischer-Tropsch Synthesis on a Cobalt Catalyst', *Energy & Fuels* **5**, 168–173.
- You, F. and Wang, B. (2011), 'Life cycle optimization of biomass-to-liquid supply chains with distributed-centralized processing networks', *Industrial and Engineering Chemistry Research* **50**, 10102–10127.
- Zhang, Q., Kang, J. and Wang, Y. (2010), 'Development of Novel Catalysts for Fischer-Tropsch Synthesis: Tuning the Product Selectivity', *ChemCatChem* **2**, 1030–1058.
- Zhong, J., Han, J., Wei, Y. and Liu, Z. (2021), 'Catalysts and shape selective catalysis in the methanol-to-olefin (MTO) reaction', *Journal of Catalysis* **396**, 23–31.



# Appendix A

## Energy balance full derivation

In Section III.5.2 the following equation is obtained:

$$\left(\sum_i \dot{F}_i \cdot h_i\right)(x) - \left(\sum_i \dot{F}_i \cdot h_i\right)(x + \Delta x) = U \cdot \pi \cdot D \cdot \Delta x \cdot (T - T_c) \quad (\text{A.1})$$

According to the derivative definition, already used in III.5.1, it can be transformed in:

$$\frac{d\left(\sum_i \dot{F}_i \cdot h_i\right)}{dx} = -U \cdot \pi \cdot D \cdot (T - T_c) \quad (\text{A.2})$$

The molar enthalpy of component  $i$  can be developed as:

$$h_i(T) = h_i^0(T_r) + \int_{T_r}^T C_{P,i} dT \quad (\text{A.3})$$

where  $h_i^0(T_r)$  corresponds to a reference enthalpy at the reference temperature  $T_r$  and where the second term thus describes the enthalpy variation between this temperature  $T_r$  and the considered temperature  $T$ . It is assumed that there are no phase changes for this development. Another assumption taken is that the heat capacity is independent of the temperature, which leads to:

$$h_i(T) = h_i^0(T_r) + C_{P,i} \cdot (T - T_r) \quad (\text{A.4})$$

With that in mind and with the results found for the material balance in Section III.5.1, the left-hand side of Equation A.2 can be developed:

$$\frac{d\left(\sum_i \dot{F}_i \cdot h_i\right)}{dx} = \sum_i \dot{F}_i \cdot \frac{dh_i}{dT} + \sum_i h_i \cdot \frac{d\dot{F}_i}{dx} = \sum_i \dot{F}_i \cdot C_{P,i} \cdot \frac{dT}{dx} + \sum_i h_i \cdot A \cdot \rho_b \cdot r'_i \quad (\text{A.5})$$

The first term of this last equality gives:

$$\sum_i \dot{F}_i \cdot C_{P,i} \cdot \frac{dT}{dx} = \sum_i x_i \cdot \dot{F} \cdot C_{P,i} \cdot \frac{dT}{dx} = \dot{F} \sum_i x_i \cdot C_{P,i} \cdot \frac{dT}{dx} = \dot{F} \cdot C_P \cdot \frac{dT}{dx} \quad (\text{A.6})$$

where  $x_i$  is the molar fraction of component  $i$ ,  $\dot{F}$  represents the total molar flow rate of the stream and  $C_P$  its overall molar heat capacity. The second term of the last equality in Equation A.5 develops as:

$$\sum_i h_i \cdot A \cdot \rho_b \cdot r'_i = A \cdot \rho_b \cdot \sum_i h_i \cdot (\nu_{i,1} \cdot r'_1 + \nu_{i,2} \cdot r'_2) = A \cdot \rho_b \cdot \left( \sum_i h_i \cdot \nu_{i,1} \cdot r'_1 + \sum_i h_i \cdot \nu_{i,2} \cdot r'_2 \right) \quad (\text{A.7})$$

where  $r'_1$  and  $r'_2$  are the two reaction rates described in Section III.4 and where  $\nu_{i,1}$  and  $\nu_{i,2}$  represent the stoichiometric coefficients of component  $i$  in the corresponding reaction. The two sums present in parentheses are by definition (see Section III.5.2) the heat of reactions 1 and 2 leading to:

$$A \cdot \rho_b \cdot (\Delta H_{R,1} \cdot r'_1 + \Delta H_{R,2} \cdot r'_2) \quad (\text{A.8})$$

Injecting these results in the energy balance equation leads to:

$$\dot{F} \cdot C_P \cdot \frac{dT}{dx} + A \cdot \rho_b \cdot (\Delta H_{R,1} \cdot r'_1 + \Delta H_{R,2} \cdot r'_2) = -U \cdot \pi \cdot D \cdot (T - T_c) \quad (\text{A.9})$$

and rearranging the terms:

$$\frac{dT}{dx} = \frac{(-\Delta H_{R,1} \cdot r'_1 - \Delta H_{R,2} \cdot r'_2) \cdot A \cdot \rho_b - U \cdot \pi \cdot D \cdot (T - T_c)}{\dot{F} \cdot C_P} \quad (\text{A.10})$$

which is equivalent to Equation III.71 presented in Section III.5.2.

Regarding the balance on the cooling medium, the following balance is derived in Section III.5.2:

$$-\dot{F}_c \cdot h_c(x) + \dot{F}_c \cdot h_c(x + \Delta x) + \Delta \dot{Q} = 0 \quad (\text{A.11})$$

Using the developed expression for  $\Delta \dot{Q}$  (see Equation III.69) and the derivative definition, it results in:

$$\frac{d(\dot{F}_c \cdot h_c)}{dx} = -U \cdot \pi \cdot D \cdot (T - T_c) \quad (\text{A.12})$$

The coolant molar enthalpy can be derived as it is performed for the balance on the reaction medium (see Equation A.4):

$$h_c(T) = h_c^0(T_r) + C_{P,c} \cdot (T_c - T_r) \quad (\text{A.13})$$

Assuming a constant coolant molar flow rate ( $\dot{F}_c$ ) and a constant coolant heat capacity ( $C_{P,c}$ ), the energy balance can be written as:

$$\dot{F}_c \cdot C_{P,c} \cdot \frac{dT_c}{dx} = -U \cdot \pi \cdot D \cdot (T - T_c) \quad (\text{A.14})$$

leading to the final expression:

$$\frac{dT_c}{dx} = \frac{-U \cdot \pi \cdot D \cdot (T - T_c)}{\dot{F}_c \cdot C_{P,c}} \quad (\text{A.15})$$

which is similar to Equation III.76 presented in Section III.5.2.

# Appendix B

## Test conditions for kinetics validation

Test number	Inlet CO partial pressure (bar)	Inlet H <sub>2</sub> partial pressure (bar)	Inlet total pressure (bar)	Inlet syngas ratio H <sub>2</sub> /CO (-)	Space velocity at normal conditions (NL/h/g <sub>cat</sub> )
1	7.1	14.2	21.3	2	16
2	7.1	14.2	21.3	2	10
3	7.1	14.2	21.3	2	6
4	7.1	14.2	21.3	2	3
5	7.1	10.65	17.75	1.5	16
6	7.1	10.65	17.75	1.5	10
7	7.1	10.65	17.75	1.5	3
8	7.1	10.65	17.75	1.5	6
9	7.1	7.1	14.2	1	16
10	7.1	7.1	14.2	1	10
11	7.1	7.1	14.2	1	3
12	7.1	7.1	14.2	1	6
13	4.87	12.17	17.04	2.5	16
14	4.87	12.17	17.04	2.5	10
15	4.87	12.17	17.04	2.5	3
16	4.87	12.17	17.04	2.5	6
17	6.08	12.17	18.25	2	16
18	6.08	12.17	18.25	2	10
19	6.08	12.17	18.25	2	6
20	6.08	12.17	18.25	2	3
21	8.11	12.17	20.28	1.5	16
22	8.11	12.17	20.28	1.5	10
23	8.11	12.17	20.28	1.5	6
24	8.11	12.17	20.28	1.5	3

Table B.1: Test conditions, including inlet CO and H<sub>2</sub> partial pressures, total pressure, syngas ratio and space velocity at normal conditions, for which the reaction rates ( $r'_{FT}$  and  $r'_{CH_4}$ ) were experimentally measured (Ma et al., 2014a,b) and calculated. The temperature is 220°C and the inlet stream only contains CO and H<sub>2</sub> for all tests

# Appendix C

## Kinetics validation data

Test number	Experimental $r'_{FT}$ (mol/h/g <sub>cat</sub> )	Calculated $r'_{FT}$ by <a href="#">Ma et al. (2014a)</a> (mol/h/g <sub>cat</sub> )	Calculated $r'_{FT}$ by ULiège model (mol/h/g <sub>cat</sub> )
1	0.0205	0.0202	0.0199
2	0.0207	0.0199	0.0197
3	0.0204	0.0196	0.0194
4	0.0188	0.0186	0.0186
5	0.0178	0.0157	0.0153
6	0.0151	0.0154	0.0152
7	0.0129	0.0138	0.0140
8	0.0145	0.0149	0.0148
9	0.01	0.0109	0.0107
10	0.0112	0.0107	0.0105
11	0.0099	0.0095	0.0096
12	0.0111	0.0105	0.0103
13	0.0226	0.0202	0.0197
14	0.0206	0.0200	0.0196
15	0.0199	0.0198	0.0193
16	0.0192	0.0199	0.0195
17	0.0175	0.0185	0.0182
18	0.0172	0.0184	0.0181
19	0.0175	0.0180	0.0178
20	0.0182	0.0172	0.0171
21	0.0157	0.0168	0.0165
22	0.0184	0.0166	0.0163
23	0.0148	0.0160	0.0159
24	0.0141	0.0148	0.0150

Table C.1: Fischer-Tropsch reaction rate ( $r'_{FT}$ ) experimental and calculated values from [Ma et al. \(2014a\)](#) and calculated values from current model for all test conditions

Test number	Experimental $r'_{\text{CH}_4}$ (mol/h/g <sub>cat</sub> )	Calculated $r'_{\text{CH}_4}$ by <a href="#">Ma et al. (2014b)</a> (mol/h/g <sub>cat</sub> )	Calculated $r'_{\text{CH}_4}$ by ULiège model (mol/h/g <sub>cat</sub> )
1	0.0022	0.0022	0.0021
2	0.0021	0.0021	0.0021
3	0.0019	0.0020	0.0020
4	0.0016	0.0016	0.0016
5	0.0015	0.0015	0.0015
6	0.0014	0.0014	0.0014
7	0.0011	0.0010	0.0011
8	0.0013	0.0013	0.0013
9	0.0008	0.0009	0.0008
10	0.0008	0.0008	0.0008
11	0.0006	0.0006	0.0006
12	0.0007	0.0008	0.0008
13	0.0025	0.0026	0.0025
14	0.0025	0.0025	0.0024
15	0.0022	0.0022	0.0021
16	0.0023	0.0024	0.0024
17	0.0021	0.0020	0.0020
18	0.0021	0.0020	0.0020
19	0.0019	0.0019	0.0019
20	0.0016	0.0015	0.0016
21	0.0015	0.0016	0.0015
22	0.0015	0.0015	0.0015
23	0.0013	0.0014	0.0014
24	0.0010	0.0011	0.0011

Table C.2: Methane reaction rate ( $r'_{\text{CH}_4}$ ) experimental and calculated values from [Ma et al. \(2014b\)](#) and calculated values from current model for all test conditions